

Dynamical remodeling of neural circuit architecture

Dissertation

for the award of the degree
"Doctor rerum naturalium" (Dr.rer.nat.)
of the Georg-August-Universität Göttingen

within the doctoral program physics
of the Georg-August University School of Science
(GAUSS)

submitted by
Wenqi Wu

From Anhui, P. R. China
Göttingen 2023

Thesis Committee

Prof. Dr. Fred Wolf

Department of Nonlinear Dynamics, Max Planck Institute for Dynamics and Self-Organization, Göttingen

Bernstein Center for Computational Neuroscience, Göttingen

Department of Physics of Biological Systems, Georg-August-Universität Göttingen

Göttingen Campus Institute for Dynamics of Biological Networks

Prof. Dr. Jörg Enderlein

III. Physical Institute, Biophysics / Complex Systems, Georg-August-Universität Göttingen

Members of the Examination Board

Reviewer: Prof. Dr. Fred Wolf

Second Reviewer: Prof. Dr. Jörg Enderlein

Further members of the Examination Board:

Prof. Dr. Stefan Luther

Biomedical Physics Group, Max Planck Institute for Dynamics and Self-Organization, Göttingen

Prof. Dr. Ulrich Parlitz

Biomedical Physics Group, Max Planck Institute for Dynamics and Self-Organization, Göttingen

Prof. Dr. Reiner Kree

Institute for Theoretical Physics, Georg-August-Universität Göttingen

Date of the oral examination: June 15th, 2022

Declaration of Authorship

Herewith I declare that this thesis titled, “dynamical remodeling of neural circuit architecture” and the work presented in it are my own and prepared with no other sources and aids than quoted.

.....

Wenqi Wu, April 23,2022

Contents

1	Introduction	1
2	Fundamentals	4
2.1	The early visual pathway	4
2.2	The functional architecture of primary visual cortex	5
2.3	Development and plasticity of OPMs	8
2.4	Modeling the development of OPMs	9
2.5	Topographica Model	11
3	Van Hemmen Model	14
3.1	Introduction	14
3.2	Van Hemmen Model	15
3.3	Using Van Hemmen model to study Topographica model	18
3.3.1	The correlation function of LGN activity for Topographica model	18
3.3.2	The calculation process	19
4	A study of the basic Topographica model	21
4.1	Introduction	21
4.2	Materials and Methods	22
4.2.1	Orientation selectivity calculation: Vector average method	22
4.2.2	Pinwheel tracking	23
4.2.3	Simulation Procedure	24
4.2.4	The model	25
4.3	Results	28
4.4	Discussion	38
5	Map dynamics near the critical point	41
5.1	Introduction	41
5.2	Map development near the critical point	41
5.3	Impact of the parameter "excitatory range"	43
6	Impact of periodic boundary conditions	58
6.1	Introduction	58
6.2	Implementation of periodic boundary conditions	58
6.3	Map development with periodic boundary conditions	59
7	The impact of system size	62
7.1	Map structure for different system sizes	62
7.2	The process of the map development for different system sizes	62
8	Changing learning rates	69
8.1	Introduction	69
8.2	Map structure for different learning rates	69
8.3	Pinwheel movement for different learning rates	70

8.4	Pinwheel statistics for different learning rates	70
9	Impact of inhibitory interactions in the model	75
9.1	Introduction	75
9.2	Maps generated by the model with different inhibitory interaction ranges	75
9.3	The process of the map development for different inhibitory interaction ranges in the model	76
10	An analysis for correlated stimuli	82
10.1	Introduction	82
10.2	Using correlated stimuli in the model	82
10.3	The process of the map development for using correlated stimuli . . .	84
10.3.1	Pinwheel statistics for area size 1.5*1.5 and 1 pair of stimuli . .	84
10.3.2	Pinwheel statistics for area size 1.5*1.5 and 2 pairs of stimuli . .	89
11	Modeling the long range interaction in the visual cortex	95
11.1	Introduction	95
11.2	The observation for maps developed for the long range interaction in the model	95
11.3	The statistical analysis of the process of the map development for the modeling of long range interaction	96
12	The impact of different numbers of Gaussian stimuli for map development	98
12.1	Introduction	98
12.2	Map development using 2 Gaussian stimuli	98
13	Discussion and Conclusion	101
13.1	Pinwheel crystallization in the developmental model	101
13.2	Conclusion and outlook	102
	Bibliography	104
	Acknowledgements	109
A	Curriculum Vitae	110

Dedicated to my parents and grandmother, for your love for me

Chapter 1

Introduction

The brain can change dramatically during learning and development yet remains structurally stable (H.Lütcke, Margolis, and Helmchen, 2013). Stability and flexibility are both hallmarks of brain functions for animals to cope with changeable environments. Underlying sensory perception there are dynamic activity patterns which are responsible for memory and behavior of animals. Neural circuits have to deal with a trade-off between keeping stability for e.g. recognition of objects and being plastically adapted to changing requirements from the outside. In experiment, long-term imaging has shown that synaptic elements can be highly dynamic including in adult animals. Some studies point out that tuning properties appear more flexible and may be adaptive to stimuli and behaviors (J.R.Kohn et al., 2021; A.I.Weber, K.Krishnamurthy, and A.L.Fairhall, 2019; A.Borst, V.L.Flanagin, and H.Sompolinsky, 2005). In the hippocampus, recent investigations revealed that around 80% of the cells change their tuning properties over a timescale of a week (T.Hainmueller and Bartos, 2018; T.Bonhoeffer, M.Huebener, and T.Rose, 2017). The zebra finch, for example, sings a highly stereotyped song that is stable for years, but the neuron patterns underlying song shift from day to day (for a review, see M.S.Brainard and A.J.Doupe (2000)).

Visual cortex, as a model for plasticity, has been studied for many years (D.H.Hubel and T.N.Wiesel, 1962; D.H.Hubel and T.N.Wiesel, 1963b; B.A.Wandell and S.M.Smirnakis, 2009; J.S.Espinosa and M.P.Stryker, 2012; Ko et al., 2011; L.White and D.Fitzpatrick, 2007; M.Sur and C.A.Leamey, 2001; Y.Frégnac et al., 1988; Y.Frégnac, S.Thorpe, and E.Bienenstock, 1992). It is still controversial, however which mechanisms guide the emergence and development of a hallmark of the cortical functional architecture, orientation preference maps (OPMs) (M.Kaschube et al., 2010a; J.B.Ackman and M.C.Crair, 2014; W.H.Bosking, J.C.Crowley, and D.Fitzpatrick, 2002; M.Kaschube et al., 2010b; E.Erwin, K.Obermayer, and K.Schulten, 1995). Two classes of mechanisms have been proposed, one is about molecular recognition of gradients of diffusible ligands and cell-surface receptors to arrange map structures, another one are called activity-dependent mechanisms which means the visual system uses correlated patterns of pre- and postsynaptic activity to lead the map formation (L.White and D.Fitzpatrick, 2007). The activity patterns are generated within the visual pathway from retina, LGN to the primary visual cortex (M.V.Albert, Schnabel, and D.J.Field, 2008; S.Behpour, D.J.Field, and M.V.Albert, 2021). After an animal's eyes open, the activity is driven by visual experience. Many people believe that molecular recognition governs the initial map formation and helps build a basic topology structure, but for later stages in development, retinal activity patterns are required to tune the maps for maturation (L.E.White, D.M.Coppola, and D.Fitzpatrick, 2001; M.Sur and C.A.Leamey, 2001; M.C.Crair, D.C.Gillespie, and M.P.Stryker, 1998b). A recent study shows in vivo by using calcium imaging that at early development period in

ferret visual cortex contralateral, ipsilateral or binocular stimulation each creates distinct representations of orientation that are misaligned at the columnar and cellular scale (J.T.Chang, D.Whitney, and D.Fitzpatrick, 2020). It is visual experiences that drive the reorganization of these three representations to a unified binocular representation of orientation. Another example is found in juvenile animals exposed to stimuli with a restricted range of orientation, as a result the OPMs are obviously affected (F.Sengpiel, P.Stawinski, and T.Bonhoeffer, 1999a). This indicated experience-dependent plasticity after the initial formation of OPMs.

The role visual experience plays may be more important than widely thought. Several substantial biological changes in V1 are observed which follow eye opening of animals (L.White and D.Fitzpatrick, 2007). At the time when visual experiences drive the activity in the visual pathway, the density of cortical synapses in V1 is only a fraction of that found in maturity and a large part of synapses are added during the development when visual experiences affect the neural activity in V1. Interestingly, the rapid increase of cortical synapses is accompanied by an outgrowth of long-range horizontal connections which accelerates after eye opening. These long-range connections are regarded as connections of cortical columns with similar response properties (C.Gilbert and T.N.Wiesel, 1989; R.Malach et al., 1993; W.H.Bosking et al., 1997). For orientation selectivity of V1, these connections are used to link neurons with similar orientation preferences. Taken together, these observations indicate that a large part of the construction of neural circuits in supragranular layers of V1 takes place during a period when V1 is responsive to visual experiences. Furthermore, by intrinsic signal optical imaging techniques it has been observed that, after OPMs are initially detectable at the time of eye opening of some species, e.g. ferret, the strength of mapping signals increases significantly until it reaches maturation state. So during the postnatal period the maps become more robust and achieve full map strength.

To sum up the above, the visual experiences are considered to exert a profound influence over the formation and maturation of OPMs instead of only maintaining the maps. In fact, receptive fields can be extremely plastic in V1. For instance, one study demonstrated using a STDP protocol one can induce rearrangement of cortical neurons' sub-threshold and supra-threshold responses by only a few spikes (V.Pawlak et al., 2013). During an hour a cortical neuron fires thousands of spikes. Whether and why the orientation selectivity persists under this continuous stream of activity is not clear and has not frequently been investigated in theoretical models. Also the question about how visual experience exactly impact neuronal responses and cortical architecture in the developing brain is still not well understood. Recently, the Bednar group has built a detailed model with input driving the activity in the visual system and open software packages are available online (J.Stevens et al., 2013). We will use this well established model to investigate this open question. For this model, the issues about time scales of modeling map formation, types of map rearrangement and final states of the map development will be examined in detail.

An overview of my work is as follows. Except for the introduction parts, Chapter 3 considers utilizing the van Hemmen model to reveal the mechanism of the formation of receptive fields in the Topographica model and the results show that the framework of the van Hemmen model is likely unsuitable to apply to the Topographica model. Chapter 4 examines, with the same conditions as used originally in the Topographica model (J.Stevens et al., 2013), the dynamics of OPM development is a long-term process and pinwheel crystals and boundary effects are discovered in the simulations. Chapter 5 studies parameter variation of the excitatory range in the model and analyzes the characteristics of pinwheel layouts during the map

development. To remove boundary effects, Chapter 6 studies the model with periodic boundary conditions which are newly implemented and gives the dynamical description of cortical pattern changes under this condition. Chapter 7 analyzes the process of OPM development for using different system sizes of the model and finds that in a larger size of cortical area the pinwheel crystallization process is more apparent and clearly observed. Chapter 8 compares pinwheel statistics generated by using different learning rates in the model. Chapter 9 examines the impact of changing the parameter of the inhibitory interaction in the model and discovers that the OPMs produced by using the previously used parameters values fail to match the OPMs in the experiments. Chapter 10 studies the question whether using correlated stimuli can reproduce OPMs conforming to the features of the common design (see Chapter 2). The answer is no. Chapter 11 builds the model with a type of the long range cortical interaction and examines the pinwheel statistics produced under this condition. The results exhibit that the model with the long-range interaction in the visual cortex and periodic boundary conditions is not able to generate features for the common design. Chapter 12 is concerned with the impact of different numbers of input patterns on OPM development in the model and discovers that the maps which have pinwheel statistics similar to the common design are observed.

Chapter 2

Fundamentals

2.1 The early visual pathway

The early visual pathway is presented in Figure 2.1. The visual pathway begins with the retina where light enters through lens and falls on photo-receptors which convert light signals into spike patterns. The retinal ganglion cells on the outermost layer of retina conduct these action potentials to the brain. Different populations of ganglion cells in the retina send information to the brain through the optic nerve. The optic nerves from both eyes meet and cross at the optic chiasm, where the information coming from both eyes is combined and then splits according to the visual fields. From there the information from the left visual field travels in the right optic tract, and information from the right visual field travels in the left optic tract. This means, the right half brain will process the information from the left field of view and the left half brain will deal with the information from the right field of view. Each optic tract targets the lateral geniculate nucleus (LGN) in the thalamus. The LGN consists of 6 layers in humans and some other primates. Layer 1, 4 and 6 receive information from the origin of nasal retina whereas layer 2,3 and 5 receive information from the origin of the temporal retina. One of the main functions of LGN is relaying the signals of retinal ganglion cells without modifying much of them. Therefore the properties of receptive fields of LGN are similar to receptive fields of retinal ganglion cells (E.Kaplan, S.Marcus, and Y.T.So, 1979; S.F.Tavazoie and R.C.Reid, 2000). Both of them have center-surround structures. The visual information is carried by optic radiation from LGN to the layer 4 of the primary visual cortex (V1), which is located in the posterior pole of the occipital lobe. V1 is the first stage of cortical processing of visual information and highly specialized at pattern recognition of the moving and static visual objects. V1 is composed of a two-dimensional sheet of neurons and contains a large number of neurons. In human, the number is about 140 million neurons per hemisphere.

V1 has retinotopic organization. This means V1 contains a complete map of the visual field. Retinotopy is continuous, because neighboring point in V1 area correspond to neighboring visual positions in the visual field.

There are two types of neurons in V1 area: simple cells and complex cells, according to the structure of receptive fields (D.H.Hubel and T.N.Wiesel, 1959; J.A.Movshon, I.D.Thompson, and D.J.Tolhurst, 1978; H.Kato, P.O.Bishop, and G.A.Orban, 1978). The receptive fields of simple cells have two distinct responsible regions: on and off subregions. On subregions respond to the light part of stimuli while off subregions respond to the dark part of stimuli. But for complex cells, on and off regions are superimposed, which means one position of the receptive fields can be stimulated by both the light part and dark part of stimuli.

Neurons in V1 have many response properties. One of the important properties is ocular dominance, which means neurons are selectively responsive to right eye

or left eye. Another important property is orientation selectivity, which indicates that different neurons in V1 have different orientation preferences for stimulus and response most strongly for preferred orientation of the stimulus (D.H.Hubel and T.N.Wiesel, 1962; D.H.Hubel and T.N.Wiesel, 1963b). In addition to these properties, neurons in V1 are also selective for several attributes, such as direction of motion, spatial and temporal frequency and so on. Here we don't introduce these aspects.

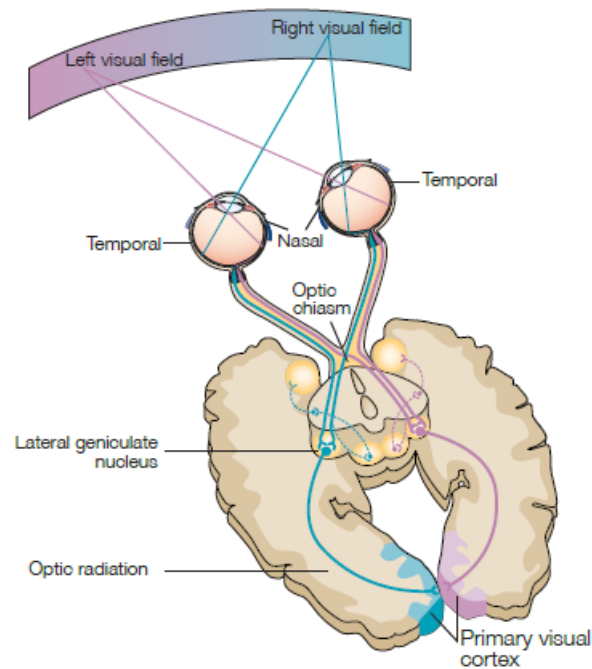


Figure (2.1) Schematic illustration of the early visual pathway in carnivores and primate. The visual pathway begins with the retina where light enters through lens. The optic nerves from both eyes meet and cross at the optic chiasm for information combination and splitting. Each optic tract projects to the lateral geniculate nucleus (LGN) in the thalamus. Then visual information is transmitted by optic radiation from LGN to the primary visual cortex (V1) (adapted from D.E.Hannula, D.J.Simons, and N.J.Cohen (2005)).

2.2 The functional architecture of primary visual cortex

The cerebral cortex is the outer layer of neural tissue of the cerebrum of the brain in humans and other mammals. The cerebrum is the largest part of the brain. In the human brain, the cerebrum is the uppermost region of the central nervous system. The cerebral cortex plays a key role in attention, awareness, thought, perception, memory, language and consciousness. It has a functional structure of cortical columns, which are groups of neurons extending perpendicular to the cortical surface and have nearly identical receptive fields. Neurons within a column share similar functional properties. In the single cortical layer parallel to the surface, neuronal selectivity varies systematically. We understand the two dimensional patterns with such characteristics as the functional maps of visual cortex. Especially, the spatial structure of orientation preference is referred to as the functional architecture of primary visual cortex.

In the primary visual cortex of primates and carnivores, the structural units for orientation selectivity are called orientation columns. The two-dimensional patterns

which consist of orientation columns are called orientation preference maps. Experimentally, the pattern of orientation preferences is measured by using optical imaging of intrinsic signals (A.Grinvald et al., 1986; A.Grinvald et al., 1988). This method is accomplished using an enhanced video acquisition system. It records the changes from light reflectance when the cortical tissue is activated by different illuminance conditions. Typically, the cortical responses $E_k(\mathbf{x})$ are produced by stimulation with a grating of orientation ϑ_k , see Fig 3.2(A). Here \mathbf{x} represents the location of a column in the cortex. The activity patterns ($E_k(\mathbf{x})$) can be summarized to construct a complex field which represents the two-dimensional orientation preference maps:

$$z(\mathbf{x}) = \sum_k e^{2i\vartheta_k} E_k(\mathbf{x})$$

The preferred orientation of neurons at location \mathbf{x} can be obtained from:

$$\vartheta(\mathbf{x}) = \frac{1}{2} \arg(z)$$

The module $|z(\mathbf{x})|$ is a measure of orientation selectivity at cortical location \mathbf{x} . An example of OPM constructed by this approach is shown in Figure 2.2. In OPMs there is a typical organization called pinwheel around which columns preferring all orientations surround a common center in a radial fashion (A.Grinvald et al., 1986; D.H.Hubel and T.N.Wiesel, 1977; G.G.Blasdel and G.Salama, 1986; T.Bonhoeffer and A.Grinvald, 1991). Pinwheels actually are the singular points of the field $\vartheta(\mathbf{x})$. See Figure 3.2. Mathematically, pinwheel centers are the roots of the complex field $z(\mathbf{x}) = 0$ (N.V.Swindale, 1982). As a topologically conserved measurement for continuously changing OPMs, topological charge indicates whether the preferred orientations arrange around pinwheel centers in a clockwise or counterclockwise way (N.V.Swindale, 1982). It is defined as:

$$q_i = \frac{1}{2\pi} \oint_{C_i} \nabla \vartheta(\mathbf{x}) ds$$

C_i is a closed curve around only a pinwheel center and $\vartheta(\mathbf{x})$ is a continuous function up to isolated singular points. Since $\vartheta(\mathbf{x})$ is a periodic variable from 0 to π , q_i can have values (N.D.Mermin, 1979):

$$q_i = \frac{n}{2}$$

In experiments, only the pinwheels with values $|q_i| = \frac{1}{2}$ are observed. $q_i = \frac{1}{2}$ means the preferred orientations increase around pinwheel centers in a clockwise way, while $q_i = -\frac{1}{2}$ for the opposite change way of the orientations. Other topological charges of $q_i = \pm 1, \pm \frac{3}{2} \dots$ are never observed in animals. The pinwheel centers can be visualized at single cell level with the experimental method of two-photon calcium imaging in vivo (K.Ohki et al., 2006a).

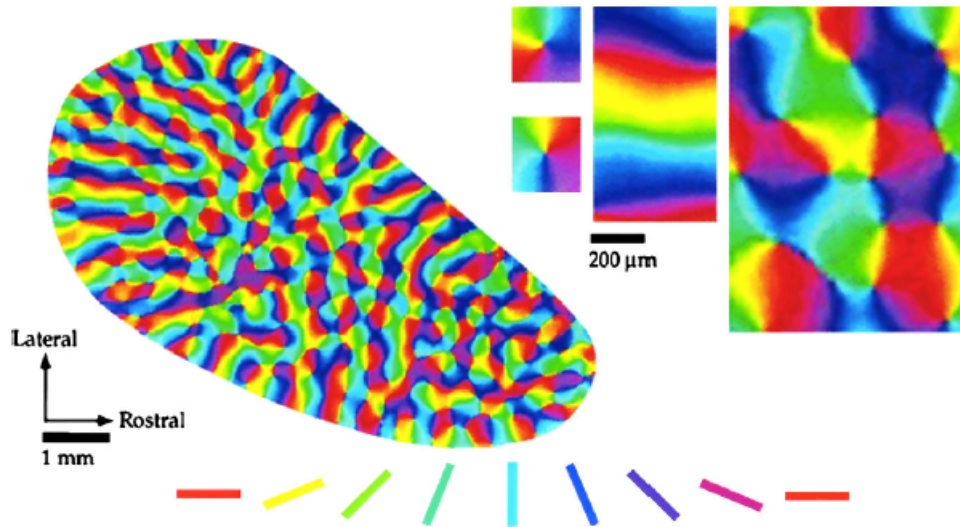


Figure (2.2) Orientation preference maps in the visual cortex of a tree shrew. Different colors indicate different orientation preferences for the stimuli with the color coded orientation. This map was obtained by optical imaging by summing complex fields evoked by stimuli with different orientations. The right part shows pinwheel structures. Pinwheel centers are the singular points around which all orientations are arranged in a radial way (adapted from W.H. Bosking et al. (1997)).

The OPM exhibits a roughly repetitive arrangement of preferred orientations. The column spacing Λ measures the average distance of adjacent iso-orientation domains, which can be achieved by using wavelet analysis (M. Kaschube et al., 2010b; T. Bonhoeffer and A. Grinvald, 1993). This size of Λ^2 are called hypercolumn, which contains the neuronal columns responding to all the orientations of stimulus. A hypercolumn occupies an area of about 1 mm^2 on the cortical surface.

To characterize the layout of orientation columns, M. Kaschube et al. (2010b) developed a statistical approach based on pinwheel density. The concept of pinwheel density means the average number of pinwheels per hypercolumn area. Firstly, they found the mean pinwheel density was virtually identical in six species which are macaque, mouse lemur, cat, tree shrew, galago and ferret and the values are close to π (M. Kaschube et al., 2010b; W. Keil et al., 2012; M. Schottdorf et al., 2015a; C.L.A. Ho et al., 2020). Secondly, they characterized intramap heterogeneity and local arrangement of neighboring pinwheels. Their calculation results suggest these species share a "common design" of orientation column layouts: the virtual identity of (i) pinwheel density, (ii) pinwheel density fluctuations as a function of subregion size, and (iii) nearest-neighbor distance distributions of pinwheels. These findings support that in spite of phylogenetical and ecological diversity during evolution, carnivores and primates may follow a common layout rule of orientation columns.

In the primary visual cortex of a range of species, long-range horizontal connections are observed to link the iso-domanins of the same or similar orientation preference in the maps, as revealed by a number of experiments (W.H. Bosking et al., 1997; K.S. Rockland and J.S. Lund, 1982; L.C. Sincich and G.G. Blasdel, 2001; M. Weliky and L.C. Katz, 1994; C.D. Gilbert and T.N. Wiesel, 1979; C.D. Gilbert and T.N. Wiesel, 1983; Z.F. Kisvarday et al., 1997; M. Callaway and L.C. Katz, 1990; S. Löwel and W. Singer, 1992; L.E. White, D.M. Coppola, and D. Fitzpatrick, 2001). Studies in both of cat and monkey visual cortex, for example, have demonstrated that horizontal connections selectively link patches of neurons that have similar orientation preferences. These connections extend for millimeters parallel to the cortical surface and generate patchy

terminations. Horizontal connections are an important feature of the intrinsic circuitry of the visual cortex.

Compared to an ordered spatial arrangement of orientation columns in carnivores and primates, glires or rodents, e.g. rats, gray squirrels and rabbits have columnless, apparently random, salt-and-pepper organization for orientation preferences, although all of their cortical neurons selectively respond to stimulus orientations (K. Ohki et al., 2005). See Figure 2.3. The complete randomness of organization for rodents and the ordered arrangement of orientation columns for primates and carnivores pose an enigma for researchers about the formation mechanisms. One suggested that the short-range circuit interaction is responsible for the formation of the salt-and-pepper organization while a long range cortical interaction gives rise to the columnar structure conforming a common design rule (M. Kaschube et al., 2010a).

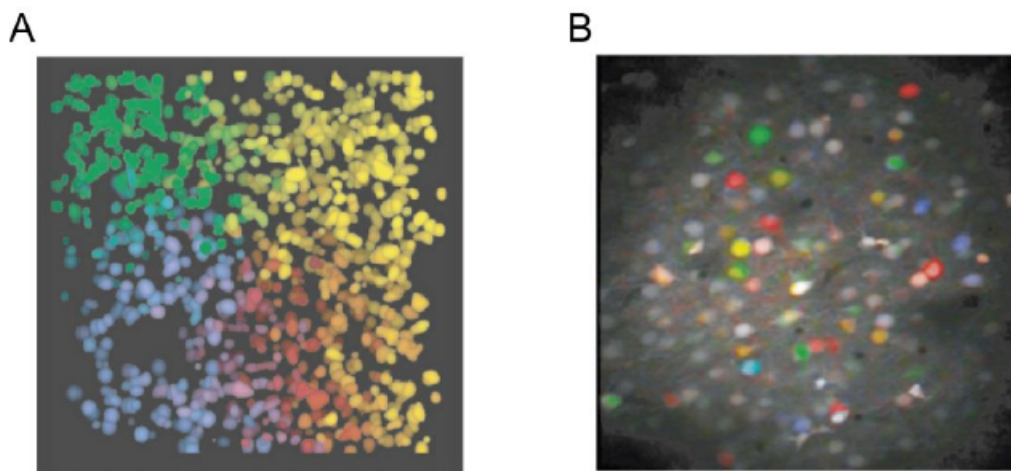


Figure (2.3) single-cell resolution orientation maps for (A) cat's visual cortex and (B) rat's visual cortex obtained by in vivo two-photon calcium imaging. (A) is a pinwheel of cat's visual cortex (adapted from K. Ohki et al. (2006b)). (B) is salt-and-pepper structure of rat's visual cortex. Different color indicates different orientation preferences of neurons (adapted from K. Ohki et al. (2005)).

2.3 Development and plasticity of OPMs

How do the cortical functional architecture emerge during the development of animals? There is a long-term question that to what extent the structure and functions of orientation columns are determined by genetic coding and visual experience. Experimental evidences show that an initial OPM can be established without any visual inputs (B.G. Cragg, 1975; R. Backmann and K. Albus, 1982; S.F. Tavazoie and Reid, 2000; B.M. Hooks and C. Chen, 2006; U.R. Karmarkar and D. Yang, 2006a). Spontaneous activity may play a role in establishing the cortical patterns before or during eye opening. In an experiment tree shrew is dark rearing and shows normal OPMs with pinwheel density close to π (M. Kaschube et al., 2010a). The size of neural network including a huge number of neurons and synapses in one hypercolumn is extremely large. It is unlikely for genes to encode the activities and connections of this type of neural networks. Instead, for visual cortex, the synaptic architecture of visual cortex remains plasticity and refinement lasting several months after the initial orientation selectivity is established (M. Sur and C.A. Leamey, 2001). Some experimental observations indicate that the development of OPMs is a process of experience-dependent plasticity (U.R. Karmarkar and D. Yang, 2006b; B. Godde et al.,

2002). One of the most remarkable evidences supporting this hypothesis comes from the visual inputs rewired to the auditory cortex in ferrets (J.Sharma, A.Angelucci, and M.Sur, 2000). Thalamocortical projections from the retina were experimentally redirected to the auditory pathway at a very early stage of development. As a consequence, similar patterns of OPMs have been observed in the area that would normally be the primary auditory cortex. This experiment suggests that by manipulation to give inputs with some conditions the cerebral cortex can generate similar cortical maps at different areas. Another experiment shows the visual cortex of kittens reared in a striped environment responded to all orientations, but contributed to twice as much surface area to the experienced orientation as the orthogonal one (F.Sengpiel, P.Stawinski, and T.Bonhoeffer, 1999b). This effect indicates an instructive role of visual experience to make some neurons change their orientation preference. Also, some other experiments show the deprivation of visual experience will cause the degradation of OPMs (M.C.Crair, D.C.Gillespie, and M.P.Stryker, 1998a). What is more, Sensory maps can undergo plastic changes with experience even in adult brains (V.Pawlak et al., 2013; U.R.Karmarkar and D.Yang, 2006a). But how visual experience impact neuronal responses and cortical architecture in the developing brain are still not well understood.

To summed up, the initial establishment of orientation map may be free requirement of visual experience but in the later stage of development the visual cortex can be plastic and refined by visual experience. Especially, for the second stage there is a period called critical period during which the cortex is most susceptible to visual inputs (L.Reichl et al., 2012; B.M.Hooks and C.Chen, 2007). For example, in cats the critical period lasts for about 3 months (K.R.Jones, P.D.Spear, and L.Tong, 1984).

2.4 Modeling the development of OPMs

Since Hubel and Wiesel in experiments discovered the orientation selectivity of neurons in cats' primary visual cortex, many models have been proposed to modeling the emergence and the development process of orientation selectivity (for review, see N.V.Swindale (1996) and G.J.Goodhill (2007)). Hubel and Wiesel firstly presented a model about genetical predetermination of required neuronal circuitry (D.H.Hubel and T.N.Wiesel, 1963a). But there are several disadvantages of this model which are, for example, a high cost of genetical information about afferent axon branches to contact neurons, neglect of considering cortical plasticity. Then activity-dependent mechanisms have been applied to understand the development of functional architecture of V1. The pioneer work of this aspect was done by Malsburg (1973), Malsburg and D.J.Willshaw (1976), and Malsburg and D.J.Willshaw (1977). Their model consists of a network of cells which has two sheet, one represents retina and another one represents V1. Cells in retina are connected to units in V1 sheet which are postsynaptic. The connection strengths are random initially and can be learned according to Hebb learning rule (D.O.Hebb, 1949). There are two types of neurons in cortical layer, excitatory and inhibitory ones, which interact to each other, with short range excitation effect and long range inhibitory effect. Nine different set of stimuli in the form of light bars were presented to the retina sheet. After 20 presentations of all the stimuli different neurons in the cortical sheet become response selective to different orientations. Also one can observe there are groups of nearby neurons having same or similar orientation selectivity, which are analogous to cortical columns. Linsker proposed a model of self-organization in the visual system that does not require structured input (R.Linsker, 1986a; R.Linsker, 1986b; R.Linsker, 1986c). The

network consists of several layers and the units of the network are linear and are organized into two-dimensional layers. There are feed-forward connections between layers, with each unit receiving inputs only from a neighborhood in the previous layer which are regarded as receptive field. Linsker used a modified Hebbian learning rule to update the connection weights. This linear network can reproduce orientation preference patterns. Linsker's model shows that structured inputs for retina are not necessary to generate structured patterns of receptive fields in later processing stages. And unstructured "spontaneous" activity patterns are sufficient to form structured receptive fields during the development process. K.D.Miller (1994) studied a linear mathematical model consisting of a LGN ON cell-layer, a LGN OFF cell-layer and a cortical layer. In this model the correlations among afferent activities determine receptive field structure. If the correlation function does not change sign within an arbor radius, the resulting cortical cells come to receive only ON-center or OFF-center inputs. If the correlation function changes sign, so that at small separations same type inputs are best correlated, but at larger separations within the arbor radius opposite-type inputs are best correlated, then the segregated ON center and OFF center subregions of receptive fields are developed.

Meanwhile, high-dimensional nonlinear models had been proposed and also observed structure of the topographic map can arise from these models (K.Obermayer, H.Ritter, and K.Schulten, 1990; G.J.Goodhill, 1993; H.G.Barrow, A.Bray, and J.M.L.Budd, 1996; M.Riesenhuber et al., 1998; J.Sirosh and R.Miikkulainen, 1997; J.A.Bednar and R.Miikkulainen, 2006). In addition, these models were pointed out to have some different properties from the linear models.

Compared with high-dimensional models, some authors have proposed "low-dimensional" models which are also referred as dimension reduction framework (R.Durbin and G.Mitchison, 1990; G.J.Goodhill and D.J.Willshaw, 1990; K.Obermayer, G.G.Blasdel, and K.Schulten, 1992). We consider an example of multiple dimensional feature space which is spanned by quantities describing e.g. receptive field properties of cortical cells. The coordinates can correspond to the position of a receptive field in retinotopic space, to orientation preferences and specificity and to ocular dominance. These feature variables form a five dimensional space and each point in this space is mapped onto one point in the two-dimensional cortical surface of the primary visual cortex. These models are generally based on using either the elastic net (R.Durbin and D.J.Willshaw, 1987) or T.Kohonen (1982), T.Kohonen (2000), and T.Kohonen (2006). For example, W.Keil and F.Wolf (2011) presented a mathematical approach to calculate cortical representations predicted by the elastic net (EN) model for the joint mapping of stimulus position and orientation. The EN model trades off of the space of visual stimulus features and the continuity of their cortical representation. On the one hand, each stimulus features should be contained in the representation of a cortical map. On the other hand, the wiring cost of neuron connections should be kept low. To achieve this neurons that are physically close in the cortex are required to have similar orientation preferences. These two aspects compete with each other. This research demonstrates the optimization models for EN are in principle capable of correctly predicting the common OPM design.

The analogy between the pattern formation of physical systems and the development of OPMs in visual cortex inspires a class of mathematical models called the long range interaction model (F.Wolf, 2005; M.Kaschube et al., 2010a; F.Wolf and T.Geisel, 2003). These models are based on symmetry consideration and are the only models which can reproduce the common design features of OPMs. The long-range interaction model is defined by a dynamical equation for an order parameter field $z(x, t)$ that completely characterizes the spatial pattern of preferred orientations at

time t . It consists of linear part and nonlinear part. In the nonlinear part there is non-local interaction which is the key ingredient for pinwheel stabilization during the map development. But one disadvantage of these models is that it is abstractly formed and lacks details about how input activity patterns drive the self organization process of OPM development.

In recent years Bednar group made a detailed model available to do simulations and study (J.Stevens et al., 2013; J.A.Bednar and R.Miikkulainen, 2004; R.Miikkulainen et al., 2005). An introduction will show the model in the following.

2.5 Topographica Model

The Topographica model is intended to mimic the biological structures and developmental process of orientation preference maps in primary visual cortex. In this model, the V1 network is a sheet of $N \times N$ interconnected computational units represented as “neurons”. Each cortical neuron receives external input from two types of LGN cells: ON-center and OFF-center. The LGN neurons in turn receive input from the retina, which consists of $R \times R$ array of photoreceptor cells. In addition to the afferent connections, each cortical neuron has local excitatory and inhibitory connections with other neurons. Excitatory connections have a short range and inhibitory connection have a larger range connecting nearby units. By a Hebbian mechanism, the intracortical interaction function is determined by intracortical synaptic connections: it is positive between two cortical locations that tend to excite one another, and negative between locations that tend to inhibit one another.

The ON and OFF neurons represent the entire pathway from photoreceptor output transferred to the input for V1, including the ON and OFF processing in the retinal ganglion cells and the LGN. In this model ON and OFF are simply divided into separate channels and organized into an $L \times L$ array corresponding to the retinotopic organization of the LGN. Each neuron of LGN and V1 generate an initial response by a weighted sum of neurons’ responses in its connection field of afferent input. The intracortical interaction regarded as “Mexican-Hat” type between cortical neurons then form the initial activation activity into a localized cortical pattern. After the pattern has stabilized, the connection weights of cortical neurons are modified based on Hebbian learning rule. As the self-organization progresses, responses of these neurons grow more nonlinear and weak connections decay. The result is a self-organized structure formation in a dynamical process driven by the input.

The following subsections describe the specific components of Topographica model in more detail.

Retina. An input pattern is presented to the model by activating the photoreceptor units in the retina according to the gray-scale values in the pattern. To generate such input patterns, the activity Ψ for photoreceptor cell x_c, y_c is calculated according to:

$$\Psi(x_c, y_c, \theta) = \exp\left(-\frac{((x - x_c)\cos\theta + (y - y_c)\sin\theta)^2}{2\sigma_u^2} - \frac{(-(x - x_c)\sin\theta + (y - y_c)\cos\theta)^2}{2\sigma_v^2}\right) \quad (1)$$

, $(x_c, y_c), \theta$ are random positions and orientation.

ON/OFF sheets. The cells in the ON and OFF channels of the LGN compute their responses as a weighted sum of activity in their receptive fields. More precisely, the activation level η for a unit at position j in an ON/OFF sheet O at time $t + \delta t$ is

calculated as

$$\eta_{j,O}(t + \delta t) = f\left(\frac{\gamma_O \sum_{i \in F_{j,p}} \Psi_i(t) w_{ij}}{k + \gamma_s \sum_{i \in F_{j,s}} \eta_{i,O}(t) w_{ij,s}}\right) \quad (2)$$

Ψ_i is the activation value of unit i on retina from which ON/OFF unit j receives input and its afferent connection field is $F_{j,p}$. $\eta_{i,O}(t)$ is the activation of other units in ON/OFF sheets on the previous step and received over the connection field $F_{j,s}$. The function f is a half-wave rectifying function which removes the negative part of the activation and ensures that $\eta_{j,O}$ is always positive. The $\gamma_O = 14$ is a constant strength for the connections from the photoreceptor sheet to the ON/OFF sheet to give the activation level in the range 0.0 to 1.0. If contrast-gain control is not applied, $k = 1$ and $\gamma_s = 0$. If applied, e.g., in the GCL and GCAL models, $k = 0.11$ and $\gamma_s = 0.6$. The weights w_{ij} define the strength of connections from the unit i in Retina to the ON or OFF unit j and is a standard difference-of-Gaussian kernel. The Mexican-hat shape of w_{ij} makes the connection area for ON unit j has positive center and negative surround, and vice versa for OFF units. The mathematical form of the weight w_{ij} from an ON unit j located at (x, y) and the unit i at position (x', y') in Retina is given by:

$$w_{ij}^{ON} = \frac{1}{Z_c} \exp\left(-\frac{(x - x')^2 + (y - y')^2}{2\sigma_c^2}\right) - \frac{1}{Z_s} \exp\left(-\frac{(x - x')^2 + (y - y')^2}{2\sigma_s^2}\right) \quad (3)$$

The width of the central Gaussian is given by $\sigma_c = 0.037$, and the surround Gaussian $\sigma_s = 0.15$. Z_c and Z_s define the normalization constants that make sure the weights sum equal 1.0. The weights for the OFF units are the negative of Equation (3).

Finally, when the contrast-gain control is activated, the weights $W_{ij,s}$ in the Equation (2) define the spatial profile of the lateral inhibitory interactions between unit j and other unit i in the ON/OFF sheet. The weights $W_{ij,s}$ is a fixed, circular Gaussian profile so that the connection between neuron j in the location (x, y) and the presynaptic neuron i in the location (x', y') is given by :

$$w_{ij,s} = \frac{1}{Z_s} \exp\left(-\frac{(x - x')^2 + (y - y')^2}{2\sigma_s^2}\right) \quad (4)$$

where $\sigma_s = 0.125$ and Z_s is a normalizing constant.

The V1 sheet. Each V1 unit receives inputs from connections between ON/OFF sheet and V1, and between V1 neurons. We can call these connections "projections" (p). The projections can be the afferent projection from the ON/OFF sheets ($p = A$), or the recurrent lateral excitatory projection ($p = E$), and the recurrent lateral inhibitory projection ($p = I$). from other V1 units. The activation of unit j in V1 sheet by afferent connections is defined as following:

$$\eta_{j,V}(t) = f\left(\sum_p \gamma_p C_{jp}(t)\right) \quad (5)$$

$$C_{jp}(t + \delta t) = \sum_{i \in F_{j,p}} \eta_{i,p}(t) w_{ij,p} \quad (6)$$

The scaling factors for each projection type are $\gamma_A = 1.5$, $\gamma_E = 1.7$, $\gamma_I = -1.4$, to provide a balance between excitation and inhibition, and between afferent and lateral influences, to allow smooth map to form. C_{jp} is the contribution to the activation of unit j from each projection type. $\eta_{i,p}$ is the activation of unit i of ON/OFF sheet or

V1 neurons to which unit j is connected (its connection field F_j and $w_{ij,p}$ is the connection weight from unit i in LGN or V1 to unit j in LGN or V1 for the projection p . f is a half-wave rectifying function. After previously mentioned steps from Retina to V1, the final activation of V1 units is the response to the present stimulus in Retina. At this point the response of V1 will be used to update the threshold of V1 units and to update the afferent and lateral inhibitory weights through Hebbian learning rule. Then the activation in V1 will be reset to 0, and then a new pattern will be presented in Retina and thus the next iteration will be started.

Adaptation. The adaptation process is to bring the average activity of every unit in V1 close to a specified value. It consists of two steps. The first step is to calculate a smoothed average of settled activity patterns for each unit j .

$$\overline{\eta_j(t)} = (1 - \beta)\eta_j(t) + \beta\eta_j(t - 1) \quad (7)$$

β is called the smoothing parameter which control the degree of smoothing. The initial value of $\eta_j(t = 0)$ is the target average V1 unit activity μ which equal 0.024. The threshold is updated as follows:

$$\theta(t) = \theta(t - 1) + \lambda(\overline{\eta_j(t)} - \mu) \quad (8)$$

where $\lambda = 0.01$ is the homeostatic learning rate. If the activity in the unit j move away from the specified target, the threshold, according to the Equation (8), will be automatically increased or decreased in order to force it closer to the target.

Learning. The weights of initial connection field are given by isotropic 2D Gaussians for the lateral excitatory projection and uniformly random within a Gaussian envelope for afferent and lateral inhibitory projections. Specifically, a neuron located at (x, y) has a connection weight from unit i at (x', y') with following value:

$$w_{ij} = \frac{1}{Z_p} u \exp\left(-\frac{(x - x')^2 + (y - y')^2}{2\sigma_p^2}\right) \quad (9)$$

here $u = 1$ for lateral excitatory projection $w_{ij,E}$ and u is a random value chosen from a uniform distribution for the afferent and lateral inhibitory projections $w_{ij,A}$ and $w_{ij,I}$. σ_p defines the width of Gaussian and $\sigma_A = 0.27, \sigma_E = 0.025, \sigma_I = 0.075$, and Z_p is a normalizing factor to ensure the total of all weights w_{ij} equal to 1. When an image is presented to the Retina, the weights $w_{ij,p}$ are updated once per iteration by using a Hebbian learning rule. This rule reflects the correlations between the ON/OFF unit activities and the V1 response activities. The updating procedure of Hebbian connection weights at each iteration dependent on the activities of both presynaptic and postsynaptic units, and the learning rate:

$$w_{ij,p}(t) = \frac{w_{ij,p}(t - 1) + \alpha\eta_i\eta_j}{\sum_k (w_{kj,p} + \alpha\eta_j\eta_k)} \quad (10)$$

The Hebbian learning rates for afferent connections, lateral excitatory connections and lateral inhibitory connections are $\alpha_A = 0.1, \alpha_E = 0$ and $\alpha_I = 0.3$, respectively.

Chapter 3

Van Hemmen Model

3.1 Introduction

In primary visual cortex, visual information is processed from retina to the cortical areas. Basically, the processing experiences starting from retina, then going to lateral geniculate nucleus (LGN), finally projecting to the visual cortex. More details about this process are shown in Chapter 2.

Cells in the LGN and the visual cortex are characterized by their receptive field regarded as the area on the retina or LGN that is to be activated by a light pattern so as to evoke a response of the neuron. In retina and LGN, each receptive field is arranged into a central disk, the "center", and a concentric ring, the "surround", each region responding oppositely to light. In the LGN, there are two types of cells, the ON cells and the OFF cells. An ON cell will show largest response if a light spot is projected into the center of its receptive field. Similarly, an OFF cell responds best if a light stimuli shine on the surrounding part of its receptive field.

For cortical cells, they respond selectively to the orientation of light stimulus within the cell's receptive fields (D.H.Hubel and T.N.Wiesel, 1959). According to Hubel and Wiesel's classification, cortical cells are divided to simple cells, complex cells and hypercomplex cells (D.H.Hubel and T.N.Wiesel, 1962). Cortical simple cells receive direct input from the LGN. Simple cell receptive fields are elongated and approximately rectangular, with one long side being excitatory subregions or ON subregions and the other being inhibitory subregions or OFF subregions. The two subregions are aligned along its preferred orientation. If cortical cells have such receptive fields, they are called simple cells, which are proposed by Hubel and Wiesel, according to the classical model they suggested. In this model, the receptive fields of ON cells and OFF cells in LGN are superimposed partly to form the receptive fields of simple cells.

How do the receptive fields of simple cells emerge during the development of animals? The arguments focus on genetically coding or activity-dependent mechanism. It is unlikely that for cortex a huge number of neurons and synapses can be genetically arranged to form the structures of neuronal orientation selectivity. The activity-dependent learning assumption says that the formation of receptive field properties are driven by neural activity during the critical period of the development. Starting from Malsburg (1973), several mathematical models have been proposed to describe the activity-dependent learning process as a self-organization process using a Hebbian learning rule (R.Linsker, 1986a; R.Linsker, 1986b; R.Linsker, 1986c). In order to describe the emergence of orientation-selective receptive fields of simple cells, K.D.Miller (1994) introduce a mathematical model of linear differential equations for the Hebbian learning developmental process. The key element of this model is the correlation function of the activity of LGN. Miller suggests that this correlation function must have a zero crossing so that the orientation selectivity

can emerge. Van Hemmen studied a new model based on the Miller model. They derived the eigenfunctions associated with the learning equation. The eigenfunctions determine the shape of the receptive fields and also the cortical map structure. We call this model proposed by van Hemmen as van Hemmen model. We use this model to describe and analyze the developmental process of orientation-selective receptive fields of Bednar model, to see if this Miller and Hemmen's framework work for the Bednar model, so that we can obtain some new insights for the emergence of orientation selectivity.

3.2 Van Hemmen Model

Now we will introduce how Van Hemmen model is built step by step according to the basic biological structures and the activity-dependent learning process.

Since Hubel and Wiesel proposed a classical model which states the receptive fields of simple cells consist of LGN cells aligned along, we adopt this view and assume the orientation selectivity is generated related to the convergence of LGN inputs. Then we need to consider the connection weights between LGN and the primary visual cortex. We neglect retinal activity and focus on LGN and V1 based on Hubel and Wiesel's proposal.

Van Hemmen model considers firing-rate to describe response properties of modeling neurons. The V1 neurons receive inputs from both of LGN cells and other cortical cells. Both of LGN ON or OFF channel and V1 are regarded as two-dimensional sheets. The positions of cells are denoted as two-dimensional vectors. The vector $x=(x,y)$ denotes the position of a cell on the cortical sheet and $\alpha=(\alpha,\beta)$ labels a position on the LGN sheet; the basic structure is shown on Figure 3.1.

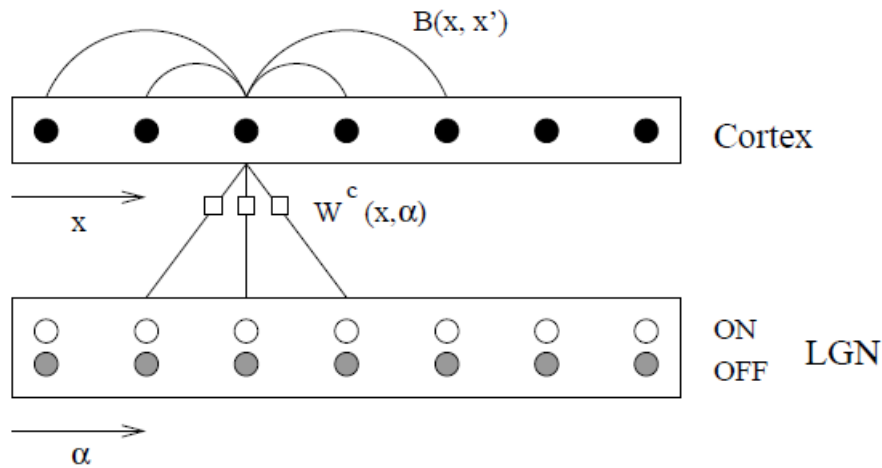


Figure (3.1) This scheme shows the connections between cortical simple cells and LGN neurons, and the connection between cortical cells themselves. The LGN inputs are weighted by the synapse $W^c(x, \alpha)$. Besides the responses of other cortical cells also contribute to the firing rates of simple cells and $B(x, x')$ denotes the interaction strength. The assumption says only the weights between LGN and the cortex are learned during development (adapted from S.Wimbauer, W.Gerstner, and J.L.Hemmen (1998)).

For LGN cells, we use $L(x, y)$ to represent their firing rates, and $W(x, \alpha)$ to represent the connection weights between LGN and V1 cells. For cortical cells, we use $V(x, y)$ to express their firing rates, and $B(x, y)$ to express the connection weights with other

cortical cells. Thus, we can obtain an equation to express the firing rate of cortical cells which has a linear relationship with firing rates of LGN cells and other V1 cells.

$$V(x, t) = \sum_{c=ON,OFF} \sum_{\alpha} W^c(x, \alpha) L^c(\alpha, t) + \sum_{x'} B(x, x') V(x', t) \quad (1)$$

We can rewrite this equation as this following form:

$$V(x, t) = \sum_{x'} I(x, x') \sum_{c=ON,OFF} \sum_{\alpha} W^c(x', \alpha) L^c(\alpha, t) \quad (2)$$

Here $I(x, x')$ satisfies :

$$I^{-1}(x, x') = 1 - B(x, x') \quad (3)$$

the I^{-1} denotes the inverse of the matrix I. In this model to be simple they assume that the long-time average of the rates $L(x, y)$ to be zero. In other words, they regard $L(x, y)$ as the difference between the momentary firing rate and the average firing rate. But when we apply this model to the Bednar model, we take $L(x, y)$ as the responses of neurons.

Hebbian learning is a rule of activity-dependent synaptic plasticity that if the activation of pre- and post-synaptic neurons are correlated, their synaptic connection will be strengthened. The learning principle was first proposed by D.O.Hebb (1949), who postulated that if a neuron A could successfully repeatedly activate a postsynaptic neuron B when A itself is active, then A will gradually become more effective in activating neuron B. In the model on consideration only synapses between the LGN and the cortex are modified by Hebbian learning, whereas intracortical synapses are kept no change. We will examine how the synaptic weights W change with the correlation between the response functions of LGN and the cortical neurons. We assume at average level W at time t is determined by the correlation of LGN responses and firing activity of V1 during a time window Λ . Thus:

$$\frac{dW^c(x, \alpha, t)}{dt} = \eta A(x - \alpha) \frac{1}{\Lambda} \int_0^{\Lambda} ds V(x, t - s) L^c(\alpha, t - s) \quad (4)$$

The arbor function, A tells how many synapses connecting LGN neurons to V1 to be modified. Combine this equation with (2) we obtain:

$$\frac{dW^c(x, \alpha, t)}{dt} = A(x - \alpha) \sum_{x'} I(x, x') \sum_{c=ON,OFF} \sum_{\alpha'} C^{c,c'}(\alpha, \alpha') W^{c'}(x', \alpha', t) \quad (5)$$

In this equation C is the correlation function between the responses of two neurons in the LGN, given by:

$$C^{c,c'}(\alpha, \alpha') = \frac{\eta}{\Lambda} \int_0^{\Lambda} ds a^c(\alpha, s) a^{c'}(\alpha', s) \quad (6)$$

From the deduction of (5) we make two additional assumptions. One is we have $W(t)$ instead of $W(t - s)$, this is because we assume W change very slowly during this time window and can be regarded as fixed. Secondly, for the correlation function of LGN activity, we remove t factor since we want to have averaging effect over time and also the randomness of LGN responses, so the correlation C doesn't relate to time t . Now we need to specify the elements in equation (5), where there are the arbor function $A(x - a)$, the intracortical interaction function $I(x, x')$ and the correlation function of LGN cell responses, C . In the following the arbor function is given

by a Gaussian:

$$A(x - \alpha) = \exp\left(-\frac{|x - \alpha|^2}{2A}\right) \quad (7)$$

This function makes synapses change in a distance $|x - \alpha|$. Also, the excitatory interaction between cortical neurons are chosen to be a Gaussian:

$$I(x, x') = \exp\left(-\frac{|x - x'|^2}{2I}\right) \quad (8)$$

Based on the research of K.D.Miller (1994), as a function of the distance $|\alpha - \alpha'|$ the correlation function of the activity of two neurons at positions α and α' on the LGN should change sign at least one time to let the orientation selectivity to emerge. So here by inducing a sign change, the correlation functions are proposed as following:

$$\begin{aligned} C^{ON,ON}(\alpha, \alpha') &= C^{OFF,OFF}(\alpha, \alpha') = \exp\left(-\frac{|\alpha - \alpha'|^2}{2C}\right) - k \\ C^{ON,OFF}(\alpha, \alpha') &= C^{OFF,ON}(\alpha, \alpha') = -\epsilon C^{ON,ON}(\alpha, \alpha') \end{aligned} \quad (9)$$

where $0 \leq k \leq 1$ and $0 \leq \epsilon \leq 1$. For $k = 0$ the correlation function $C^{ON,ON}$ is a positive function whereas for $k > 0$ the value of the function has a zero crossing at some finite distance. According to the knowledge of ordinary linear differential equation, we can know the solution of equation (5) $W^c(x, \alpha, t)$ can be expressed by eigenfunctions $W_a^c(x, \alpha)$:

$$W^c(x, \alpha, t) = \sum_a c_a(0) \exp(\lambda_a t) W_a^c(x, \alpha)$$

Based on the analysis of Wimbauer et al.(1998), positive eigenvalues λ_a always exist and this may lead synaptic weights would increase to infinity. To avoid such behavior of synapses we need to set bounds for $W^c(x, \alpha, t)$:

$$0 \leq W^c(x, \alpha, t) \leq W_{max} A(x - \alpha)$$

With the largest eigenvalues the eigenfunction components will firstly reach the bound. So the receptive fields will be determined by the eigenfunctions for the largest eigenvalues.

The equation was solved and the solution was obtained. The eigenfunctions corresponding to receptive fields are shown in Figure 3.2. These functions mimic the shapes of receptive fields observed in experiments. They confirmed that in their equations, in order to get orientation-selective receptive fields, the correlation function of the LGN inputs must have a zero crossing.

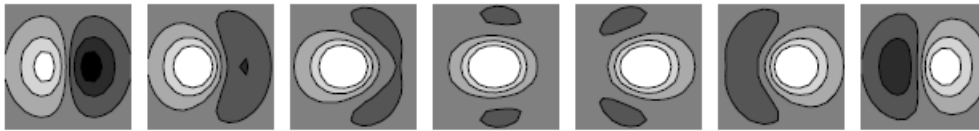


Figure (3.2) The eigenfunction corresponding to the largest eigenvalue (adapted from S.Wimbauer, W.Gerstner, and J.L.Hemmen (1998)).

3.3 Using Van Hemmen model to study Topographica model

To understand the reason why the receptive fields emerge during the development process in Topographica model, we would be able to capture the instability framework of Van Hemmen model to describe the formation of receptive fields. One of the key elements for van Hemmen model is correlation functions of LGN activity. In the Bednar model, the correlation functions of LGN inputs are not simply Gaussian as (9), but acquired from calculations based on relevant data.

3.3.1 The correlation function of LGN activity for Topographica model

We use correlation coefficient formulas to calculate the correlation function of ON and Off cells' responses.

$$\rho_{xy} = \frac{Cov(x,y)}{\sigma_x \sigma_y}, \quad \text{where } Cov(x,y) = E[(x - E(x))(y - E(y))] \quad (10)$$

σ_x and σ_y are standard deviations of x and y , respectively. By averaging, e.g. 2000 sheets of LGN units' responses, we calculate the mean correlation functions. The plots of correlation functions of ON and ON neurons, ON and OFF neurons, OFF and OFF neurons, respectively, are not shown here. We fit the 3 functions by using 3 mixed Gaussian type functions. We consider the cases when aspect ratio of Gaussian stimuli equal 1 and 3.4, since previous results show the orientation selectivity changes significantly from aspect ratio 1 to aspect ratio 3.4. When aspect ratio =1, the fitting functions for correlation functions are:

$$F_1^{ON,ON}(x) = A \exp\left(\frac{-x^2}{2\sigma_1^2}\right) \quad (11)$$

In this equation, $A = 1.006$, $\sigma_1 = 1.562$.

$$F_1^{ON,OFF}(x) = 0.7 \exp\left(\frac{-x^2}{\sigma_2^2}\right) - \frac{2.1}{\gamma_2^2} \exp\left(\frac{-x^2}{\sigma_3^2}\right) + \gamma_3 \quad (12)$$

In equation(12), $\sigma_2 = 5.827$, $\gamma_2 = 1.673$, $\sigma_3 = \gamma_2^2$, $\gamma_3 = -0.023$.

$$F_1^{OFF,OFF}(x) = 1.0674 \exp\left(\frac{-x^2}{2\sigma_4^2}\right) - 0.155x^2 \exp\left(\frac{-x^2}{2\sigma_5^2}\right) + 6.142 \times 10^{-3} x^4 \exp\left(\frac{-x^2}{2\sigma_6^2}\right) + 2.506 \times 10^{-5} x^6 \exp\left(\frac{-x^2}{2\sigma_7^2}\right) + A_1 \exp\left(\frac{-x^2}{2\sigma_8^2}\right) + B \quad (13)$$

In equation (13), $\sigma_4 = 2.27$, $\sigma_5 = 0.124$, $\sigma_6 = 1.998$, $\sigma_7 = 3.34$, $\sigma_8 = 532.66$, $A_1 = -532.756$, $B = -3319.515$. When aspect ratio =3.4, the fitting functions for correlation functions are:

$$F_2^{ON,ON}(x) = A_2 \exp\left(\frac{-x^2}{2\sigma_9^2}\right) + B_1 \quad (14)$$

In this equation $A_2 = 0.954$, $\sigma_9 = 2.199$, $B_1 = -0.014$

$$F_2^{ON,OFF}(x) = 0.7 \exp\left(\frac{-x^2}{\sigma_9^2}\right) - \frac{2.1}{\gamma_4^2} \exp\left(\frac{-x^2}{\sigma_{10}^2}\right) + \gamma_5 \quad (15)$$

In equation (15), $\sigma_9 = 6.844$, $\gamma_4 = 1.713$, $\sigma_{10} = \gamma_4^2$, $\gamma_5 = -0.035$.

$$F_2^{OFF,OFF}(x) = 1.056 \exp\left(\frac{-x^2}{2\sigma_{11}^2}\right) - 0.162x^2 \exp\left(\frac{-x^2}{2\sigma_{12}^2}\right) + 2.185 \times 10^{-3}x^4 \exp\left(\frac{-x^2}{2\sigma_{13}^2}\right) + 9.687 \times 10^{-6}x^6 \exp\left(\frac{-x^2}{2\sigma_{14}^2}\right) + A_3 \exp\left(\frac{-x^2}{2\sigma_{15}^2}\right) \quad (16)$$

In equation (16), $\sigma_{11} = -2.345$, $\sigma_{12} = 0.125$, $\sigma_{13} = 2.175$, $\sigma_{14} = 3.807$, $\sigma_{15} = 46.444$, $A_3 = -0.09$.

3.3.2 The calculation process

In this section we will solve the eigenvalue problem corresponding to the learning equation(5),

$$\lambda W^c(x, \alpha) = A(x - \alpha) \sum_{x'} I(x, x') \sum_{c=ON,OFF} \sum_{\alpha'} C^{c,c'}(\alpha, \alpha') W^{c'}(x', \alpha') \quad (17)$$

Then we obtain

$$\lambda W^c(x, \alpha) = \exp\left(-\frac{|x - \alpha|^2}{2D}\right) \int dx' \int d\alpha' \exp\left(-\frac{|x - x'|^2}{2I}\right) \sum_{c'=ON,OFF} C^{c,c'}(\alpha, \alpha') W^{c'}(x', \alpha') \quad (18)$$

thus we have:

$$\lambda W^{ON}(x, \alpha) = \exp\left(-\frac{|x - \alpha|^2}{2D}\right) \int dx' \int d\alpha' \exp\left(-\frac{|x - x'|^2}{2I}\right) \sum_{c'=ON,OFF} C^{ON,c'}(\alpha, \alpha') W^{c'}(x', \alpha') \quad (19)$$

$$\lambda W^{OFF}(x, \alpha) = \exp\left(-\frac{|x - \alpha|^2}{2D}\right) \int dx' \int d\alpha' \exp\left(-\frac{|x - x'|^2}{2I}\right) \sum_{c'=ON,OFF} C^{OFF,c'}(\alpha, \alpha') W^{c'}(x', \alpha') \quad (20)$$

Let $W = (W^{ON}, W^{OFF})$, so

$$\lambda W(x, \alpha) = \exp\left(-\frac{|x - \alpha|^2}{2D}\right) \int dx' \int d\alpha' \exp\left(-\frac{|x - x'|^2}{2I}\right) \begin{pmatrix} C^{ON,ON}(\alpha, \alpha') & C^{ON,OFF}(\alpha, \alpha') \\ C^{OFF,ON}(\alpha, \alpha') & C^{OFF,OFF}(\alpha, \alpha') \end{pmatrix} W(x', \alpha') \quad (21)$$

we use variable $\Delta\alpha = \alpha - x$, and let $C = \begin{pmatrix} C^{ON,ON} & C^{ON,OFF} \\ C^{OFF,ON} & C^{OFF,OFF} \end{pmatrix}$, so

$$\lambda W(x, \Delta\alpha) = \exp\left(-\frac{|\Delta\alpha|^2}{2D}\right) \int dx' \int d\alpha' \exp\left(-\frac{|x - x'|^2}{2I}\right) C((x - x') + (\Delta\alpha - \Delta\alpha')) W(x', \Delta\alpha') \quad (22)$$

We replace the integral by a sum. Let $\vec{x}'_{i,j} = (\Delta i', \Delta j')$, $\vec{\Delta\alpha}'_{k,l} = (\Delta k', \Delta l')$ then we can have

$$\lambda W_{ijkl} = \exp\left(-\frac{(\Delta k)^2 + (\Delta l)^2}{2D}\right) \sum_{i',j',k',l'} (\Delta i')(\Delta j')(\Delta k')(\Delta l') \exp\left(-\frac{(\Delta i - \Delta i')^2 + (\Delta j - \Delta j')^2}{2I}\right) C((\Delta i - \Delta i' + \Delta k - \Delta k', (\Delta j - \Delta j' + \Delta l - \Delta l')) W_{i'j'k'l'} \quad (23)$$

Let $A_{ijkl'i'j'k'l'} = \exp(-\frac{(\Delta k)^2 + (\Delta l)^2}{2D}) \exp(-\frac{(\Delta i - \Delta i')^2 + (\Delta j - \Delta j')^2}{2I}) C((\Delta i - \Delta i' + \Delta k - \Delta k', (\Delta j - \Delta j' + \Delta l - \Delta l'))$,
 then we have

$$\lambda W_{ijkl} = (\Delta i')(\Delta j')(\Delta k')(\Delta l') \sum_{i',j',k',l'} A_{ijkl'i'j'k'l'} W_{i'j'k'l'} \quad (24)$$

We assume an odd number N , then $i, j, k, l, i', j', k', l' \in \{-\frac{N-1}{2}, \dots, \frac{N-1}{2}\}$.

To solve (23) we can use the eigenvalue functions of python. Combine (13),(14) and (15), set $\Delta i', \Delta j', \Delta k', \Delta l' = 0.05$ and know $D = 0.27 * 0.27, I = 0.025 * 0.025$, theoretically we can solve (23) and get the eigenvalues λ and the corresponding eigenvectors W . But in simulations we meet computing problem which is about our current computer memory doesn't support the so large matrix calculation.

So with this unsolved problem we still don't know if the framework of Van Hemmen model appears suitable to reveal the mechanism of the emergence of orientative receptive field in the Topographica model.

Chapter 4

A study of the basic Topographical model

4.1 Introduction

The brain can change dramatically during learning and development yet remains structurally stable. Many studies support this viewpoint (for a review, see H.Lütcke, Margolis, and Helmchen (2013)). In vivo long-term imaging has revealed that synaptic plasticity in adult brains may involve the strengthening or weakening of existing synapses as well as synapse formation and elimination. In the hippocampus, recent studies revealed that around 80% of the cells change their tuning properties over a timescale of a week (T.Hainmueller and Bartos, 2018; T.Bonhoeffer, M.Huebener, and T.Rose, 2017). The zebra finch, for example, sings a highly stereotyped song that is stable for years, but the neuron patterns underlying song shift from day to day (for a review, see M.S.Brainard and A.J.Doupe (2000)). Visual cortex, is a model for plasticity of cortical circuits (D.H.Hubel and T.N.Wiesel, 1962; D.H.Hubel and T.N.Wiesel, 1963b; B.A.Wandell and S.M.Smirnakis, 2009; J.S.Espinosa and M.P.Stryker, 2012; Ko et al., 2011; L.White and D.Fitzpatrick, 2007; M.Sur and C.A.Leamey, 2001; Y.Frégnac et al., 1988; Y.Frégnac, S.Thorpe, and E.Bienenstock, 1992). Visual features selectivity acquired around and after eye opening. The synaptic architecture of visual cortex remains plastic lasting several months after the initial orientation selectivity is established (J.T.Chang, D.Whitney, and D.Fitzpatrick, 2020). Many experimental observations indicate that the development of orientation selectivity involves a process of experience-dependent plasticity (for a review, see J.S.Espinosa and M.P.Stryker (2012)). Sensory maps can undergo plastic changes with experience. The deprivation of visual experience can cause the degradation of orientation selectivity. In fact receptive fields can be extremely plastic in V1. For instance, one study demonstrated that using a STDP protocol can induce rearrangement of cortical neuron's sub-threshold and supra-threshold responses by only dozens of spikes (V.Pawlak et al., 2013). During an hour cortical neuron fires thousands of spikes. Whether and why the selectivity persists under this continuous stream of activity is not well understood and has not frequently been investigated in theoretical models.

Using pattern formation approach, Wolf and coworkers investigated a class of abstract mathematical models to determine the conditions for realistic orientation maps generation modelling activity-dependent self-organization (F.Wolf, 2005; M.Kaschube et al., 2010a; F.Wolf and T.Geisel, 2003). They found predicted maps exhibiting all the statistics of the common design with dynamical stability and robustness if the long-range neuronal interaction extending beyond one hypercolumn are present in the models. W.Keil and F.Wolf (2011) using this mathematical approach examined the Elastic Network model and found that in previous studied regimes, the ground states of OPM layouts are periodic patterns. Only in an extreme limit aperiodic maps

which resemble the representations of v1 in real animals were found. Also in this model non-local neuronal interaction are essential for layout stabilization. L.Reichl et al. (2012) studied a coordinated optimization model for the interaction between orientation map and other types of maps and discovered that maps typically undergo substantial rearrangement and pinwheel crystals and stripes dominate in the final layouts. In particular, this study examined the time scales on which map optimization takes place and how these time scales can be compared to those of visual cortical development and plasticity.

To answer whether the common design features emerge as a consequence of random connectivity for feedforward projections from retinal ganglion cells to cortical target neurons, M.Schottdorf et al. (2015b) generalized and examined the stochastic wiring model proposed by Ringach and coworkers and found that the random wiring framework could not reproduce the experimentally observed layout invariants. So far only the long-range interaction model can reproduce the common design features. This model however lacks biological detail about how activity patterns drive the self-organization process. Nevertheless, it is natural to expect microscopically detailed models consistent with the long-range interaction model, in the sense that cortical activity patterns excite larger regions instead of the classical receptive fields and accordingly might need to be driven by complex scene stimuli rather than simple stimuli only activating the classical receptive field of a small number of neurons. Therefore, realistic inputs such as natural scene stimuli are required to activate widely distributed cortical activity and strong non-local neuronal connections are necessary for the maturation of V1 architecture.

To test both of these hypotheses, for the first time, we use a detailed network model with Hebbian-learning to simulate the development process of OPMs. We use realistic inputs to drive the map development process over realistically long-term time scales. In biology the relevant long time scales can be compared to so called "critical period" of animal brains' plasticity for sensory experience.

4.2 Materials and Methods

4.2.1 Orientation selectivity calculation: Vector average method

The calculation of orientation selectivity is based on the vector average method (Blasdel and Salama(1986)). Inputs that cover the full range of parameter values, e.g. combinations of orientations, frequencies, and phases, are presented, and for each value of the parameter, the peak response of the neuron is recorded. To calculate the preferred orientation, for each orientation ϕ , other parameters such as phase and spatial frequency are varied systematically, and the peak response $\hat{\eta}_\phi$ is recorded.

Then a vector is obtained for each orientation ϕ . with $\hat{\eta}_\phi$ as its length and 2ϕ as its orientation, and these vectors are summed together to form vector

$$V = [V_x, V_y]$$

The preferred orientation of the neuron,, is computed as half the orientation of V :

$$V_x = \sum_{\phi} \hat{\eta}_\phi \cos 2\phi, V_y = \sum_{\phi} \hat{\eta}_\phi \sin 2\phi$$

The magnitude of V can be regarded as an estimate for orientation selectivity; normalized selectivity S would be:

$$S = \frac{\sqrt{V_x^2 + V_y^2}}{\sum_{\phi} \hat{\eta}_{\phi}}$$

4.2.2 Pinwheel tracking

During the evolution of maps we analyzed the states using about hundred time frames from the initial time $T = 0$ to the very late state, i.e. every time frame for $t = N \times T^*$ ($N = 1, 2, 3, \dots$). We tracked all the pinwheel centers and calculated the pinwheel density as well as various other pinwheel statistics. Pinwheel centers were located as the intersection of the zero contours of the real and imaginary components in the polar representation of orientation preference. The pinwheel density was defined as the average number of pinwheels per hypercolumn Λ^2 . Defined in this way the pinwheel density is dimensionless and characterizes the layout of orientation columns independent of their absolute size. To calculate distributions of nearest neighbor distances of pinwheels with arbitrary charge we identified for each pinwheel i in a given map the distances d_{ij} to all neighbors j with arbitrary topological charge. We minimize the distances to find the nearest neighbors and the distances are measured in units of column spacing. For distances d_{ij} between pinwheels with the same (opposite) charge, we consider the distances d_{ij} of pinwheel i to all pinwheels j with the same (opposite) charge.

To calculate pinwheel density variability in subregions of size A , we sampled for each map circular shaped regions of various size and placed their centers at random locations of the map. Sizes of circular regions were uniformly distributed. To calculate pinwheel density variability for a given area A_i , we randomly selected from all regions in the set up to 1000 regions with size in the interval $[A_i, A_i + dA]$ where $dA = \min\{|A_{i+1} - A_i|, 0.1\Lambda^2\}$, and calculated the standard deviation SD of pinwheel densities. Next, we estimated the variability coefficient c and the exponent γ by fitting the empirically observed power law $SD(A) = c(\langle \rho \rangle / A)^{\gamma}$ to the $SD(A)$ -curves.

To track pinwheels and find corresponding pinwheels between two time steps, pinwheels in two consecutive time frames were detected using a pinwheel finder. For each pinwheel in the first map, a list of potential corresponding pinwheels in the second map is made. This is based both on distance (must be much smaller than an hypercolumn) and on pinwheel sign (must be equal). Those lists are combined into separated optimization sub-problems. In each problem a set of pinwheels in the first map that must be mapped to a set of pinwheels in the second map. Each sub-problem generally involves a very small amount of pinwheels. This is because the pinwheels have a typical distance in a map and the search distance is lower than that. Since the subproblems are small, each is solved by minimizing the total distance between matched pairs. This is done via recursive programming (i.e. brute force). Once a list of matched pinwheels is made, with the remaining pinwheels the same procedure is used to make a list of annihilated/generated pinwheels. It works the same, only that the criteria of possible pinwheels requires them having opposite sign and to be in the same time step. Finally, all pinwheels that could not be labeled as matched or annihilated or generated are given the labels lost or new. When tracking pinwheels in multiple time steps, a table was generated with columns corresponding to time steps and rows corresponding to matched pinwheels. The tracking

results between two steps described above was used to fill the table. When a pinwheel gets annihilated or lost, its location in space was saved. When a pinwheel was generated or new, it was checked if the location matches one of the lost pinwheels. If they do, they are annotated in the same row. Motivation: This is required because one can have a pinwheel pair that annihilates at time t and generates after a brief time in time $t + dt$. With this procedure the pinwheels are assigned same ID, not a new one. Once the table is complete, the next step is to give unique pinwheels IDs. Usually they simply correspond to the rows of the table, but they can be complications which are treated separately.

We define the pinwheel creation $c(t)$ and annihilation rate $a(t)$ per hypercolumn as:

$$c(t) = \frac{dN_c}{Mdt}, a(t) = \frac{dN_a}{Mdt}, M = \frac{A}{\Lambda^2}$$

where N_c and N_a are the numbers of created and annihilated pinwheels, A is the size of a map and Λ is a average wavelength of the map.

4.2.3 Simulation Procedure

A Retinal input layer was represented by "Photoreceptor" sheet by a two dimensional array of units. The sheet has a pair of 'sheet coordinates' (x, y) , floating-point cartesian coordinates indicating an arbitrary point on the sheet's plane. In simulations the sheet was implemented using a finite matrix of units. First we specified the value of the parameter "density", which gives the number of elements in the matrix corresponding to a length of 1.0 in continuous sheet coordinates. Then a "sheetcoordinatesystem" converts sheet coordinates to matrix coordinates, as well as sheet index coordinate to matrix index coordinates. The bound of sheet set as a square and the area was given as 3.75×3.75 . The density was 24. So when elongated and oriented Gaussian pattern is sampled, firstly the pattern coordinate matrix is produced from the bound and density, then transformed and rotated according to the center (x, y) and orientation of the Gaussian. In every iteration we choose two Gaussian combined, with positions and orientations uniform random chosen from interval $[-(\sqrt{v1_area}/2 + 0.25), (\sqrt{v1_area}/2 + 0.25)]$ and $[-\pi, \pi]$, respectively. $v1_area$ was the size of the model cortical area. The size of single Gaussian stimuli was 0.088388 and its aspect ratio 4.66667. The contrast was defined as 70%. So the response value of a unit in the Retina was given by $70\% \times$ of the Gaussian function value of the unit.

The projection from the Retina to LGN ON or OFF cells consisted of separate connection fields, each of which is a spatially localized set of connections from neurons in Retina near the corresponding topographic location of the target neuron. Each connection field had radius 0.375 and shared an identical set of weights.

The LGN level of the visual system was represented by ON and OFF sheets, both of which had density as 24 and radius as $0.5 * \sqrt{v1_area} + 0.75$. The response of LGN cells is defined by

$$\eta_{j,O}(t + \delta t) = f\left(\frac{\gamma_O \sum_{i \in F_{j,p}} \Psi_i(t) w_{i,j}}{k + \gamma_s \sum_{i \in F_{j,s}} \eta_{i,O}(t) w_{i,j,s}}\right)$$

Here, the constant $\gamma_0 = 14, k = 0.11$ and $\gamma_s = 0.6$. Ψ_i is the activation value of unit i on retina from which ON/OFF unit j receives input and its afferent connection field is $F_{j,p}$. $\eta_{i,O}(t)$ is the activation of other units in ON/OFF sheets on the previous step and received over the connection field $F_{j,s}$. The function f is a half-wave rectifying

function which removes the negative part of the activation and ensures that $\eta_{j,O}$ is always positive. The width of the central Gaussian is defined by 0.037, and the width of the surround Gaussian by 0.15. The weights in the denominator define the local inhibition for every units of LGN and share the same Gaussian profile with width 0.125 and normalization. The radius of the suppressive connection field is given as 0.25. This type of inhibition can be switched on or off for particular simulations. The connection fields between LGN and primary visual cortex (V1) had 0.27083 as radius. Neurons in V1 near the border would have afferent connections that extend over the border of LGN sheets, so the connection fields for these neurons are truncated to be restrained in the projection area. This truncation of connections may result in artifacts for map formation. A strategy to avoid this kind of effect, is to impose periodic boundary conditions to the connection fields and Retina. Such simulations are examined later. In this section we just use open boundary conditions. The initial weights are generated by a random Gaussian Cloud function. These weights can be updated by a Hebbian learning rule

$$w_{ij,p}(t) = \frac{w_{ij,p}(t-1) + \alpha \eta_i \eta_j}{\sum_k (w_{kj,p} + \alpha \eta_j \eta_k)}$$

The factor α is the learning rate, defined by a constant (e.g. 0.1) divided by the number of connections per connection field.

For V1, we set the area size as 1.5 and the density as 49. Every unit of V1 has 3 type of connections with other units, one is with LGN ON or OFF units, another one is for local excitatory interactions and the third one is for local inhibitory interactions within V1. The excitatory and inhibitory connection weights within V1 neurons are also defined using Gaussians in space, with width 0.05 and 0.15, respectively. They can also be learned and for efficient computation, the learning rate of E is given by 0 and of I is constant and given by 0.3. The projection strength scaling factors for each connection type was 1.5 for LGN, 1.7 for excitatory interaction and -1.4 for inhibitory interaction. In addition, the threshold of responses of cortical neurons was chosen adaptive. The corresponding parameter for the homeostatic learning rate set to 0.01, and defined such that the average activity of each neuron was driven towards a the specified target (here we use 0.024).

4.2.4 The model

The Topographica model mimics the main biological structures and developmental processes underlying orientation preference maps in primary visual cortex. In this model, the V1 network is a sheet of $N \times N$ interconnected computational units represented as “neurons”. Each cortical neuron receives external input from two types of LGN cells: ON-center and OFF-center. The LGN neurons in turn receive input from the retina, which consists of $R \times R$ array of photoreceptor cells. In addition to the afferent connections, each cortical neuron has local excitatory and inhibitory connections with other neurons. Excitatory connections have a short range and inhibitory connection have a larger range connecting to nearby units. By a Hebbian mechanism, the intracortical interaction function is determined by intracortical synaptic connections: it is positive between two cortical locations that tend to excite one another, and negative between locations that tend to inhibit one another.

The ON and OFF neurons represent the entire pathway from photoreceptor output transferred to the input for V1, including the ON and OFF processing in the retinal ganglion cells and the LGN. In this model ON and OFF are simply divided into

separate channels and organized into an $L \times L$ array corresponding to the retinotopic organization of the LGN.

Each neuron of LGN and V1 generate an initial response by a weighted sum of neurons' responses in its connection field of afferent input. The intracortical interaction regarded as "Mexican-Hat" type between cortical neurons then form the initial activation activity into a localized cortical pattern. After the pattern has stabilized, the connection weights of cortical neurons are modified based on Hebbian learning rule. As the self-organization progresses, responses of these neurons grow nonlinear interaction set in and weak connections decay. The result is a self-organized structure formation in a dynamical process driven by the input.

The following subsections describe the specific components of GCAL model in more details.

Retina. An input pattern is presented to the model by activating the photoreceptor units in the retina according to the gray-scale values in the pattern. To generate such input patterns, the activity Ψ for photoreceptor cell x_c, y_c is calculated according to:

$$\Psi(x_c, y_c, \theta) = \exp\left(-\frac{((x - x_c)\cos\theta + (y - y_c)\sin\theta)^2}{2\sigma_u^2} - \frac{(-(x - x_c)\sin\theta + (y - y_c)\cos\theta)^2}{2\sigma_v^2}\right) \quad (1)$$

, $(x_c, y_c), \theta$ are random positions and orientation.

ON/OFF sheets. The cells in the ON and OFF channels of the LGN compute their responses as a weighted sum of activity in their receptive fields. More precisely, the activation level η for a unit at position j in an ON/OFF sheet O at time $t + \delta t$ is calculated as

$$\eta_{j,O}(t + \delta t) = f\left(\frac{\gamma_O \sum_{i \in F_{j,p}} \Psi_i(t) w_{ij}}{k + \gamma_s \sum_{i \in F_{j,s}} \eta_{i,O}(t) w_{i,j,s}}\right) \quad (2)$$

Ψ_i is the activation value of unit i on retina from which ON/OFF unit j receives input and its afferent connection field is $F_{j,p}$. $\eta_{i,O}(t)$ is the activation of other units in ON/OFF sheets on the previous step and received over the connection field $F_{j,s}$. The function f is a half-wave rectifying function which removes the negative part of the activation and ensures that $\eta_{j,O}$ is always positive. The $\gamma_O = 14$ is a constant strength for the connections from the photoreceptor sheet to the ON/OFF sheet to give the activation level in the range 0.0 to 1.0. If contrast-gain control is not applied, $k = 1$ and $\gamma_s = 0$. If applied, e.g., in the GCL and GCAL models, $k = 0.11$ and $\gamma_s = 0.6$. The weights w_{ij} define the strength of connections from the unit i in Retina to the ON or OFF unit j and is a standard difference-of-Gaussian kernel. The Mexican-hat shape of w_{ij} makes the connection area for ON unit j has positive center and negative surround, and vice versa for OFF units. The mathematical form of the weight w_{ij} from an ON unit j located at (x, y) and the unit i at position (x', y') in Retina is given by:

$$w_{ij}^{ON} = \frac{1}{Z_c} \exp\left(-\frac{(x - x')^2 + (y - y')^2}{2\sigma_c^2}\right) - \frac{1}{Z_s} \exp\left(-\frac{(x - x')^2 + (y - y')^2}{2\sigma_s^2}\right) \quad (3)$$

The width of the central Gaussian is given by $\sigma_c = 0.037$, and the surround Gaussian $\sigma_s = 0.15$. Z_c and Z_s define the normalization constants that make sure the weights sum equal 1.0. The weights for the OFF units are the negative of Equation (3).

Finally, when the contrast-gain control is activated, the weights $W_{ij,s}$ in the Equation (2) define the spatial profile of the lateral inhibitory interactions between unit j and other unit i in the ON/OFF sheet. The weights $W_{ij,s}$ is a fixed, circular Gaussian profile so that the connection between neuron j in the location (x, y) and the presynaptic neuron i in the location (x', y') is given by :

$$w_{ij,s} = \frac{1}{Z_s} \exp\left(-\frac{(x-x')^2 + (y-y')^2}{2\sigma_s^2}\right) \quad (4)$$

where $\sigma_s = 0.125$ and Z_s is a normalizing constant.

The V1 sheet. Each V1 unit receives inputs from connections between ON/OFF sheet and V1, and between V1 neurons. We can call these connections “projections”(p). The projections can be the afferent projection from the ON/OFF sheets($p = A$), or the recurrent lateral excitatory projection($p = E$), and the recurrent lateral inhibitory projection($p = I$).from other V1 units. The activation of unit j in V1 sheet by afferent connections is defined as following:

$$\eta_{j,V}(t) = f\left(\sum_p \gamma_p C_{jp}(t)\right) \quad (5)$$

$$C_{jp}(t + \delta t) = \sum_{F_{jp}} \eta_{i,p}(t) w_{ij,p} \quad (6)$$

The scaling factors for each projection type are $\gamma_A = 1.5$, $\gamma_E = 1.7$, $\gamma_I = -1.4$, to provide a balance between excitation and inhibition, and between afferent and lateral influences, to allow smooth map to form. C_{jp} is the contribution to the activation of unit j from each projection type. $\eta_{j,p}$ is the activation of unit i of ON/OFF sheet or V1 neurons to which unit j is connected (its connection field F_j and $w_{ij,p}$ is the connection weight from unit i in LGN or V1 to unit j in LGN or V1 for the projection p . f is a half-wave rectifying function. After previously mentioned steps from Retina to V1, the final activation of V1 units is the response to the present stimulus in Retina. At this point the response of V1 will be used to update the threshold of V1 units and to update the afferent and lateral inhibitory weights through Hebbian learning rule. Then the activation in V1 will be reset to 0, and then a new pattern will be presented in Retina and thus the next iteration will be started.

Adaptation. The adaptation process is constructed to bring the average activity of every unit in V1 close to a specified value. It consists of two steps. The first step is to calculate a smoothed average of settled activity patterns for each unit j .

$$\overline{\eta_j(t)} = (1 - \beta)\eta_j(t) + \beta\eta_j(t - 1) \quad (7)$$

β is called the smoothing parameter which control the degree of smoothing. The initial value of $\overline{\eta_j(t=0)}$ is the target average V1 unit activity μ which equal 0.024. The threshold is updated as follows:

$$\theta(t) = \theta(t - 1) + \lambda(\overline{\eta_j(t)} - \mu) \quad (7)$$

where $\lambda = 0.01$ is the homeostatic learning rate. If the activity in the unit j move away from the specified target, the threshold, according to the Equation (8), will be automatically increased or decreased in order to force it closer to the target.

Learning. The weights of initial connection field are given by isotropic 2D Gaussians for the lateral excitatory projection and uniformly random within a Gaussian envelope for afferent and lateral inhibitory projections. Specifically, a neuron located

at (x, y) has a connection weight from unit i at (x', y') with following value:

$$w_{ij} = \frac{1}{Z_p} u \exp\left(-\frac{(x-x')^2 + (y-y')^2}{2\sigma_p^2}\right) \quad (8)$$

here $u = 1$ for lateral excitatory projection $w_{ij,E}$ and u is a random value chosen from a uniform distribution for the afferent and lateral inhibitory projections $w_{ij,A}$ and $w_{ij,I}$. σ_p defines the width of Gaussian and $\sigma_A = 0.27, \sigma_E = 0.025, \sigma_I = 0.075$, and Z_p is a normalizing factor to ensure the total of all weights w_{ij} equal to 1. When an image is presented to the Retina, the weights $w_{ij,p}$ are updated once per iteration by using a Hebbian learning rule. This rule reflects the correlations between the ON/OFF unit activities and the V1 response activities. The updating procedure of Hebbian connection weights at each iteration dependent on the activities of both presynaptic and postsynaptic units, and the learning rate:

$$w_{ij,p}(t) = \frac{w_{ij,p}(t-1) + \alpha \eta_i \eta_j}{\sum_k (w_{kj,p} + \alpha \eta_j \eta_k)} \quad (9)$$

The Hebbian learning rates for afferent connections, lateral excitatory connections and lateral inhibitory connections are $\alpha_A = 0.1, \alpha_E = 0$ and $\alpha_I = 0.3$, respectively.

4.3 Results

This model mimics the early visual pathway. Figure 4.1(a) shows a simplified diagram of the early visual pathway in the cat. A stimulus placed in front of retina through the cornea and lens, is activating retinal ganglion cell receptive fields and transmitted to the LGN. LGN neurons project to stellate cells in layer IV of V1, which selectively response to stimuli orientations. The orientation selectivity is arranged in patterns of orientation domains, which exhibit a continuous, roughly repetitive arrangement. These patterns are called orientation preference maps.

Figure 4.1(b) illustrates this model consists of four sheets, retina, LGN ON, LGN OFF and V1. Each of them consists of two-dimensional arrays of computational units. Input to the retina can be any type of patterned images, such as small natural image patches. Typically we use four Gaussian stimuli shown here. The difference-of-Gaussian afferent connections from the retina to the ON and OFF units generate a local receptive field on the retina, and give the effect that ON-center units response to light areas surrounded by dark, and OFF-center units response to dark areas surrounded by light. V1 units receive afferent input from LGN ON and OFF units, and also receive lateral excitatory and lateral inhibitory connections from nearby units, which lead to the activity patches seen on the V1 sheet.

We find that long time scales are important for OPM development in this model. In experiments, accumulating evidence shows that in the primary visual cortex of several species, orientation selectivity emerged within a few postnatal days around eye opening and subsequently undergoes a critical period of map plasticity and refinement lasting for several weeks. See Figure 4.2. Taking cat as an example, Kaschube and coworkers demonstrated that the spatial arrangement of eye dominance columns in striate cortex is progressively reorganized between the 6th and the 14th postnatal week such that the organization of orientation columns that are reciprocally connected to extra-striate visual cortex and contralateral hemisphere striate

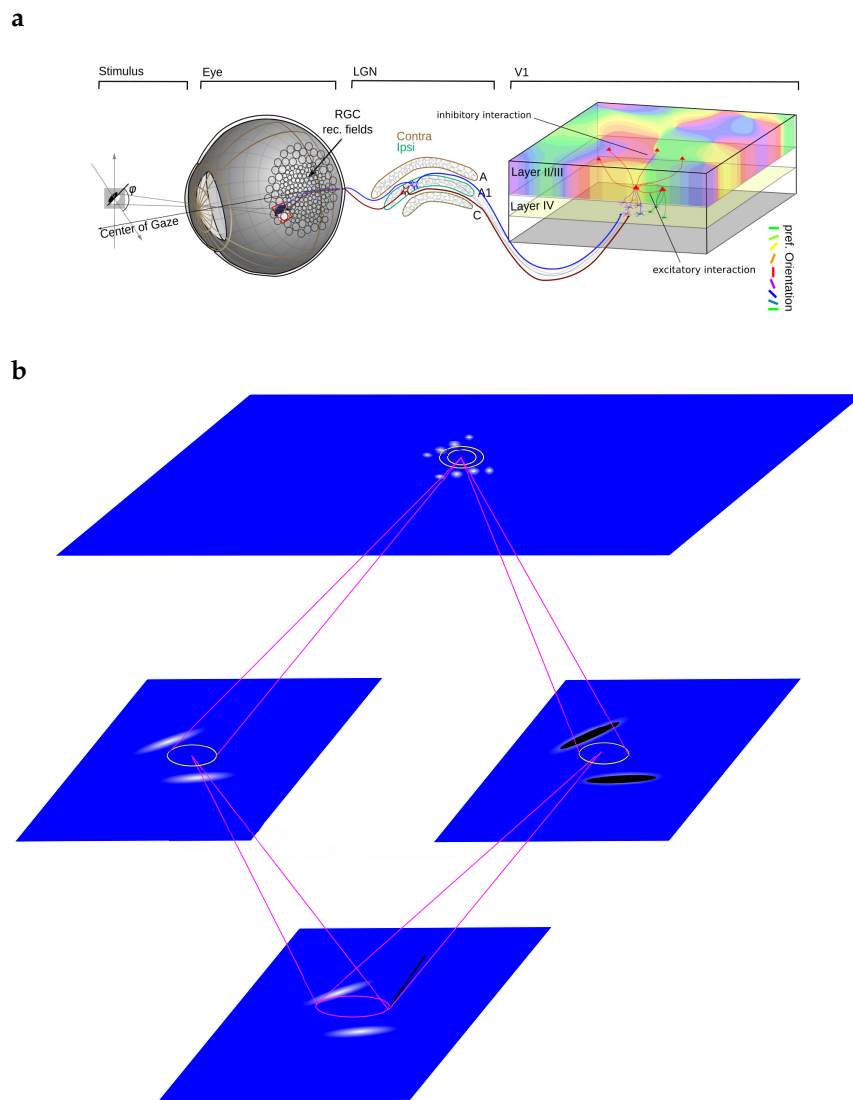


Figure (4.1) The early visual pathway in the visual system(a).The stimulus activates the retina and the signals are transmitted to the LGN.Then LGN projects to V1 for the signals. In V1 the neurons are interacted with inhibitory effects and excitatory effects to response to the orientation selectivity of stimulus.The basic structure of the Topographica model is shown in(b).This model consists of retina,LGN and V1 sheets.The input placed on the retina sheet is 2 Gaussian patterns.The LGN ON sheet responses to the light areas surround by dark areas of stimulus, and the LGN off sheet responses to the dark areas surround by light areas of stimulus. Then the afferent inputs formed by the difference-of-Gaussian from LGN are given to V1.There are 3 types of inputs received by cortical units in V1:the afferent inputs from LGN, the excitatory interaction and the inhibitory interaction between neurons.These input activities generate the “activity bubbles” of the cortical response patterns shown in V1 sheet.

cortex are better matched. For mouse, the duration of the period of cortical plasticity is quite long and extends beyond the third postnatal month. It was showed that neurons in the binocular segment of mouse visual cortex change their preferred orientations during this period. After eye opening, animals will see many images

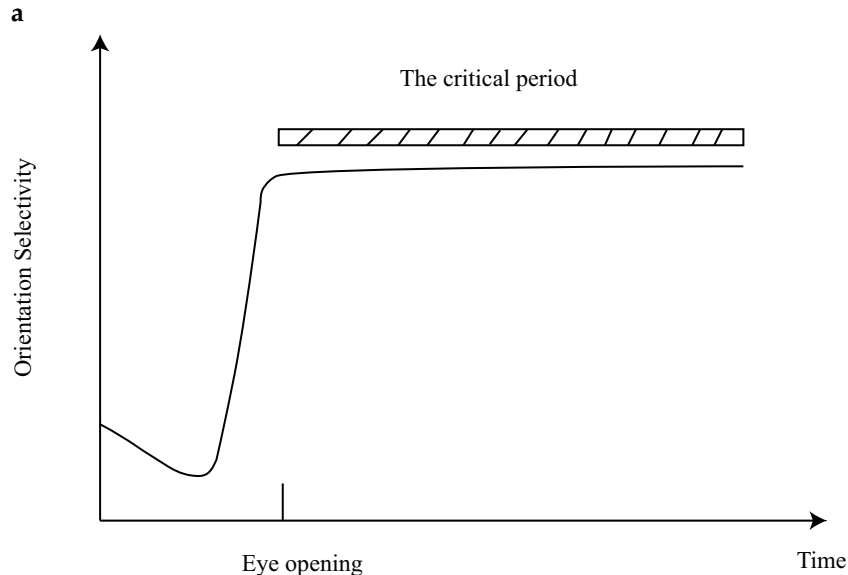


Figure (4.2) A scheme for the critical period since animals open their eyes after their birth. The orientation selectivity firstly decreases and then increases sharply until saturates after animals' eyes opening.

and generate a huge number of spikes in their brain. According to C.D.Meliza and D.Yang (2006) pairing visual stimulation at a given retinal location with post-synaptic spiking can rapidly alter receptive fields in developing rat visual cortex. V.Pawlak et al. (2013) even demonstrated that an STDP protocol using a few dozens of paired APs can transform a neuron's visually evoked responses from non-spiking to spiking and can induce a rearrangement of the neurons sub- and suprathreshold responses to stimuli presented at locations surrounding the paired location. These indicate that when animal's eyes see a large number of images which as stimuli can change the receptive fields in the visual cortex. Imagine just during a few seconds, saccade can take several images. Assume a high firing rate like 10 HZ and low firing rate like 0.1 HZ, we can estimate during a time course how many spikes can be generated. Consistently, we can also estimate how many images can be seen. There are four typical time points. One is the time scale T^* . The three others are the critical period, the time per day not suffered from monocular deprivation which is about 3 hours, and the axon arbor collapsing takes at most 2 days.

In this model an iteration consists of a constant retinal activation from visual activity patterns, followed by transferring to the ON and OFF cells of LGN and processing at the primary cortex. To aid a detailed comparison we are presenting all maps and layout parameters as a function of time. In such displays time is represented in two different ways. One way is based on conventions in the pattern formation literature, time is rescaled with the largest growth rate γ_z of the OP map, $T = \gamma_z * t$. Another way is, to aid comparison with biological observations, we also plot all the measurements of layout characteristics as a function of multiples of the time scale T^* where T^* is the time for which the OP power reaches it peak value or, if there is no peak in the OP power, reaches 90% of its final value. In these units

T^* represents the time when orientation selectivity is essentially mature and later times correspond to subsequent convergence process. From biological perspective, the first stage of the developmental period in which neurons reach adult-like levels of orientation selectivity and the later convergence stage to the following period of developmental juvenile plasticity e.g. until the closure of the developmental critical periods.

We performed time calibration of simulated OPM development for the Topographica model as shown in Figure 4.3(a). We found 20000 time steps to correspond one time scale, T^* . The orientation selectivity firstly decreased, due to the competition of modes outside the circle of positive growth rate similar to Swift-Hohenberg equation models. After this the selectivity exhibits a rapid growth until it saturates. The time scale for growth and saturation depends on model parameters, including afferent learning rate, system size, cortex density, number of gaussian stimuli and so on. For simulations with a different sets of parameters, we firstly redetermined time scale need .

The central question of this study is, how visual cortical networks change after many stimuli have been presented ? As the representation of visual cortex, the orientation preference maps will be used to illustrate this. As shown in Figure 4.3(a), one can see the maps continuously change driven by more and more stimuli presentation. In the initial state the map look noisy and unstructured, but when $t = 1T^*$ it become more banded compared to previous states. When the simulation runs longer than 1 time scale, the organization of orientation maps continued to change. By observation, Orientation maps in the simulations typically became more regular over time. With open boundary conditions, a banded geometry of the orientation domains at the boundaries of V1 increasingly dominates the center of the model area. After a few intrinsic time scales, map layout becomes stripe-like or crystal-like shape with perpendicular direction extended from the borders. To assess this dynamic process, we used the properties pinwheel number, column spacing and pinwheel density. Pinwheel number is the total number of pinwheels in a orientation map area. The pinwheel density is defined as the average number of pinwheels per orientation hypercolumn. The typical column spacing is the average spacing of adjacent iso-orientation columns, by Λ , and the frequency of occurrence of pinwheels per mm^2 by $\hat{\rho}$, then the pinwheel density is given by $\rho = \hat{\rho}\Lambda^2$, where Λ^2 is the area of an orientation hypercolumn. The average pinwheel number decreases during the time course and the pinwheel number reduces strongly during the first 10 intrinsic time scales. The column spacing, or the average wavelength, only changes slightly. These two variables give rise to a fall of the average pinwheel density, which drops to below 3 from about the second time scale.

The dynamics of map organization is driven by pinwheel annihilation and creation. One example of pinwheel annihilation is given in Figure 4.4(a) and another example of pinwheel creation is shown in Figure 4.4(b). How fast are the pinwheels created or annihilated ? The annihilation rate is larger than the creation rate from the beginning and then go to close but still slightly larger than the creation rate. See Figure 4.4(c). How many pinwheels of the pattern in the early stage are still present in the late stage ? For a given set of pinwheels at a early time t we further calculate the fraction of pinwheels surviving until time $t + w$, w can be different time windows. We choose $w = 10, 50$ and $100T^*$. If $w = 10T^*$, we can observe that during the first 10 time scales the surviving fraction is lower than the later period and increases from about 50% to 75%. If $w = 50T^*$, the surviving fraction during the first 10 time scales increase from about 30% to 50%, and then basically keeps a stable level. If

$w = 100T^*$, the surviving fraction is shown as increase from about 20% to 25% during the first 10 time scales and then doesn't change so much. These also indicate the longer time the w is, the smaller pinwheels' surviving fraction until $t + w$. See Figure 4.4(d). For single neurons, their orientation preferences also change due to pinwheel annihilation and creation. We can choose one neuron as an example. During the time course this neuron's preferred orientation continuously change. Especially their receptive fields' orientation can have $\pi/2$ change during the time period from 0 to $25T^*$. See Figure 4.4(e).

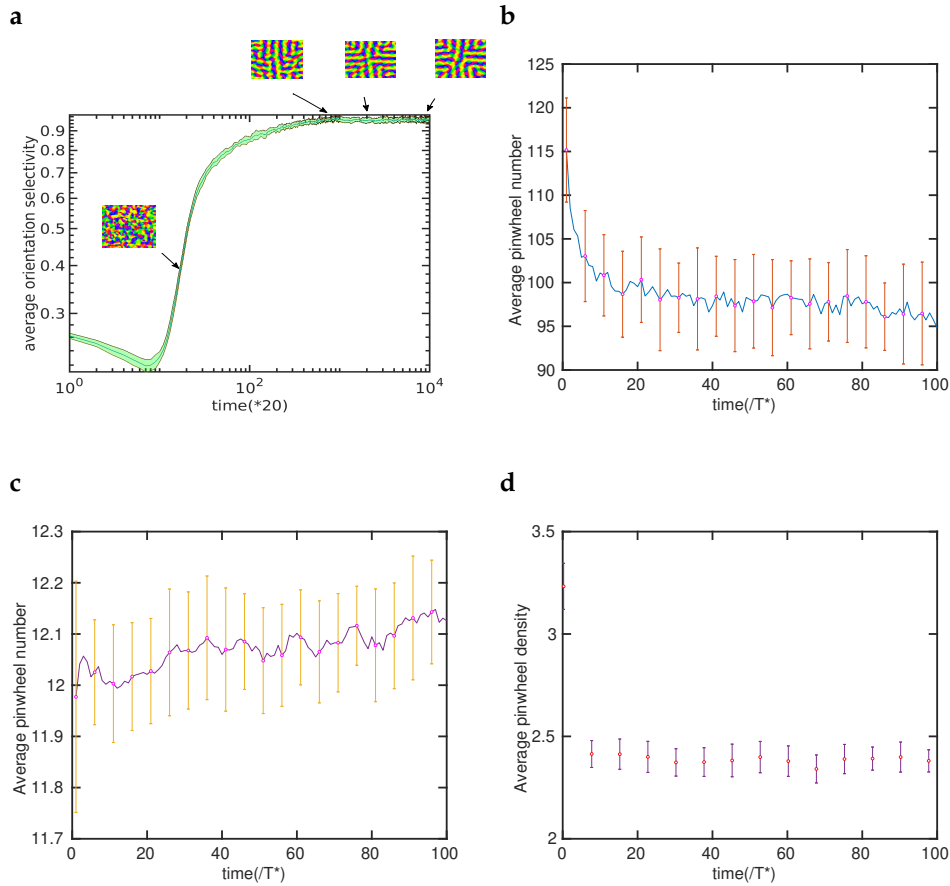


Figure (4.3) Time calibration for maps in the simulation (a). 20000 time steps are equal to 1 time scale. Example maps are exhibited to indicate during the time course the layout of maps is changing. The changes of pinwheel number, average wavelength and mean pinwheel density for maps during the time evolution are shown in (b)(c)(d).

How does the orientation selective pattern emerge from an initially homogenous state and how should this process be characterized? In many physical systems, a new pattern emerges at a critical values of certain control parameters like the critical temperature for liquid-gas transitions. In order to reveal the critical point for map formation, we fixed the stimulus size and performed simulations with different aspect ratio of Gaussian inputs.

The average orientation selectivity(OS) increases as the aspect ratio(AR) of Gaussian stimuli increases. When $AR=1$, OS is the smallest and almost the same value as the initial state. The initial weights give the non-zero OS by the measurement

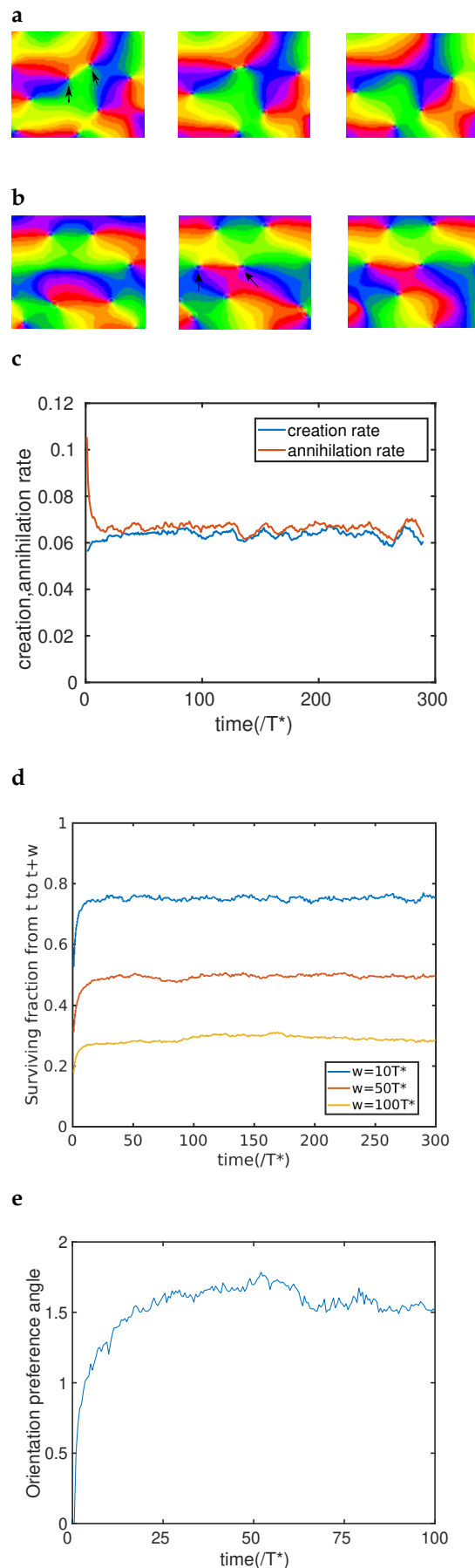


Figure (4.4) An example for pinwheel annihilation (a). An example for pinwheel creation (b). Creation rate and annihilation rate of pinwheels during the map development (c). The fraction of pinwheels surviving during the time course

Figure (4.4) (d).The change of orientation preferences for a single neuron due to the dynamics of pinwheels (e). The receptive field of the neuron can change $\pi/2$ during the time course from 0 to $25T^*$.

method. When AR changes from 1 to 2.8, OS grows slightly, but after that OS rises sharply, with around 3 fold growth of OS for 2.8 to 4 change of AR. See Figure 4.5(a). We also use afferent learning rates (for projection from LGN to V1) 0.05,0.02,0.01 to perform simulations and find that the trends of growth are very similar and OS with learning rate 0.01 has a little more sharper increase when AR changes from 2.8 to 4 than OS with the other learning rates.

We find another phase transition of orientation selectivity for changing the cortical range of excitation, as shown in Figure 4.5(b). We pick two points, one close to the critical point and another one far from the critical point, to examine systematic differences. For 0.25Λ , typical map layouts produced regular crystals which are rhomboid especially for the center of the area. As for conditions far from the critical point which is 0.1Λ , stripes can be seen in the maps generated.

To characterize the phase transition, we examined some key values of parameters impacting map features. We varied aspect ratio, selecting 2.8, 3.4 and 4 as the key points. When aspect ratio =2.8, the average pinwheel density fluctuates massively and the map organization is very poor and changes dramatically during the time course. For aspect ratios 3.4 and 4, the pinwheel density dropped to below 3. See Figure 4.5(c). For an cortical excitatory range, we display the pinwheel densities for the excitatory sigma 0.25Λ , 0.2Λ and 0.1Λ (Figure 5.5(d)). All of them decrease to below 3. When we analyzed the pinwheel creation and annihilation rate. We pick two conditions, one near the critical point and a second far from the critical point. We find that both of creation rate and annihilation rate for aspect ratio 3.4 was slightly higher than for aspect ratio 4. And in the initial state the annihilation rate was larger than the creation rate and in the later stage they approach to each other. A similar analysis for the excitatory range 0.25Λ and 0.1Λ is presented in Figure 5.5(e)(f).

We next systematically calculated the core layout parameters of the common design—pinwheel density and pinwheel nearest neighbor distance distributions for the Bednar model. We evaluated the standard deviation of pinwheel densities as a function of the area A of randomly selected subregions of the iso-orientation domain layouts. The black line represents the SD for 2D poisson process of pinwheel density π . Generally,the standard deviation's decay with subregion size followed a power law with increasing area size. We fitted the empirically observed power law, to the standard deviation of the pinwheel density estimate in increasing subregions of cortical area. At $t = 1T^*$, the pinwheel density variability reveals deviation from SD for a 2D Poisson process of pinwheel density π . During time evolution the deviation continues to become slightly larger. Next we plot pinwheel nearest neighbor(NN) distance distributions of the model. Histograms for NN distances for arbitrary charge and equal charge become more concentrated around half the typical column spacing. Histograms for NN distances for opposite charge deviate from the fitting curve. These results are shown in Figure 4.6.

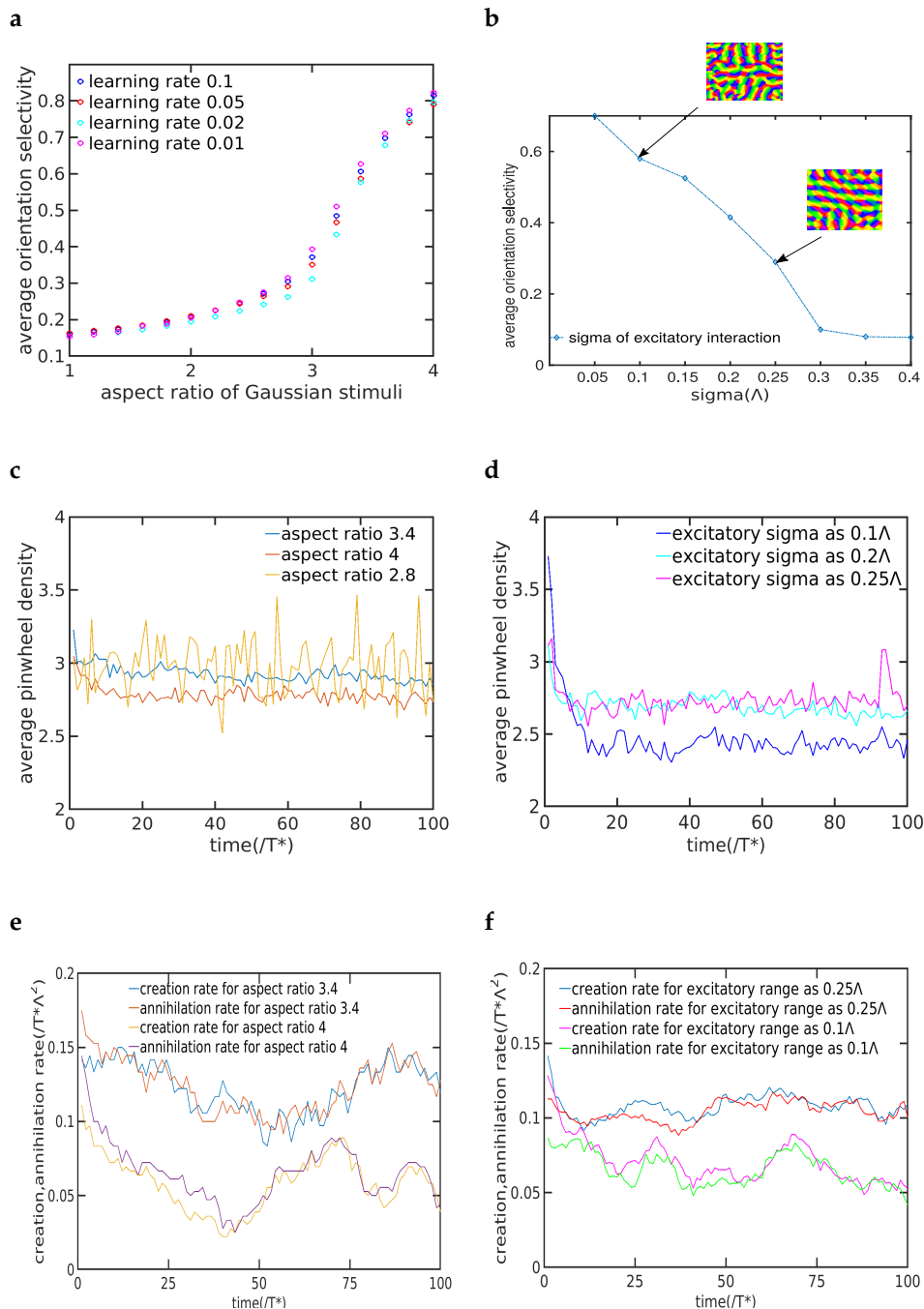


Figure (4.5) A bifurcation change for the average orientation selectivity increasing as the aspect ratio of Gaussian stimuli increases (a). The learning rates 0.1,0.05,0.02,0.01 are used for comparison. Another phase transition of orientation selectivity for changing the cortical excitatory range (b). The maps for one point near the critical value and another point far from the critical value are shown for differences. The average pinwheel densities of maps for using aspect ratio 2.8,3.4 and 4 (c). The average pinwheel densities of maps for different excitatory ranges (d). Creation rate and annihilation rate of pinwheels for using aspect ratios of stimuli as 3.4 and 4 (e). Creation rate and annihilation rate of pinwheels for using excitatory ranges as 0.25Λ and 0.1Λ (f).

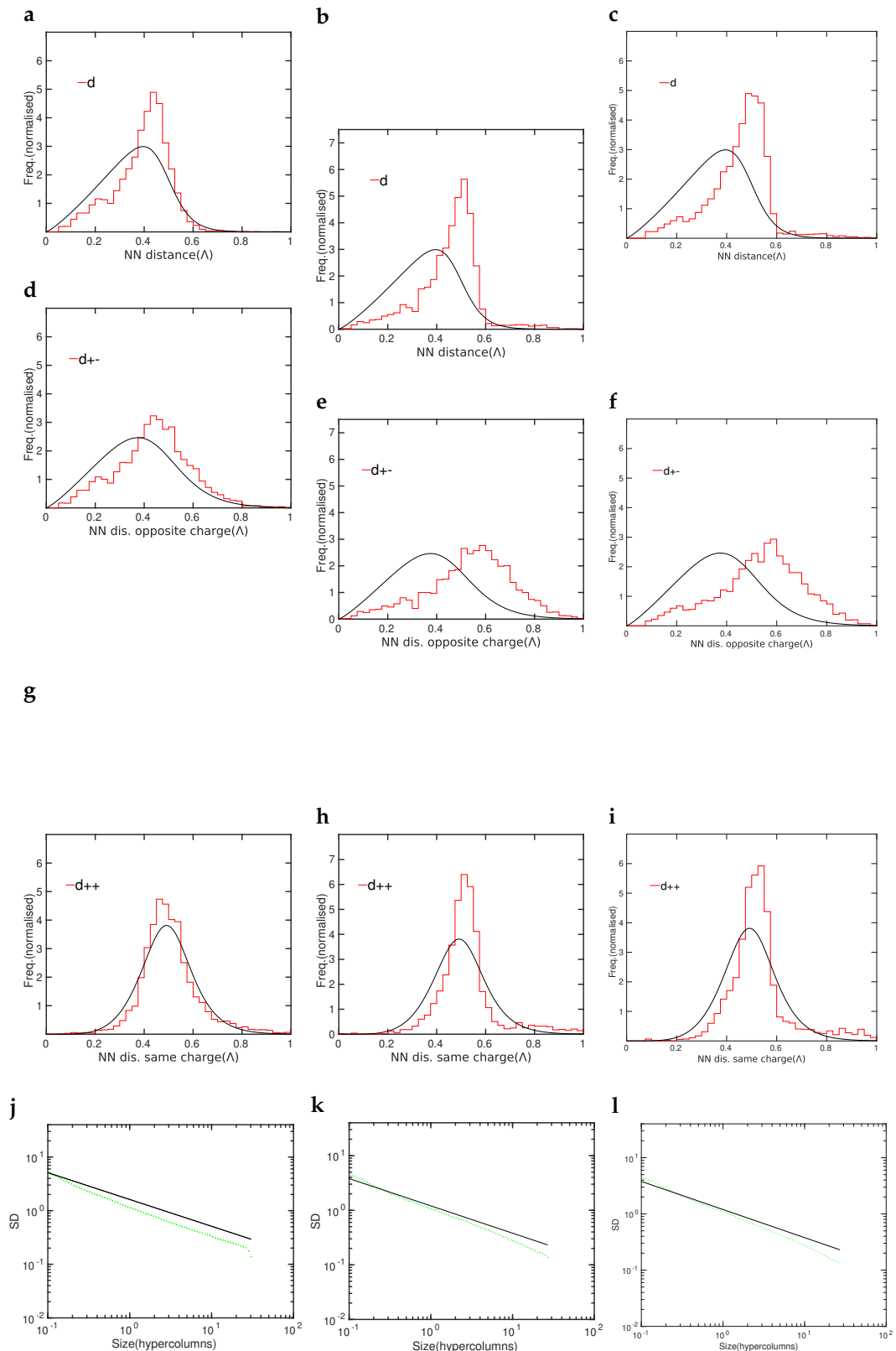


Figure (4.6) Nearest neighbor distances of pinwheels generated by the model without considering the topological charges at time $t=1T^*$, $100T^*$ and $300T^*$ (a)(b)(c). The black curves are the fitting functions for the common design. Nearest neighbor distances of pinwheels generated by the model with the same and the opposite topological charge at time $t=1T^*$, $100T^*$ and $300T^*$ (d)(e)(f). The black curves are the fitting functions for the common design. The standard deviation of the pinwheel density estimated in randomly selected circular regions of the size when time is $300T^*$ respectively (g)(h)(i). The black curves are standard

Figure 4.7 summarizes all common design features determined for the model layouts as a function of time and compares them to the experimentally observed values in tree shrew, galago, ferret, dark-reared ferrets, and cats. Light (dark)grey shaded areas indicate the single species(common design) consistency ranges. Over time the pinwheel density of model layouts decreases from 3.1 and then remains below the single species consistency range. Thus, the pinwheel density of model orientation domain layouts is inconsistent with pinwheel densities observed in all species. Next, we fitted the empirically observe power law, to the standard deviation of the pinwheel density estimate in randomly selected circular regions of size A . The variability exponent γ basically stayed above the experimentally observe regions and the confidential interval band has some overlap with the experimental observation area, while the confidential interval of variability constant c dropped below the experimental observe range. The Figure also displays the mean pinwheel NN distances as function of time, all of which increases during the first 10 time scales and then basically keep a stable level. Only the mean pinwheel NN distances for equal charge at some time points locate close to the border of experimental observe region and the confidential interval band intersects with the region. The other two types of mean NN distances are not consistent with the experimentally observed values.

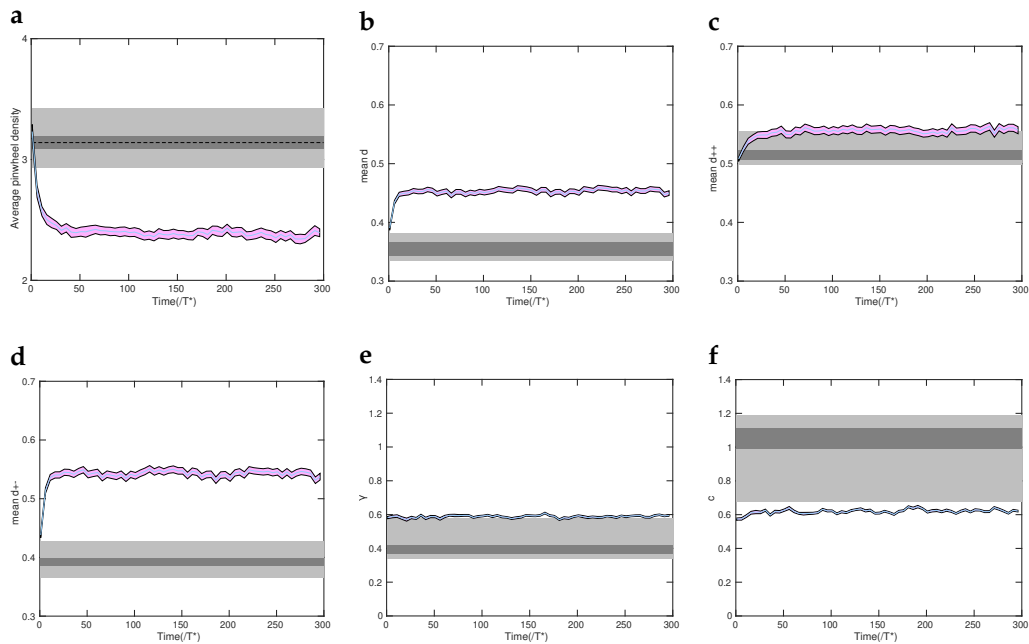


Figure (4.7) Pinwheel statistics of maps generated by Topographica model fail to match the common design. Grey shaded areas indicate the range consistent with the experiments. Grey areas show the values of the common design. The average pinwheel density of maps during the time course (a). Confidential interval are shown for 90 maps. Blue curves indicate the mean value. Mean nearest neighbor distances of pinwheels compared with the common design without considering topological charges, with the same topological charge and with the opposite topological charges, respectively (b)(c)(d). The variability exponent as a function of time compared to the common design (e). The variability constant in comparison with the common design (f).

4.4 Discussion

In this study, we examined if and how a input-driven model generates constant or changing orientation maps as representations of cortical functional architecture over time scales representative of biological critical periods. Firstly, we determined the time scales for simulations which correspond to the initial emergence of selectivity and to subsequent modifications. Then we analyzed orientation preference changes of single neurons and confirmed the layout of orientation maps exhibits rearrangement after orientation selectivity saturates. To quantify the speed of the primary visual cortex remodelling, we calculated pinwheel annihilation and generation rates, which turned out to be small but non zero. We closely examined one important statistics of pinwheel layout – pinwheel density and found that it rapidly drops to values below 3 over time after saturation of selectivity. Besides, we found there are two types of phase transitions in this model’s parameter space. One is the transition towards orientation selectivity for changing the aspect ratios of Gaussian stimuli.

Another one is the phase transition to orientation selectivity when changing the cortical excitatory range. In summary, we conclude there was no parameter regime in which the common design parameters matched experimental observations.

1. The boundary effect

Orientation maps in the simulations typically become more regular over time. The banded geometry of the orientation domains at the boundaries of V1 (with open boundary condition) increasingly dominate the center of the simulation area. This process is driven by pinwheel generation and annihilation events. The time scale of pinwheel survival is roughly maintained over the course of the simulation, with fluctuations depending on the learning rate of the system. The switching behavior between the prominence of orientation stripes from the lateral and from the superior/inferior boundaries prevents the pinwheel density to decrease to crystal-like values, concealing a potential ground state of the system. This indicates that boundary effects strongly influence the layouts in this model. But in biological reality, there is evidence showing that near the border of v1 and v2, orientation stripy domains are in fact present and perpendicular to the area border. In order to remove the boundary effect in this model, one can also consider implementing periodic boundary condition to this model.

2. The time scales

Experimental evidence clearly supports that cortical circuits remain in plastic state for weeks and months after the initial emergence of sensory responsiveness and stimulus selectivity. To know how far the rearrangement of cortical circuitry can reach a final state one has to relate the duration of the period of juvenile plasticity to the fundamental timescale of the map dynamics. This time scale is the duration of the process of establishing mature levels of the selectivity and in our model is the time T^* . From a theoretical perspective this time scale depends on the ensemble of activity patterns and on the details of the local cortical circuits which are not completely known.

L.Reichl et al. (2012) obtained empirical estimates for the relative duration of juvenile plasticity by comparing the characteristic time scale of initial map emergence and the duration of the period from map emergence to the closure of critical periods of visual cortical plasticity. A lower bound to the relative duration of juvenile plasticity is $10T^*$ according to experiments in cat and ferret visual cortex. In both species, data indicate at most one week to reach mature levels of single neuron's orientation selectivity, so the estimate for the time scale of orientation map development is that T^* is about one week. Since the period of susceptibility to monocular deprivation in kitten lasts between 12 to 16 weeks after single neurons first reach adult like levels of orientation selectivity and eye dominance, a lower bound for the relative duration of juvenile plasticity is thus $10T^*$. The longest estimate for a critical period in cat visual cortex was 33 weeks and assuming the time scale in the lower range of experimentally reported peak time scales i.e. 3 hours, one can estimate an absolute upper bound for the relative duration of the period of juvenile plasticity in cat is $1850 T^*$.

3. Comparison to previous studies

The Topographica model integrates a few simple and biologically realistic mechanisms to reproduce the map development. Specifically, contrast-gain control in the retinal ganglion cells and the lateral geniculate nucleus reduces variation in the presynaptic drive due to differences in input patterns, while homeostatic plasticity of V1 neuron excitability reduces the postsynaptic variability in firing rates.

The elastic net model, for comparison lacks these biological mechanisms and doesn't simulate responses to individual input patterns such as Gaussian or retinal waves. Unlike correlation-based learning models that use Hebbian learning over

large batches of inputs, Topographica model operate using incremental Hebbian learning rules. Although it is often more difficult to obtain mathematical results of the final model than those of linear, feedforward networks, the incremental properties of self-organizing maps make them more suitable for studying map development. Incremental learning allows gradual changes in network organization to be tracked as a stream of inputs drive the development of the network forward.

Lateral interactions are a key element in this model. The biological basis for V1 cortical interactions is the long-range horizontal connections between V1 neurons of layer 2/3. In this model the lateral interactions are mexican-hat type, short-range excitatory interaction and longer-range inhibitory interaction. However, this model doesn't include the long-range interaction part which means the cortical interaction range beyond 1 hypercolumn, if compared to the Wolf's model. Since Wolf's model predicts all the common design features shown in experimental observation, we think in the future work this model need to integrate the long-range interaction element, so that it may could solve the problem of predicting the experimental observed map layouts.

Chapter 5

Map dynamics near the critical point

5.1 Introduction

As demonstrated in Chapter 4, the Topographica model has a critical point for map formation at an aspect ratio of stimuli at about 3.4. Also there is another bifurcation parameter controlling the development of orientation selectivity is the excitatory range of cortical interactions. Here the critical point is located at about 0.08. In the following we ask, how is the circuit dynamics affected when the aspect ratio of stimuli or excitatory range are near or far from these critical points. In addition, we examine the circuit rearrangement in cortical model areas of increased sizes to assess the influence of boundary effects on circuit dynamics. In previous studies we chose area sizes between $1 * 1$ or $1.5 * 1.5$. Now we set the size of the cortical area as $3 * 3$.

5.2 Map development near the critical point

Firstly we do a time calibration for map development. From the plot one can see it is about 40000 steps as 1 time scale, T. See Figure 5.1.

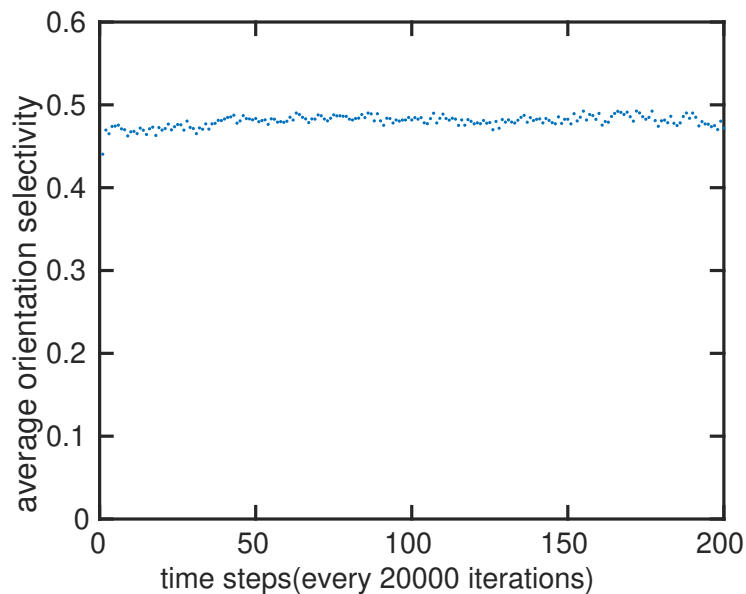


Figure (5.1) The development of orientation selectivity. Every dot is for the orientation selectivity value of every 20000 time steps. We can see at about 40000 time steps the selectivity reaches close to saturation state, therefore we choose 40000 time steps as 1 time scale.

By observation the maps at the beginning look somewhat noisy and stripy, but lately from about $10T$ they become closer to the shapes of maps generated by Wolf's model (M.Kaschube et al., 2010a). However the appearance of the maps at very late stage are filled with noisy crystals. We do Fourier transform of the map data and find in the initial stages there are multiple different Fourier modes saturating the ring but to the very later stages, e.g. $t = 100T$, about four main modes dominate the map distribution, which gives crystal-like shapes of the patterns. See Figure 5.2. Then we do statistical analysis for the maps. As shown in Figure 5.3, during the time evolution process the average pinwheel density of the maps goes above 4 and stays around 4.5, which deviate from the common design range. Interestingly, the mean pinwheel density does not fall below 3, as shown previously for the patterns. The confidential interval is outside of the experimental observation region. Also we plot the nearest neighbor distance distributions of pinwheel centers for $t = 100T$. The NN distance distribution for the data doesn't fit into the curves of the fitting functions. As seen from the figures, the mean NN distances for the same charge, the opposite charge, and arbitrary charge of pinwheels stays outside of the experimental observation scope. Also the confidential intervals don't locate at inside of the scope. Then we plot the standard deviation of the pinwheel density estimate in randomly selected circular regions and compare it to the empirically observed power law. They look like close to each other. The variability exponent r including its' confidential interval basically stay in the experimental observation regions while the variability constant c with the confidential interval also lies in the experimental observe scopes. We want to know why the patterns become noisy crystals in the late state. Is it because the excitatory range is near to the critical value? To answer this question we compare different maps with different excitatory ranges in controlled conditions and find that the Fourier modes for maps generated with the excitatory range 0.04, 0.05, 0.06, 0.07 and 0.08 are not a few and more than 4 main modes. Therefore the value 0.07 of the excitatory range for the maps in the "critical" state is not the only reason for becoming the late shapes. We suppose that it should combine the aspect ratios of the stimuli to analyze the maps further.

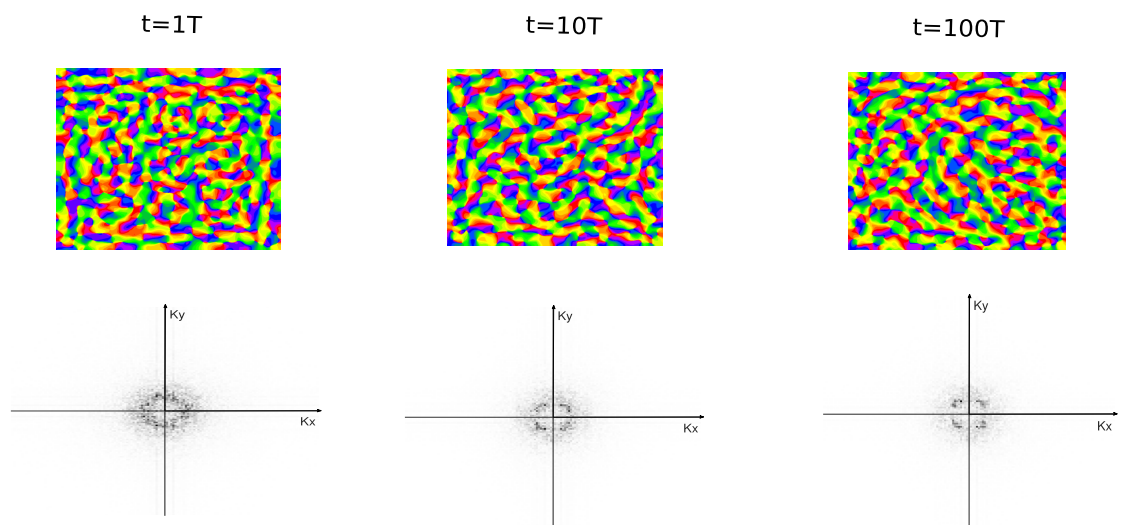


Figure (5.2) An example of map development near the critical point and their power spectrum by Fourier analysis.

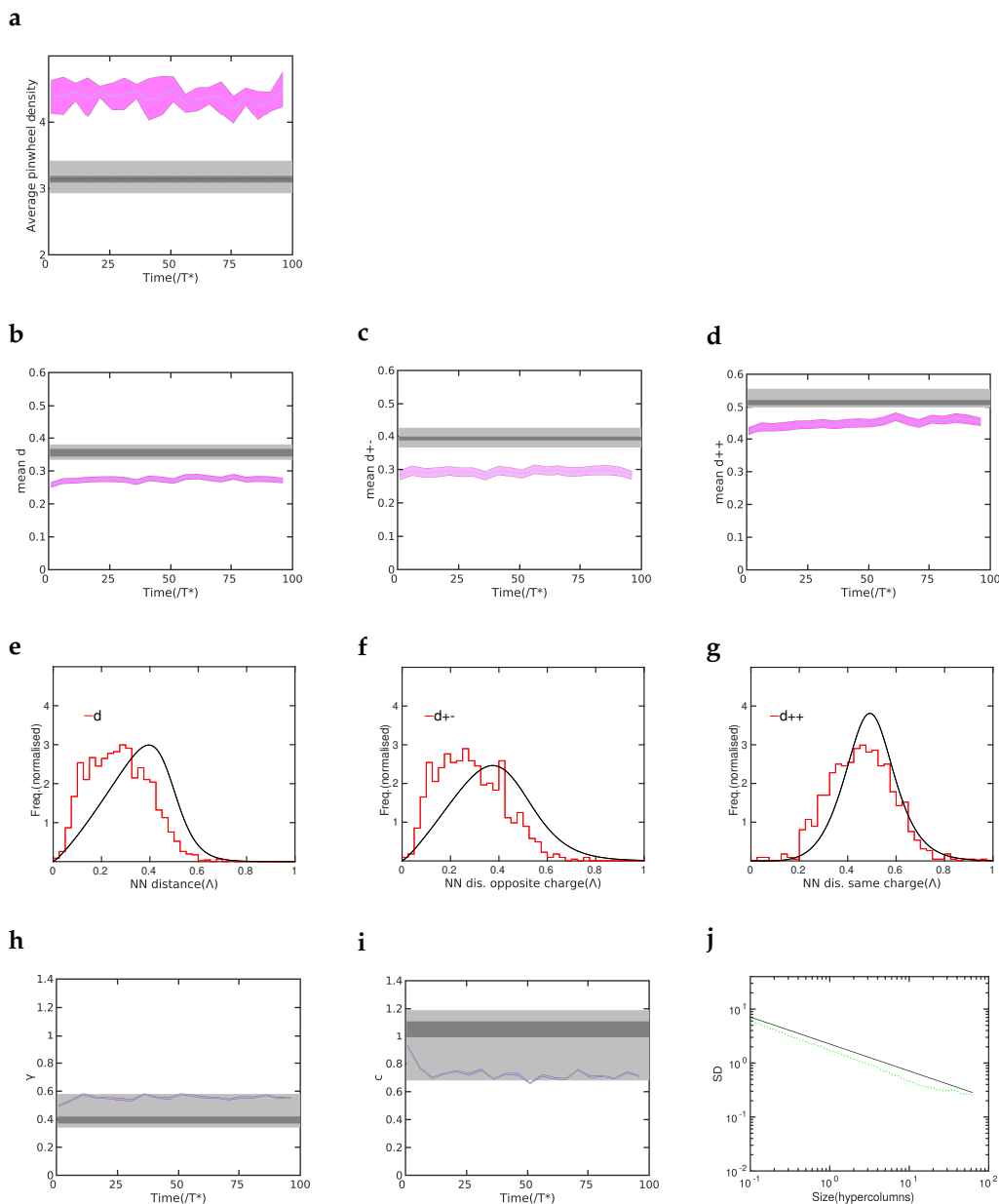


Figure (5.3) Pinwheel statistics for maps near the critical point. The time of statistics (e)(f)(g)(j) is $t = 100T$.

5.3 Impact of the parameter "excitatory range"

As the parameter "excitatory range" of the cortical interaction is important for map formation, we perform statistical analysis for different values of this parameter, including ones close to and far from the critical value. Firstly, we analyze the pinwheel density of maps for different values of excitatory ranges. We find all the mean pinwheel densities of maps for the values will drop to below 3 (Figure 5.4). We will show other statistics of maps one by one for different values of "excitatory range".

In the case of the excitatory range as 0.03, the average pinwheel density with the confidence interval drops to below 3 after a few time scales. The nearest neighbor(NN) distance distributions as function of time are plotted. In the beginning the mean NN distances with arbitrary and the opposite charge locate in the experiment consistency range but later they leave this range and basically stay outside of the range. The confidence interval of the mean NN distances with arbitrary charge of pinwheels has a small part of intersection with the experimental observation area. And the confidence interval of the mean NN distance with the opposite charge of pinwheels basically stays outside of the area. The mean NN distance with the same charge enters the experiment consistency range from the outside. Also the confidence interval of the mean NN distance with the same charge of pinwheels mainly overlaps the experimental consistence range. We show the NN distance distribution for $t=150T$. The distributions are close to the fitting functions but not fit. In addition,we fit the empirical observation power law, to the standard deviation of pinwheel density estimate in randomly selected circular regions. The confidence intervals of variability exponent r and the variability constant c basically stay in the experiment consistency range. We plot the case of $t=150T$ for the standard deviation of pinwheel densities as a function of the area of randomly selected subregions of the iso-orientation domain layout. The black line indicates the standard deviation for 2 dimensional Poisson process of pinwheel density π . The pinwheel density variability is close to the standard deviation of a 2 dimensional Poisson process of pinwheel density π but not completely fit. See Figure 5.4.

For the case of the value of the excitatory range equal to 0.04, the average pinwheel density with the confidence interval basically drops to below 3 after a few time scales. The NN distance distributions are analyzed. The mean NN distances with confidence intervals for the pinwheels with the opposite charge and arbitrary charge after a few time scales locate outside of the experiment consistency range, but the mean NN distance for the pinwheels with the same charge stays in the experiment consistency range. The confidence interval largely overlaps the range. We plot the NN distance distributions for $t=150T$. The distributions deviate from the fitting functions. Besides,we fit the empirical observation power law,to the standard deviation of pinwheel density estimate in randomly selected circular regions. The variability exponent r with the confidence interval is close to the border of the experiment consistency area while the variability constant c with the confidence interval basically stays outside of this range. We show the standard deviation of pinwheel densities as a function of the area of randomly selected subregions of the iso-orientation domain layout for $t=150T$. The pinwheel density variability deviate from the standard deviation of a 2 dimensional Poisson process of pinwheel density π . See Figure 5.5.

When the value of the excitatory range is 0.045, the average pinwheel density with the confidence interval drops to below 3 after a few time scales.The NN distance distributions are plotted. After a few time scales from the beginning, the mean NN distances for the pinwheels with the opposite charge and arbitrary charge lie in the outside of the experiment consistency range, while the mean NN distance for the pinwheels with the same charge stays in the experiment consistency range. The confidential intervals have similar trends with the mean NN distance values. The NN distance distributions for $t=150T$ is plotted. These distributions deviate from the fitting curves. In addition,we fit the empirical observation power law,to the standard deviation of pinwheel density estimate in randomly selected circular regions. Both of the variability exponent r and the variability constant c with the confidence intervals are close to the boundary of experiment consistency range but c is basically in

the outside of the range. The standard deviation of pinwheel densities as a function of the area of randomly selected subregions of the iso-orientation domain layout for $t=150T$ is shown. The pinwheel density variability doesn't fit the standard deviation of a 2 dimensional Poisson process of pinwheel density π . See Figure 5.6.

For the value of the excitatory range as 0.055, the average pinwheel density with the confidence interval basically drops to below 3 after a few time scales. Then we analyze the NN distance distributions. As similar with the above cases in this section, the mean NN distances with the confidence intervals for the pinwheels with the opposite charge and arbitrary charge stay in the outside of the experiment consistency range, while the mean NN distance for the pinwheels with the same charge basically lies in the experiment consistency range. The NN distance distributions for $t=150T$ are shown. These distributions deviate from the fitting functions. Besides, the empirical observation power law is fitted to the standard deviation of pinwheel density estimate in randomly selected circular regions. Both of the variability exponent r and the variability constant c with their confidence intervals basically are in the outside of the experiment consistency range. We plot the standard deviation of pinwheel densities as a function of the area of randomly selected subregions of the iso-orientation domain layout for $t=150T$. The pinwheel density variability deviate from the standard deviation of a 2 dimensional Poisson process of pinwheel density π . See Figure 5.7.

For the case of the excitatory range equal to 0.06, the mean pinwheel density with the confidence interval has a similar trend with above cases, which is that the values basically drop to below the experimental observation region. The NN distance distributions are analyzed. The mean NN distances of the pinwheels with the opposite charge and arbitrary charge of pinwheels lie in the outside of the experiment consistency range and the mean NN distance for the pinwheels with the same charge basically stays in the range. The confidence intervals for the mean NN distances of pinwheels are also shown. We plot the NN distance distributions for $t=150T$. These distributions deviate from the fitting curves. In addition, we fit the empirical observation power law, to the standard deviation of pinwheel density estimate in randomly selected circular regions. Both of the variability exponent r and the variability constant c with their confidence intervals basically stay in the outside of the experiment consistency range. For the case of $t=150T$ We plot the standard deviation of pinwheel densities as a function of the area of randomly selected subregions of the iso-orientation domain layout. The pinwheel density variability is not consistent with the standard deviation of a 2 dimensional Poisson process of pinwheel density π . See Figure 5.8.

For the value of the excitatory range as 0.065, we do the analysis of average pinwheel densities and the NN distance distributions. The mean pinwheel density drops to below the experiment values and the confidence interval has a small part intersecting with the experiment observation area. The mean NN distances of the pinwheels with the opposite charge and arbitrary charge and their confidence intervals stay outside of the experiment consistency range and the mean NN distance for the pinwheels with the same charge lies in the experiment consistency range. The NN distance distributions for $t=150T$ are shown in the Figure 5.9. These distributions deviate from the fitting functions. Besides, we fit the empirical observation power law, to the standard deviation of pinwheel density estimate in randomly selected circular regions. Both of the variability exponent r and the variability constant c with their confidence intervals are not in the experiment consistency range. For the case of $t=150T$ We show the standard deviation of pinwheel densities as a function of the area of randomly selected subregions of the iso-orientation domain layout. The

pinwheel density variability does not fit the standard deviation of a 2 dimensional Poisson process of pinwheel density π . See Figure 5.9.

In the case of the excitatory range equal to 0.07, the mean pinwheel density drops to below 3 but the confidence interval has some small parts in the experiment observation area. The NN distance distributions are also analyzed. After a few time scales the confidence intervals including mean NN distances of the pinwheels with the arbitrary and the opposite charge stands in the outside of the experiment consistency range. A main part of the line of the mean NN distance for the pinwheels with the same charge and a main part of the confidence interval lies in the experiment consistency range. On $t=150T$ the NN distance distributions are plotted. These distributions are not fitted by the functions. In addition, the empirical observation power law is fitted, to the standard deviation of pinwheel density estimate in randomly selected circular regions. Basically both of the variability exponent r and the variability constant c with confidence intervals don't but only a few points for r locates at in the experiment consistency range. On $t=150T$ we plot the standard deviation of pinwheel densities as a function of the area of randomly selected subregions of the iso-orientation domain layout. The pinwheel density variability deviate from the standard deviation of a 2 dimensional Poisson process of pinwheel density π . See Figure 5.10.

When the excitatory range grows to 0.075, we firstly analyze the average pinwheel density. After a few time scales the mean pinwheel density goes to below 3 and the confidence interval has some parts overlap the experiment observation region. After a few time scales the confidence intervals including the mean NN distances of the pinwheels with the arbitrary and the opposite charge locate at the outside of the experiment consistency range while a large part of another confidence interval including the line of the mean NN distance for the pinwheels with the same charge lies in the experiment consistency range. For $t=150T$ the NN distance distributions are plotted. See Figure 5.11. These distributions deviate from the fitting functions. Besides, we fit the empirical observation power law, to the standard deviation of the pinwheel density estimate in randomly selected circular regions. Both of the variability exponent r and basically the variability constant c with their confidence intervals don't but except a few points locate at the border of the experiment consistency range. For $t=150T$ we plot the standard deviation of pinwheel densities as a function of the area of randomly selected subregions of the iso-orientation domain layout. The pinwheel density variability deviate from the standard deviation of a 2 dimensional Poisson process of pinwheel density π .

For the value of the excitatory range as 0.08, as the same step with the above cases, we firstly analyze the average pinwheel density. The mean pinwheel density basically drops to below 3. Its' confidence interval has a wide band and some parts of it overlap the experiment observation area. Contrary to the results of previous values of the excitatory range, the mean NN distances of the pinwheels with the arbitrary and the opposite charge locate at the inside of the experiment consistency range while a part of the line of the mean NN distance for the pinwheels with the same charge lies in the experiment consistency range. Also the confidence intervals of the 3 type of mean NN distances of pinwheels have main parts locating at the experiment observation regions. The NN distance distributions are shown in the Figure 5.12 for $t=150T$. These distributions are closer than previous plots in this section but still deviate from the fitting functions. Then we fit the empirical observation power law, to the standard deviation of the pinwheel density estimate in randomly selected circular regions. Both of the variability exponent r and the variability constant c with their confidence intervals locate at in the experiment consistency range

except for a few points. For $t=150T$ we plot the standard deviation of pinwheel densities as a function of the area of randomly selected subregions of the iso-orientation domain layout. The pinwheel density variability basically fits the standard deviation of a 2 dimensional Poisson process of pinwheel density π well. See Figure 5.12.

Now consider the value of the excitatory range as 0.085, we will have similar analysis steps with the value of the excitatory range as 0.08. The average pinwheel density basically drops to below 3 but at a short time section it intersects the experiment observation area. The corresponding confidence interval becomes wide and has certain parts locating at the experiment observation scope. The mean NN distances of the pinwheels with the arbitrary and the opposite charge stay on the inside of the experiment consistency range while a part of the line of the mean NN distance for the pinwheels with the same charge stay in outside of the experiment consistency range. Also the three type of confidence intervals almostly fill the experiment observation regions. We selectively plot the NN distance distributions when the time is $150T$. These distributions are close to the fitting functions. Then we fit the empirical observation power law, to the standard deviation of the pinwheel density estimate in randomly selected circular regions. Both of the variability exponent r and the variability constant c with the confidence intervals lie in the experiment consistency range except at a few points. Then we take the time $150T$ as an example to show the standard deviation of pinwheel densities as a function of the area of randomly selected subregions. The pinwheel density variability basically is close to the standard deviation of a 2 dimensional Poisson process of pinwheel density π . See Figure 5.13.

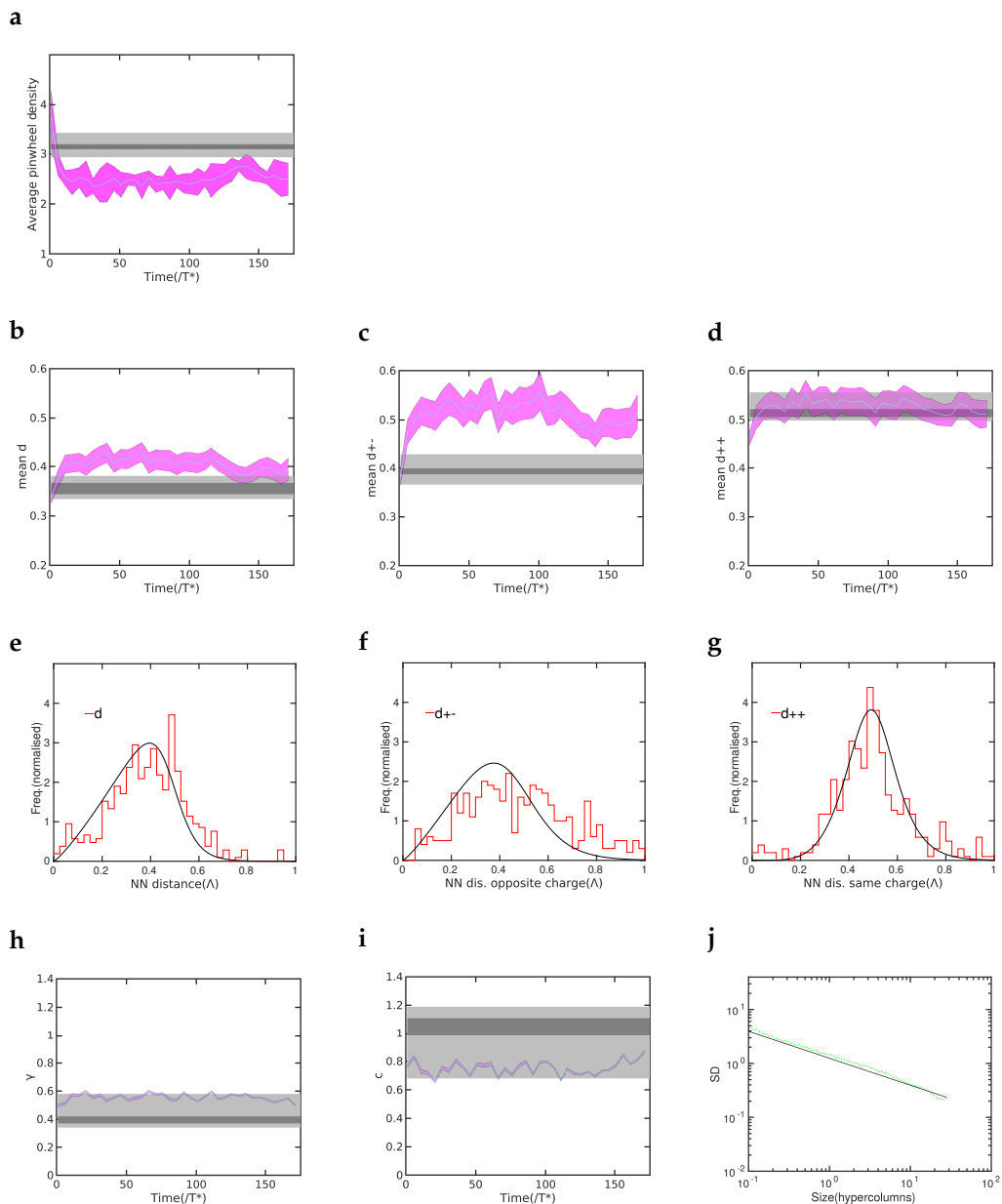


Figure (5.4) Pinwheel statistics for the excitatory range as 0.03. The mean pinwheel density of maps during the time course (a). The mean NN distance for arbitrary pinwheel charges (b). The mean NN distance for opposite pinwheel charges (c). The mean NN distance for same pinwheel charges (d). The NN distance distribution for arbitrary pinwheel charges when $t=150T$ (e). The NN distance distribution for opposite pinwheel charges when $t=150T$ (f). The NN distance distribution for same pinwheel charges when $t=150T$ (g). The variability exponent r (h). The variability constant c (i). The standard deviation of pinwheel densities as a function of the area of randomly selected subregions of the iso-orientation domain layout when the time is $150T$. The black line indicates the standard deviation for 2 dimensional Poisson process of pinwheel density π (j).

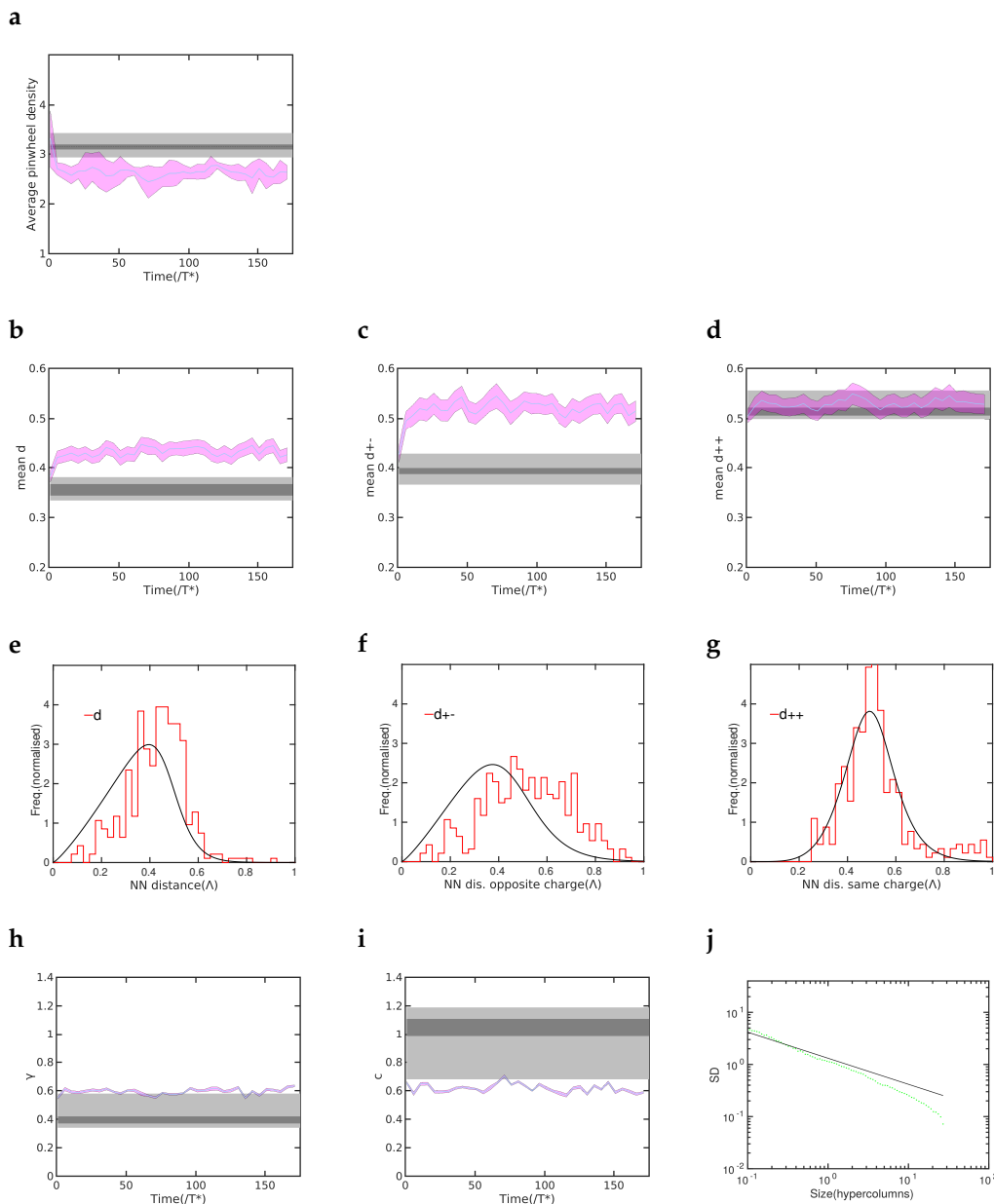


Figure (5.5) Pinwheel statistics for the excitatory range as 0.04. The mean pinwheel density of maps during the time course (a). The mean NN distance for arbitrary pinwheel charges (b). The mean NN distance for opposite pinwheel charges (c). The mean NN distance for same pinwheel charges (d). The NN distance distribution for arbitrary pinwheel charges when $t=150T$ (e). The NN distance distribution for opposite pinwheel charges when $t=150T$ (f). The NN distance distribution for same pinwheel charges when $t=150T$ (g). The variability exponent r (h). The variability constant c (i). The standard deviation of pinwheel densities as a function of the area of randomly selected subregions of the iso-orientation domain layout when the time is $150T$. The black line indicates the standard deviation for 2 dimensional Poisson process of pinwheel density π (j).

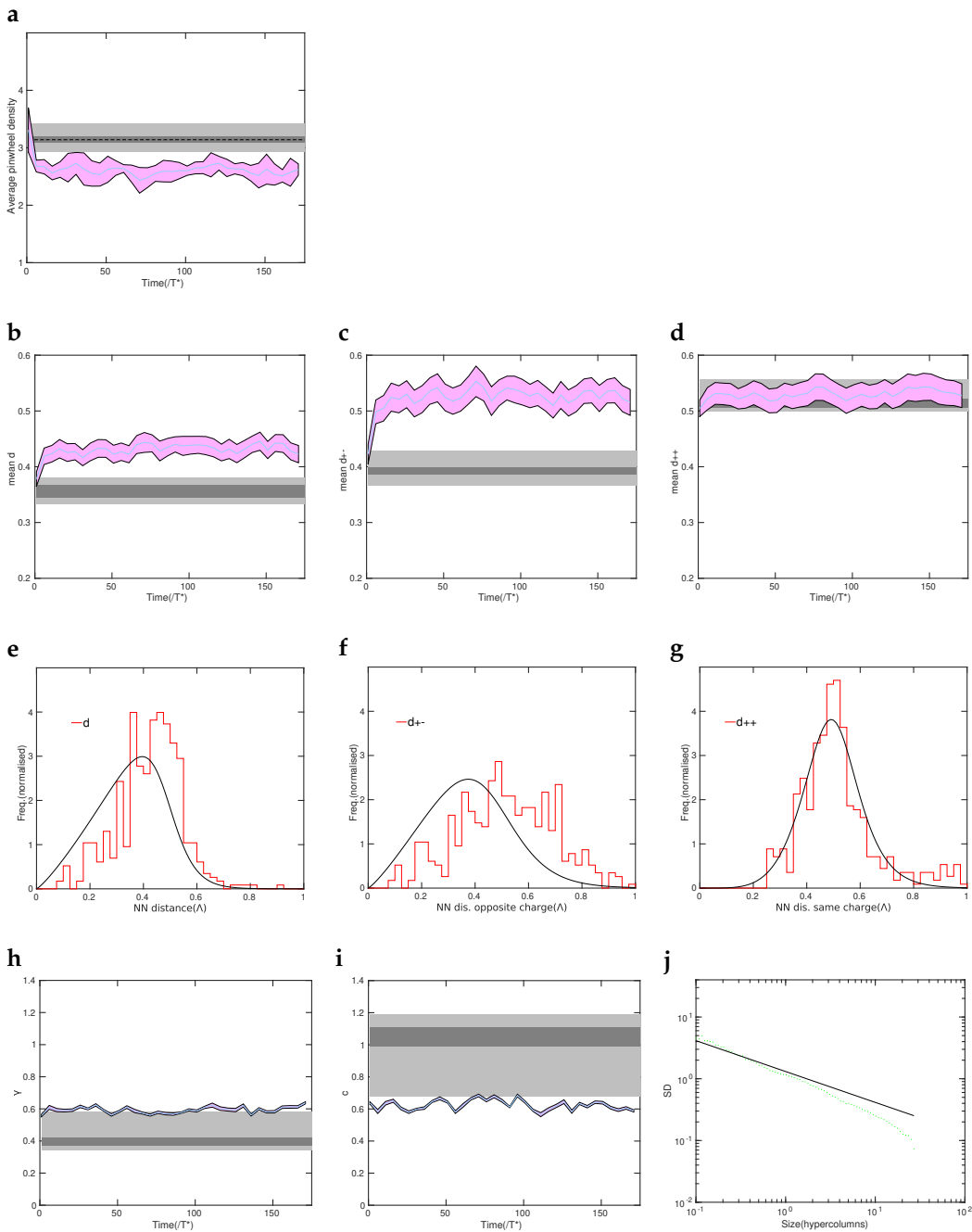


Figure (5.6) Pinwheel statistics for the excitatory range as 0.045. The mean pinwheel density of maps during the time course (a). The mean NN distance for arbitrary pinwheel charges (b). The mean NN distance for opposite pinwheel charges (c). The mean NN distance for same pinwheel charges (d). The NN distance distribution for arbitrary pinwheel charges when $t=150T$ (e). The NN distance distribution for opposite pinwheel charges when $t=150T$ (f). The NN distance distribution for same pinwheel charges when $t=150T$ (g). The variability exponent r (h). The variability constant c (i). The standard deviation of pinwheel densities as a function of the area of randomly selected subregions of the iso-orientation domain layout when the time is $150T$. The black line indicates the standard deviation for 2 dimensional Poisson process of pinwheel density π (j).

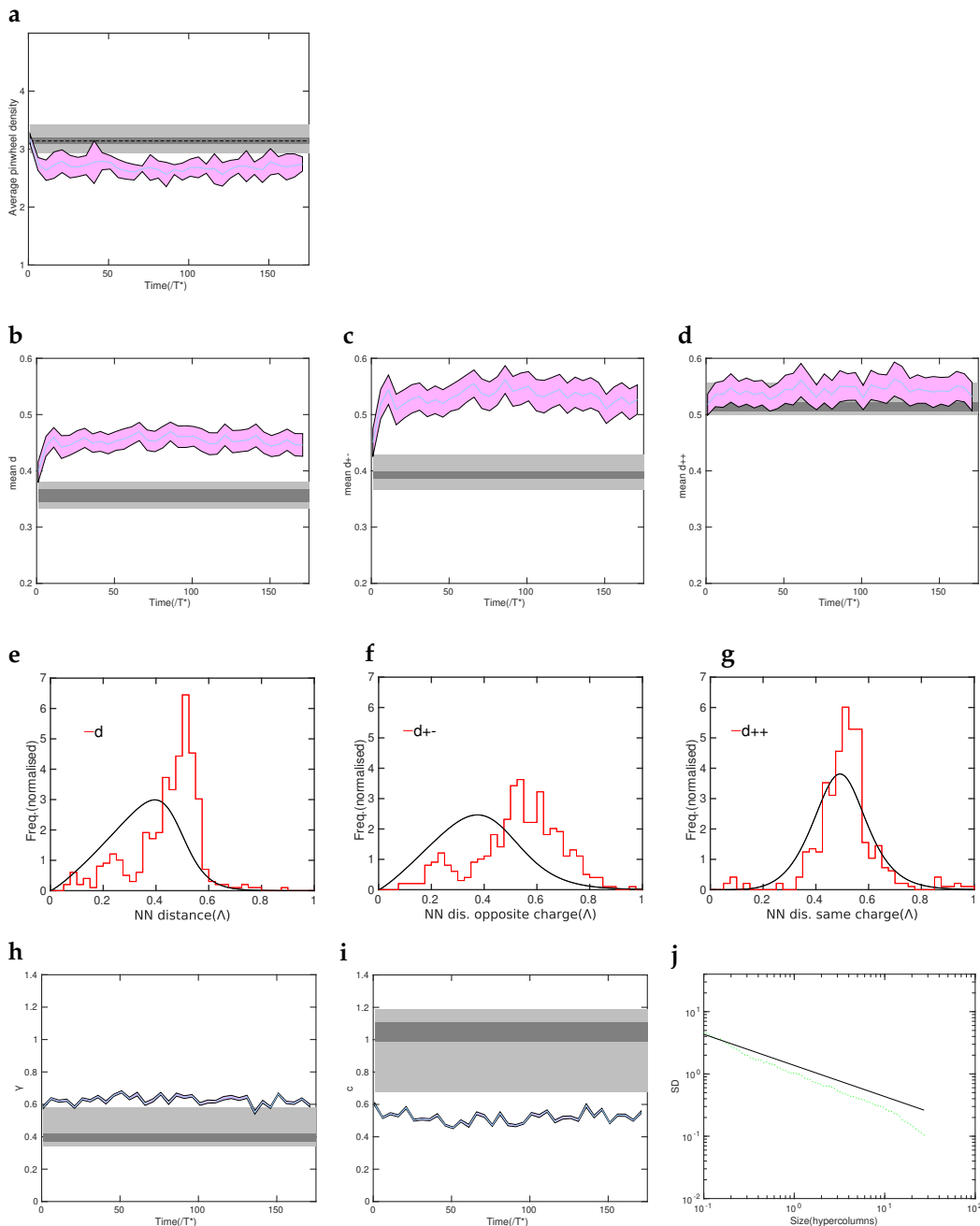


Figure (5.7) Pinwheel statistics for the excitatory range as 0.055. The mean pinwheel density of maps during the time course (a). The mean NN distance for arbitrary pinwheel charges (b). The mean NN distance for opposite pinwheel charges (c). The mean NN distance for same pinwheel charges (d). The NN distance distribution for arbitrary pinwheel charges when $t=150T$ (e). The NN distance distribution for opposite pinwheel charges when $t=150T$ (f). The NN distance distribution for same pinwheel charges when $t=150T$ (g). The variability exponent r (h). The variability constant c (i). The standard deviation of pinwheel densities as a function of the area of randomly selected subregions of the iso-orientation domain layout when the time is $150T$. The black line indicates the standard deviation for 2 dimensional Poisson process of pinwheel density π (j).

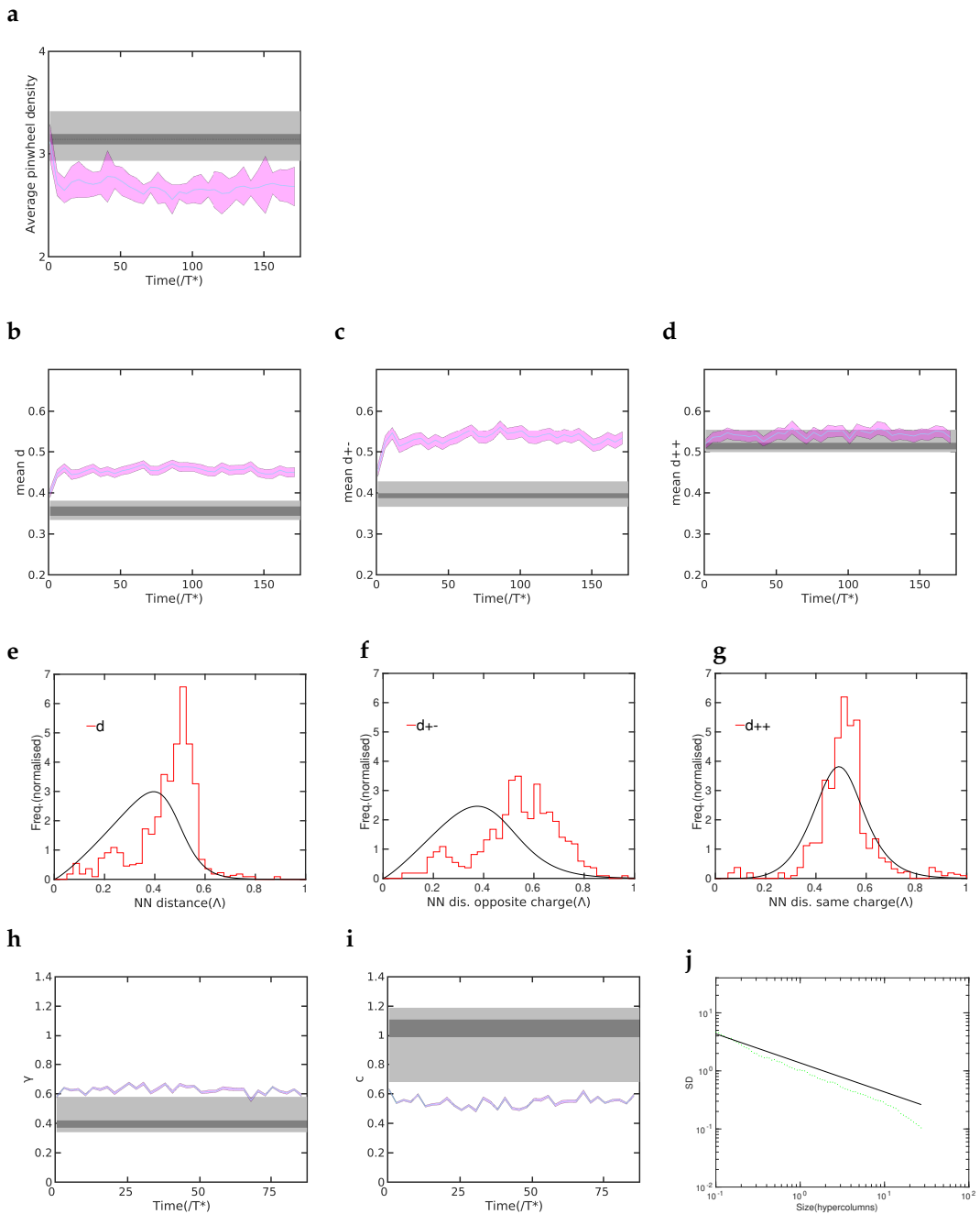


Figure (5.8) Pinwheel statistics for the excitatory range as 0.06. The mean pinwheel density of maps during the time course (a). The mean NN distance for arbitrary pinwheel charges (b). The mean NN distance for opposite pinwheel charges (c). The mean NN distance for same pinwheel charges (d). The NN distance distribution for arbitrary pinwheel charges when $t=150T$ (e). The NN distance distribution for opposite pinwheel charges when $t=150T$ (f). The NN distance distribution for same pinwheel charges when $t=150T$ (g). The variability exponent r (h). The variability constant c (i). The standard deviation of pinwheel densities as a function of the area of randomly selected subregions of the iso-orientation domain layout when the time is $150T$. The black line indicates the standard deviation for 2 dimensional Poisson process of pinwheel density π (j).

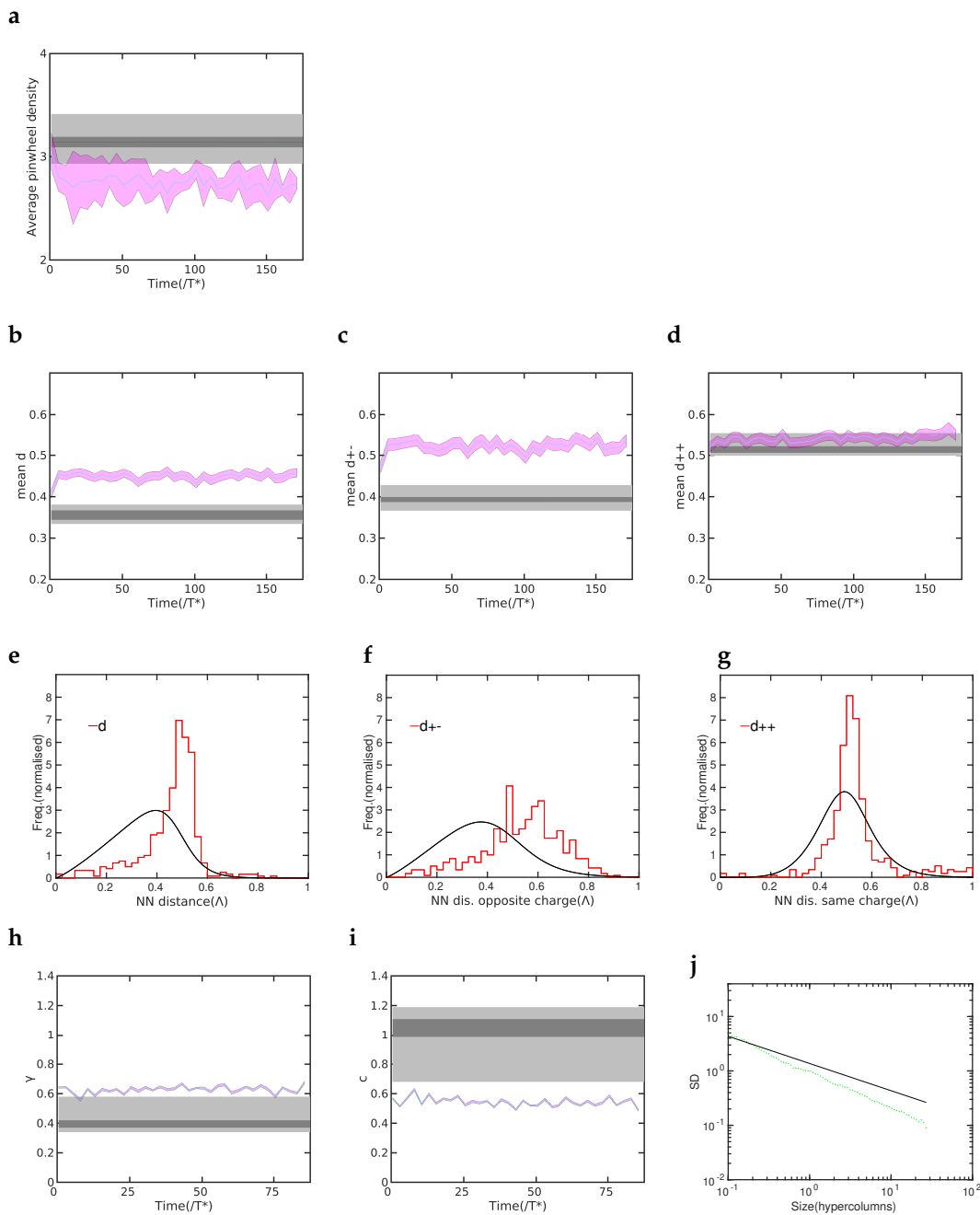


Figure (5.9) Pinwheel statistics for the excitatory range as 0.065. The mean pinwheel density of maps during the time course (a). The mean NN distance for arbitrary pinwheel charges (b). The mean NN distance for opposite pinwheel charges (c). The mean NN distance for same pinwheel charges (d). The NN distance distribution for arbitrary pinwheel charges when $t=150T$ (e). The NN distance distribution for opposite pinwheel charges when $t=150T$ (f). The NN distance distribution for same pinwheel charges when $t=150T$ (g). The variability exponent r (h). The variability constant c (i). The standard deviation of pinwheel densities as a function of the area of randomly selected subregions of the iso-orientation domain layout when the time is $150T$. The black line indicates the standard deviation for 2 dimensional Poisson process of pinwheel density π (j).

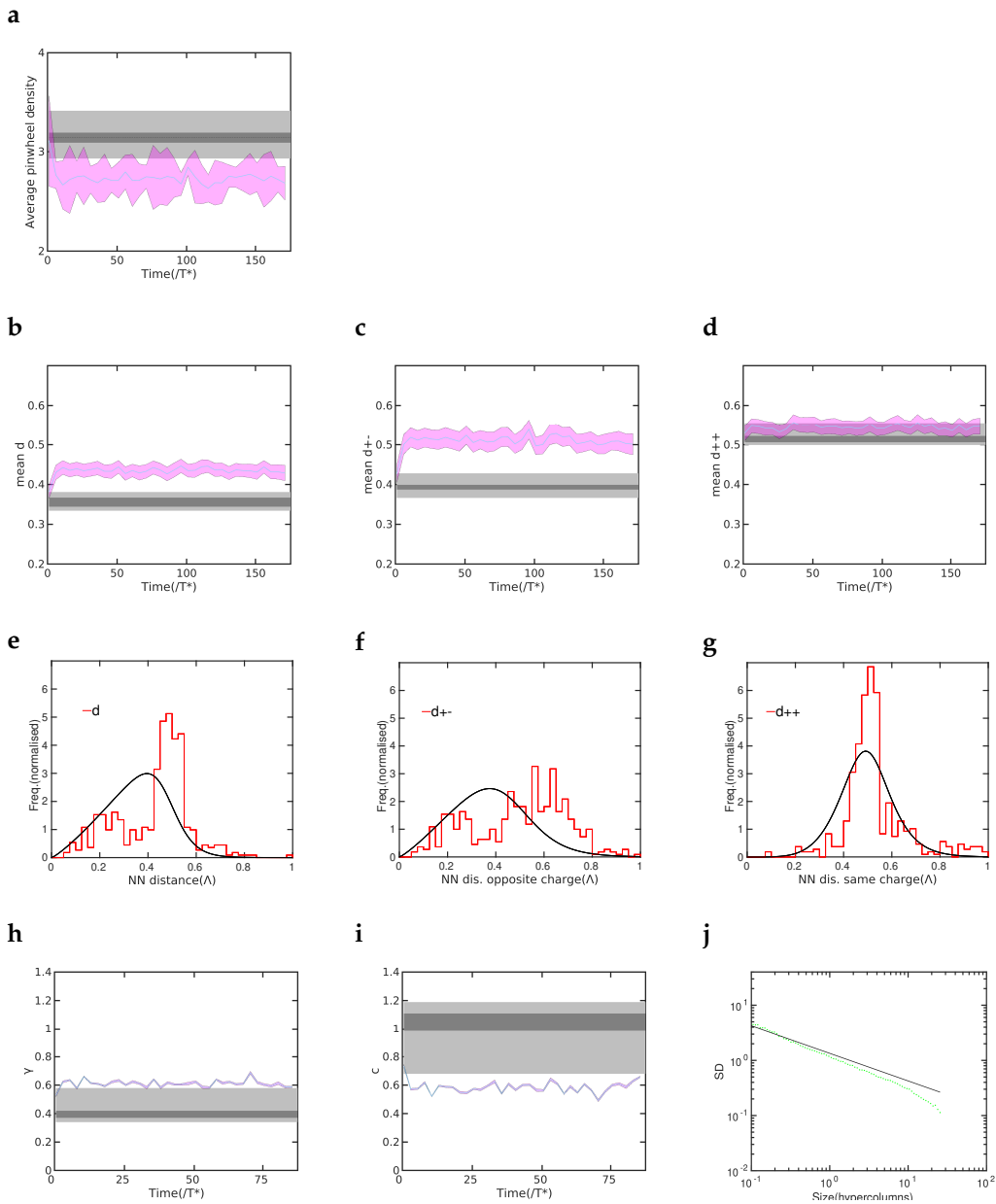


Figure (5.10) Pinwheel statistics for the excitatory range as 0.07. The mean pinwheel density of maps during the time course (a). The mean NN distance for arbitrary pinwheel charges (b). The mean NN distance for opposite pinwheel charges (c). The mean NN distance for same pinwheel charges (d). The NN distance distribution for arbitrary pinwheel charges when $t=150T$ (e). The NN distance distribution for opposite pinwheel charges when $t=150T$ (f). The NN distance distribution for same pinwheel charges when $t=150T$ (g). The variability exponent r (h). The variability constant c (i). The standard deviation of pinwheel densities as a function of the area of randomly selected subregions of the iso-orientation domain layout when the time is $150T$. The black line indicates the standard deviation for 2 dimensional Poisson process of pinwheel density π (j).

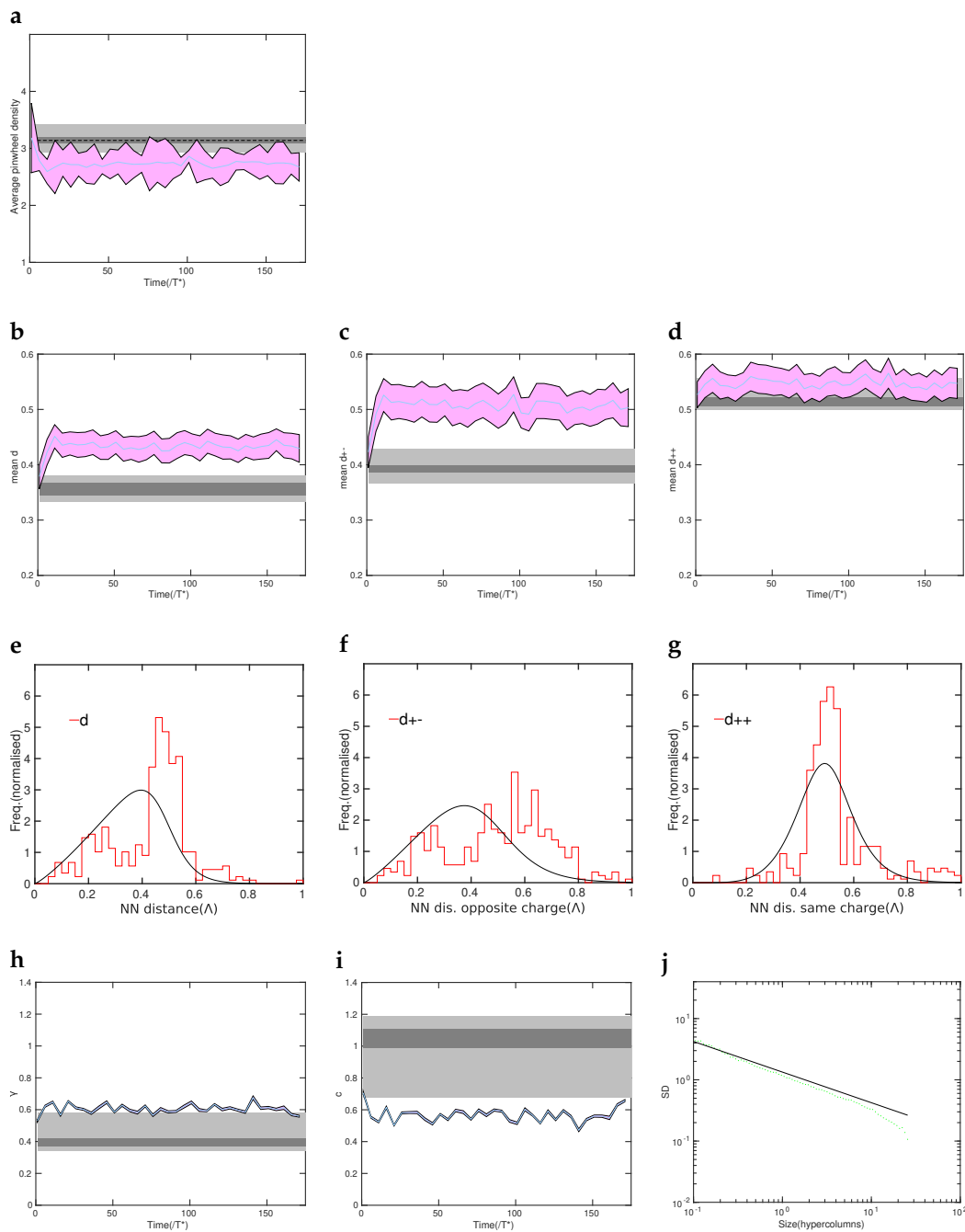


Figure (5.11) Pinwheel statistics for the excitatory range as 0.075. The mean pinwheel density of maps during the time course (a). The mean NN distance for arbitrary pinwheel charges (b). The mean NN distance for opposite pinwheel charges (c). The mean NN distance for same pinwheel charges (d). The NN distance distribution for arbitrary pinwheel charges when $t=150T$ (e). The NN distance distribution for opposite pinwheel charges when $t=150T$ (f). The NN distance distribution for same pinwheel charges when $t=150T$ (g). The variability exponent r (h). The variability constant c (i). The standard deviation of pinwheel densities as a function of the area of randomly selected subregions of the iso-orientation domain layout when the time is $150T$. The black line indicates the standard deviation for 2 dimensional Poisson process of pinwheel density π (j).

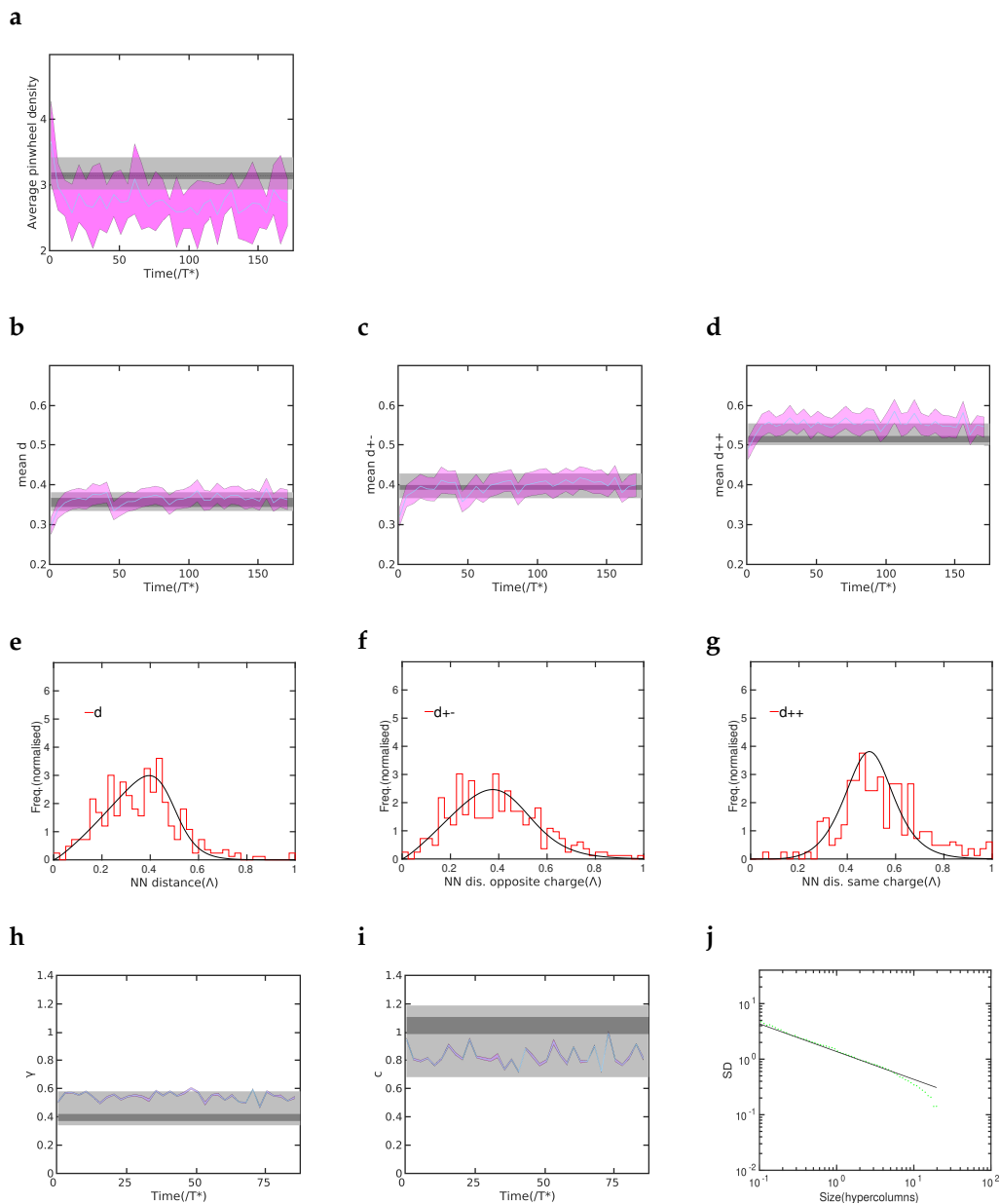


Figure (5.12) Pinwheel statistics for the excitatory range as 0.08. The mean pinwheel density of maps during the time course (a). The mean NN distance for arbitrary pinwheel charges (b). The mean NN distance for opposite pinwheel charges (c). The mean NN distance for same pinwheel charges (d). The NN distance distribution for arbitrary pinwheel charges when $t=150T$ (e). The NN distance distribution for opposite pinwheel charges when $t=150T$ (f). The NN distance distribution for same pinwheel charges when $t=150T$ (g). The variability exponent r (h). The variability constant c (i). The standard deviation of pinwheel densities as a function of the area of randomly selected subregions of the iso-orientation domain layout when the time is $150T$. The black line indicates the standard deviation for 2 dimensional Poisson process of pinwheel density π (j).

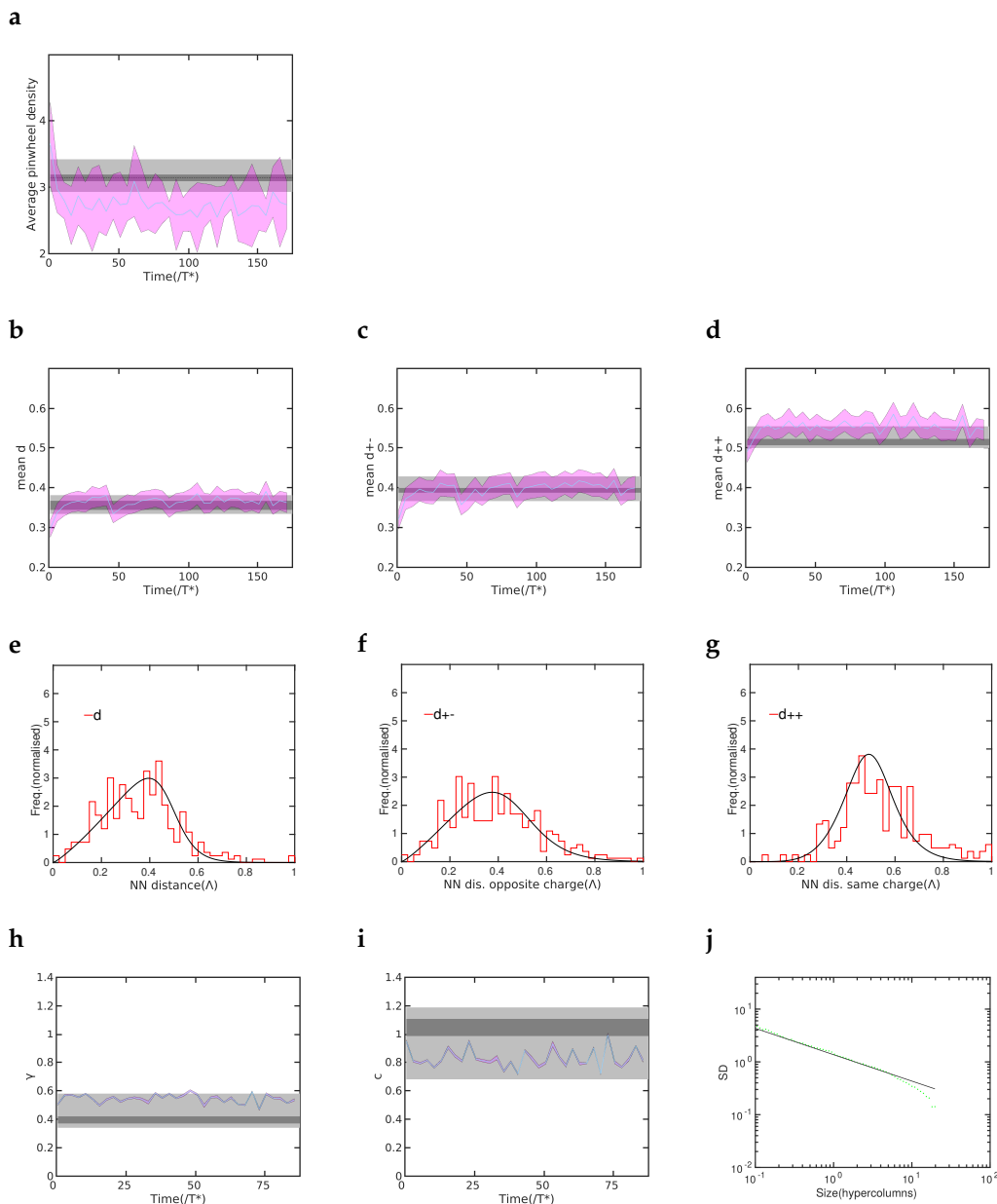


Figure (5.13) Pinwheel statistics for the excitatory range as 0.085. The mean pinwheel density of maps during the time course (a). The mean NN distance for arbitrary pinwheel charges (b). The mean NN distance for opposite pinwheel charges (c). The mean NN distance for same pinwheel charges (d). The NN distance distribution for arbitrary pinwheel charges when $t=150T$ (e). The NN distance distribution for opposite pinwheel charges when $t=150T$ (f). The NN distance distribution for same pinwheel charges when $t=150T$ (g). The variability exponent r (h). The variability constant c (i). The standard deviation of pinwheel densities as a function of the area of randomly selected subregions of the iso-orientation domain layout when the time is $150T$. The black line indicates the standard deviation for 2 dimensional Poisson process of pinwheel density π (j).

Chapter 6

Impact of periodic boundary conditions

6.1 Introduction

In order to remove boundary effects, we next introduced periodic boundary conditions into the model. Periodic boundaries mean the model from retina to cortical area are assumed to be wrapped around the boundaries and have the topology of a 2 torus. This biologically is a counterfactual assumption since both the represented part of the retina as well as the cortical area a finite size bounded 2D regions. However, boundary effects may very well represent real biological phenomena. Closely examining models with periodic boundaries therefore can provide two kinds of important biological insight. Firstly, by comparison with the finite open boundary behaviour clearly identify phenomena cause by boundary conditions in the model. Secondly, large regions models with periodic boundary conditions can be more representative of bulk behaviour far from area boundaries. Results from periodic boundary simulations therefore also reveal characteristic difference between "boundary layer" and "bulk behaviour".

6.2 Implementation of periodic boundary conditions

In order to remove the boundary effect for map formation, we use periodic boundary conditions for the model. Periodic boundaries mean the model from retina part to cortical part is wrapped by boundaries.

Firstly, the activity pattern inputs to the retina are periodically setted. We typically use Gaussian patterns as the retina inputs. For the patterns, the x coordinate part and the y coordinate part are rolled along the axes. The rolling range is between -75 and 75 if the retina area size is $1.5 * 1.5$ and the retina density is 100. We use the random number function to generate random shifts of the x coordinate parts and the y coordinate parts of the Gaussian patterns. Thus we can obtain random periodical Gaussian patterns.

Secondly, we modify the input sheet slices for generating connection fields. The creation of the input sheet slice provides the appropriate slice for the connection filed on the input sheet, as well as provides this connection field's exact bounds. Also the function of input sheet slices creates the weights slice, which offers the slice for the weights matrix. The weights matrix in nonperiodic cases must be cropped at an edge. We need to make the submatrix's bounds wrapped. The submatrix is equivalent to computing the intersection between the SheetCoordinateSystem's bounds and the bounds of the input slices, and returning the corresponding submatrix of the given matrix. As a single connection filed function which is applied to calculate

the inputs from retina to LGN or from LGN to V1, it is the submatrix of input slices multiplying the connection weights. By wrapping the bounds of the submatrix, we could obtain periodic input slices from one layer to the next layer in the model.

Besides, we need to have corresponding measurement methods for measuring the orientation selectivity of periodic maps. Instead of using sine waves to measure the selectivity, we take periodic Gaussian patterns for the measurement. By choosing size as 0.085 and aspect ratio as 5, we change the Gaussian patterns for various centers x and y positions, also for 4 different orientations. For retina area size as $1 * 1$, we use 50 positions for x axis direction and 50 positions for y axis direction. Thus for every measurement $4 * 50 * 50$ periodic Gaussian patterns are presented. We don't adopt sine waves as inputs for measurement is because near the edges a neuron in the periodic network will see bits of two different chunks of sine waves, which will by definition be a poor match to any single receptive field.

In addition, we make equal sizes of areas for retina, LGN ON or OFF sheet and V1 sheet, which is not the same as the previous Topographica model we use. In the original Topographica model, near the boarder of the retina there is a area where no input activity touches. But now we need to implement periodic inputs and the boundary of retina is wrapped, so we need to remove the "free" area near the boarder of the retina. Correspondingly, we also don't use other layers with extra free space near the boundaries. To be simplified, we adapt the same sizes of all sheets in this model.

6.3 Map development with periodic boundary conditions

We do simulations to observe the process of the map development with periodic boundary conditions. Take two maps as examples. For the first example maps, at the initial state of time $t = 0.1T$ (T is the time scale), the map looks stripy and is multiple orientation arranged. In later stage, e.g. $t = 20T$, the orientations of map stripes are reduced and the map become more lumpy. After this the map gradually become regular and crystallized. Another map has a similar process with this map. If we perform Fourier analysis we find for the maps of late stages, e.g. $t = 200T$, the Fourier power spectrums of them has only a few modes, mainly 4 modes. This indicate why they become crystallized. See Figure 6.1.

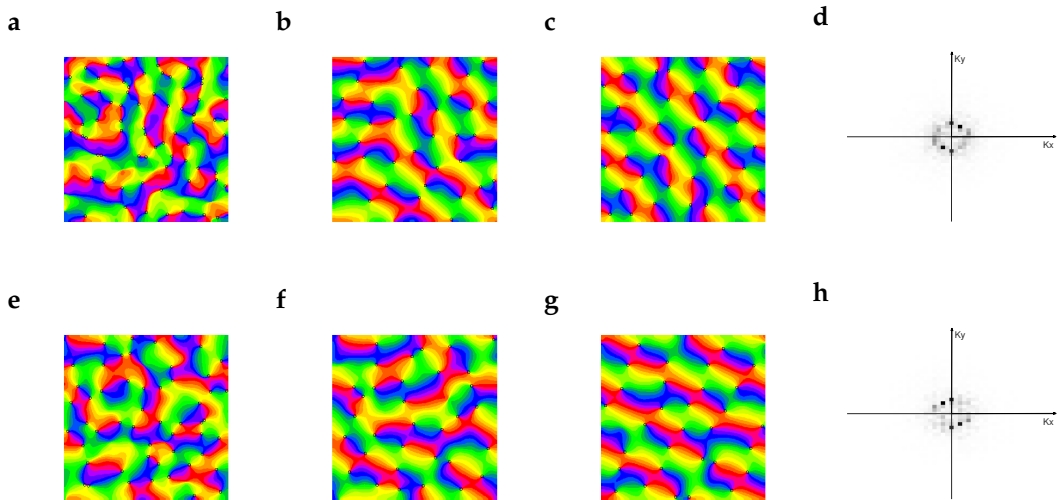


Figure (6.1) The example snapshots of map development process and Fourier modes. (a)-(c) is a process of one map development for $t = 0.1T, 20T$ and $200T$. (d) is Fourier modes of the map(c). (e)-(g) is for another map development for $t = 0.1T, 20T, 200T$. (h) is Fourier modes of the map(g).

Then we analyze pinwheel statistics of the maps during development. See Figure 6.2. For the average pinwheel density, at $t = 1T$ it locates the common design consistency range but lately it drops to below 3 and stays in between 2 and 2.5. The confidence interval decreases to below the experiment observation region. We also plot statistics for nearest neighbor distance distributions of pinwheel centers. At $t = 200T$ all of nearest neighbor distance distributions for pinwheels with the same charge, the opposite charge and the arbitrary charge deviate from the fitting functions. The mean NN distances as functions of time are shown. The mean NN distance without considering pinwheel charges keeps staying outside of experiment observation range. The confidence interval leaves the experiment observation range after a few time scales. The mean NN distance with the opposite pinwheel charges have a similar trend with it and also locates at the outside of the experimental observation range. The corresponding confidence interval starts from the experiment observation region and leaves the region lately. For the mean NN distance with the same pinwheel charge it crosses the common design consistency range and the confidence interval fills the experiment observation area. Besides, we fit the empirically observe power law, to the standard deviation of pinwheel density estimate in randomly selected circular regions of size A . The confidence intervals of the variability exponent r and the variability constant c are outside of experimental scopes. We evaluate the standard deviation of pinwheel densities as a function of the area A of randomly selected subregions of the iso-orientation domain layout. In the figure the black line is the standard deviation for 2 dimensional Poisson process of pinwheel density π . The pinwheel density variability deviates from standard deviation of a 2 dimensional Poisson process of pinwheel density π . We show for example the case of $t = 200T$.

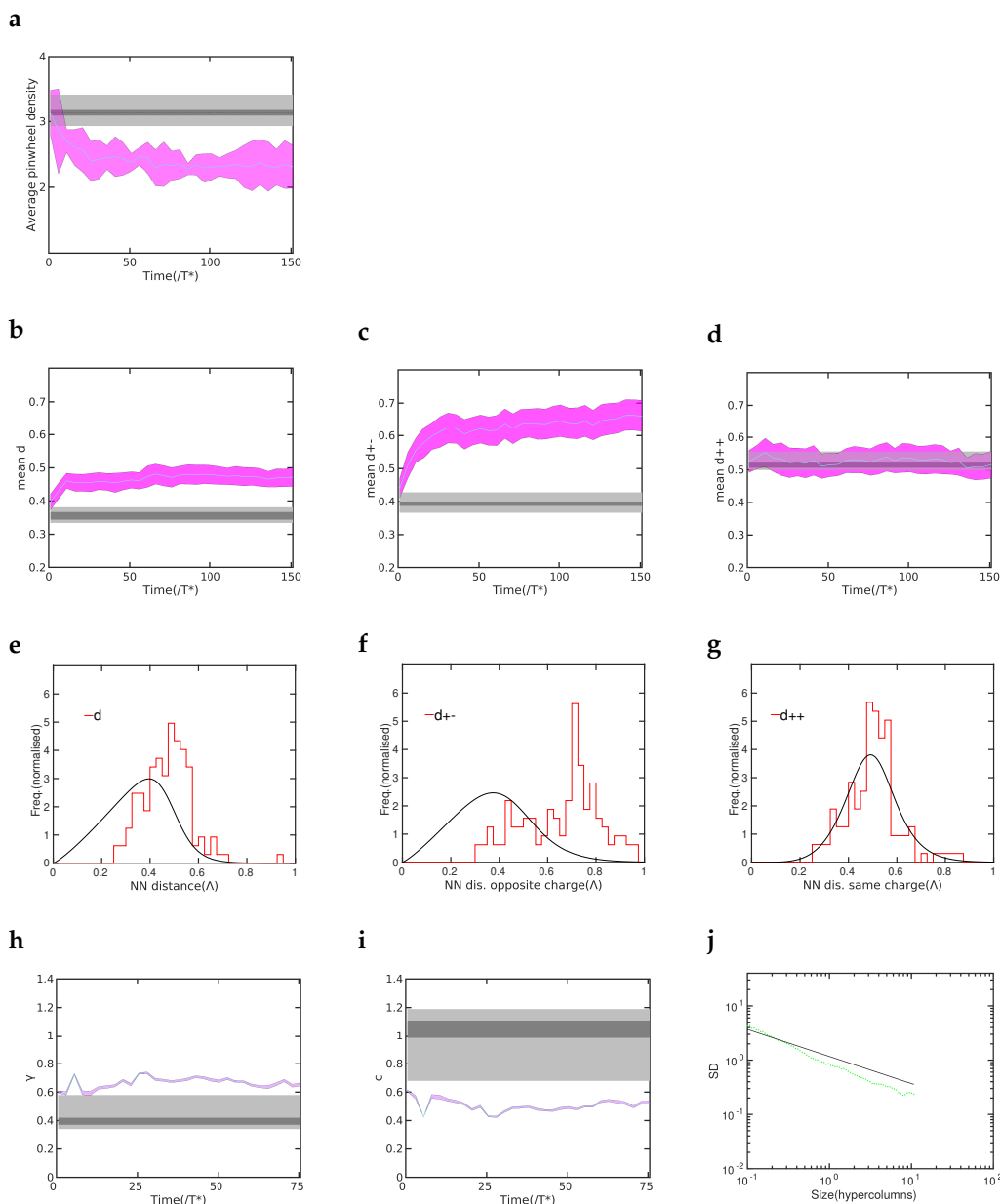


Figure (6.2) The statistics for map layouts during the time course. The average pinwheel density of maps (a). The variability exponent r (b). The variability constant c (c). For $t = 200T$ the NN distance distribution for arbitrary charges of pinwheels (d). For $t = 200T$ the NN distance distribution for opposite charges of pinwheels (e). For $t = 200T$ the NN distance distribution for same charges of pinwheels (f). The mean NN distance for arbitrary charges of pinwheels (g). The mean NN distance for same charges of pinwheels (i). The mean NN distance for opposite charges of pinwheels (h). The standard deviation of pinwheel densities as a function of the area of randomly selected subregions of the iso-orientation domain layout when the time is $200T$. The black line indicates the standard deviation for 2 dimensional poisson process of pinwheel density π (j).

Chapter 7

The impact of system size

7.1 Map structure for different system sizes

The observation of different maps for different area sizes is as follows. Example maps are shown in Figure 7.1. When the size of the area is $0.5 * 0.5$, there are just a few pinwheels formed. Some parts of the small maps appear as crystal-like shapes. For example, in the patterns shown in the Figure at least two crystals can be seen. If the size of map areas is $1 * 1$, the maps are dominated by stripes perpendicular to the boundaries. There are long stripes and crystals formed for the same orientation preferences, respectively. The long stripes may be formed by crystals connecting to each other. These patterns of stripes and crystals are affected by pinwheels generated from the borders. These pinwheels gradually move into the central areas of the maps and collide with other pinwheels so that pinwheel annihilation and creation happens. If the size of the cortical area is $2 * 2$, clear rhombuses are formed and observed, especially in the center area. When the size of maps becomes $3 * 3$, the patterns appear more regular than the patterns of smaller maps. They consist of clear crystals mostly and some stripes near the boundaries. The shapes of the crystals are similar with rhombus and the stripes are formed by connection of some crystals. Compared to maps with its' size as $1 * 1$, there are no long stripes across the whole areas for maps with its' size as $3 * 3$. In the early period of a few time scales, the patterns are not as regular as the later ones. And after some time scales, the maps show to be close to be static except for some pinwheels moving to outside and inside of the cortical area crossing the boundaries, respectively. For the maps close to be static in the late stage, the crystals or stripes are parallel to each other. Bigger areas of maps are thought to have less affection from the boundaries since the pinwheels on the central areas are farther from the borders. This is one motivation for us to consider the cases of maps with large areas.

7.2 The process of the map development for different system sizes

We analyze pinwheel statistics of the maps with different system size to reflect the characteristics of the map development process. Firstly, we plot average pinwheel densities of the different maps. When the area size of maps is $1 * 1$, at the beginning of development, e.g. $t = 1T^*$ (T^* is the time scale), the average pinwheel density of the maps is around 3 and a part of the confidence interval locates at the experiment observation range. As time proceeds, the confidence interval of the average pinwheel density falls below 3 and stands around 2.5 and keeps somewhat stable level. Compared to the maps with area size as $1 * 1$, the average of pinwheel densities for map area as $2 * 2$ and $3 * 3$ have relatively small confidence intervals. This means

the fluctuation for different maps generated from different random seeds is small for them. Similarly, the average pinwheel densities for map size as 2×2 or 3×3 at the beginning of the development are also around 3 and then after a few time scales drop below 3 and locate closely to 2.5. See Figure 7.2.

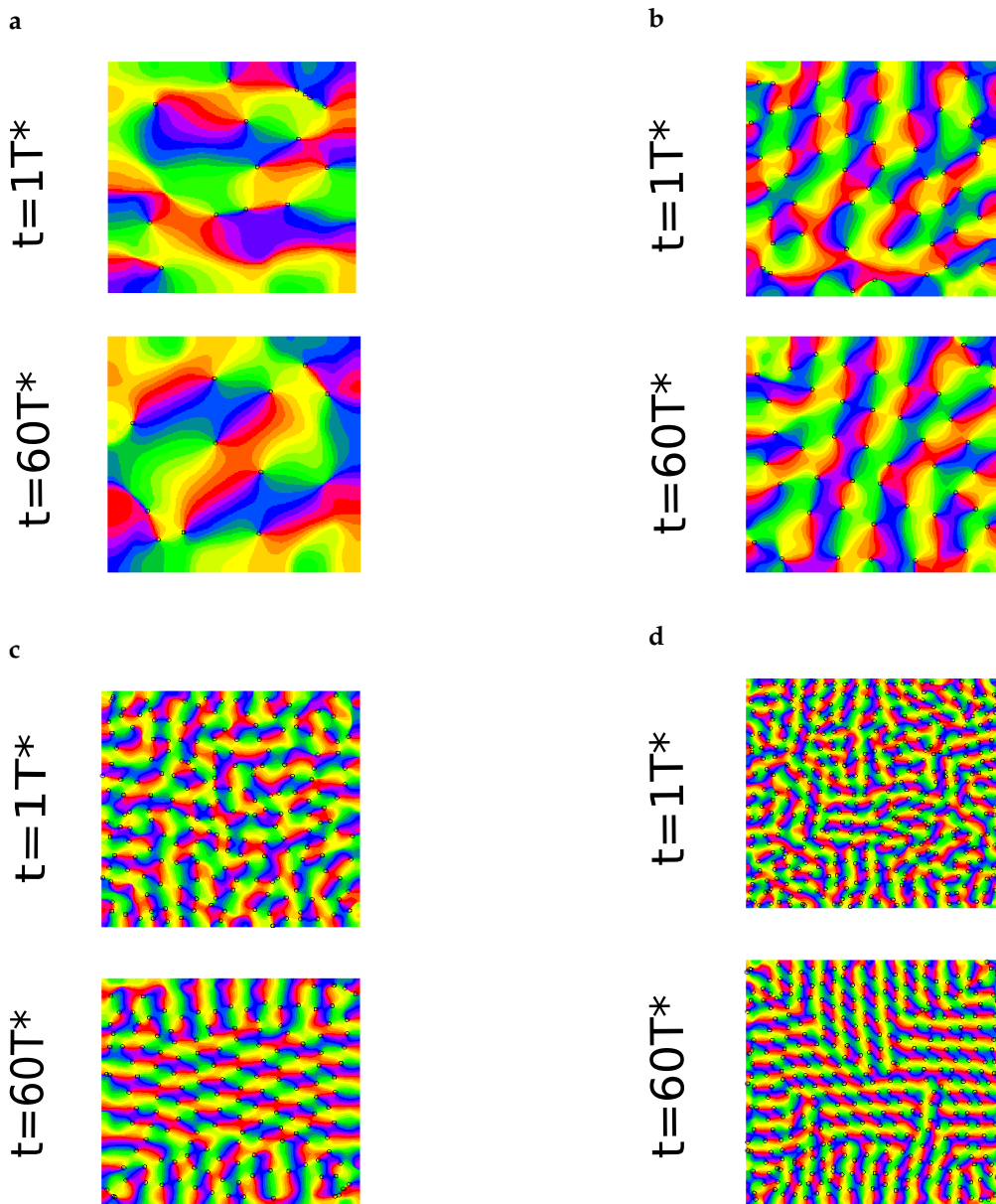


Figure (7.1) A map for area size as 0.5×0.5 when $t = 1T^*$ and $t = 60T^*$ (a). A map for area size as 1×1 when $t = 1T^*$ and $t = 60T^*$ (b). A map for area size as 2×2 when $t = 1T^*$ and $t = 60T^*$ (c). A map for area size as 3×3 when $t = 1T^*$ and $t = 60T^*$ (d).

Then we do the analysis of other pinwheel statistics including nearest neighbor (NN) distance distribution of pinwheel centers and the standard deviation of pinwheel densities.

Firstly $t = 60T^*$ we plot the nearest neighbor distance distributions of pinwheel

centers and the fitting function curves. See Figure 7.3. For maps with area size as $1 * 1$, the 3 types of NN distance distributions are obviously decentralized and not fitting to the function curves. As to maps with area size as $2 * 2$ or $3 * 3$, the NN distance distributions are more centralized for the same charge, the opposite charge and the arbitrary charge of pinwheels, however also deviate from the fitting functions. The mean NN distances as functions of time are shown in Figure 7.4. When the area size is $1 * 1$, the confidence interval including the mean NN distance without considering pinwheel charges increases from the beginning and stays outside of the experiment observation region. The confidence interval including the mean NN distance with the opposite pinwheel charge have a similar trend with it and also grows from the beginning and lies above the experiment scope. For the confidence interval including the mean NN distance with the same pinwheel charge basically it largely overlap the experiment observation area. When the area size is $2 * 2$ or $3 * 3$, the confidence intervals for the mean NN distance without considering charges of pinwheels, with the opposite pinwheel charges have similar characteristics. All of them increase from the beginning and then keep above the experiment observation areas. For the mean NN distance with same charges of pinwheels, the confidence interval for the area size as $2 * 2$ or $3 * 3$ lies inside the experiment scopes.

In addition, we fit the empirically observe power law, to the standard deviation of pinwheel density estimate in randomly selected circular regions of size A (Figure 7.5). We need to show the variability exponent r and the variability constant c . When the area size of maps is $1 * 1$, the confidence interval of the variability constant c is below the experiment observation area and the confidence interval of the variability exponent r basically is above or close to the area. Then we evaluate the standard deviation of pinwheel densities as a function of the area A of randomly selected subregions of the iso-orientation domain layout. In the figure the black line is the standard deviation for 2 dimensional Poisson process of pinwheel density π . The pinwheel density variability deviates from standard deviation of a 2 dimensional Poisson process of pinwheel density π . We show for example the case of $t = 60T^*$. When the area size of maps is $2 * 2$, similar with the area size of maps as $1 * 1$, the confidence interval of the variability constant c is below the experiment observation area and the confidence interval of the variability exponent r basically is above the area. We also show a example for $t = 60T^*$ the pinwheel density variability deviates more largely from standard deviation of a 2 dimensional Poisson process of pinwheel density π than the case of the map area size as $1 * 1$. Now we consider the cases for the map area size as $3 * 3$. Still similar with the previous two cases, the confidence interval of the variability constant c is below the experiment observation area and the confidence interval of the variability exponent r basically is above the area. Then we can for example for $t = 60T^*$ find the the pinwheel density variability deviates most largely from standard deviation of a 2 dimensional Poisson process of pinwheel density π between the three cases of the map area size as $1 * 1$, $2 * 2$ and $3 * 3$.

As the results of the pinwheel statistics show, the pinwheel layouts for maps with the area size as $1 * 1$, $2 * 2$ and $3 * 3$ fails to match the common design.

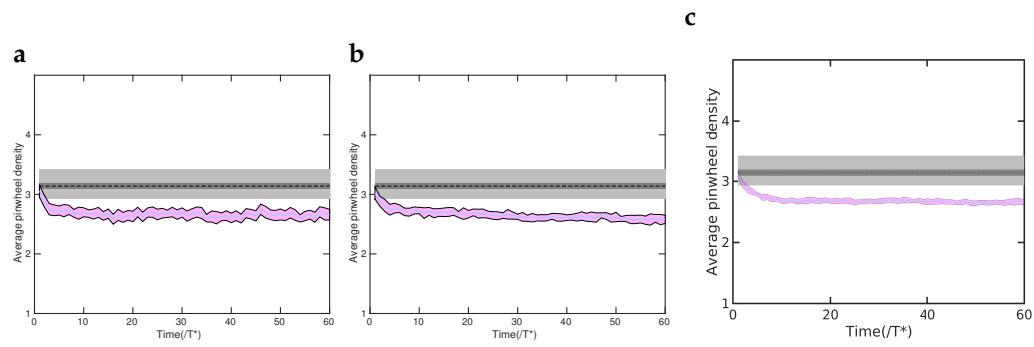


Figure (7.2) The average pinwheel density for the area size as 1×1 (a). The average pinwheel density for the area size as 2×2 (b). The average pinwheel density for the area size as 3×3 (c).

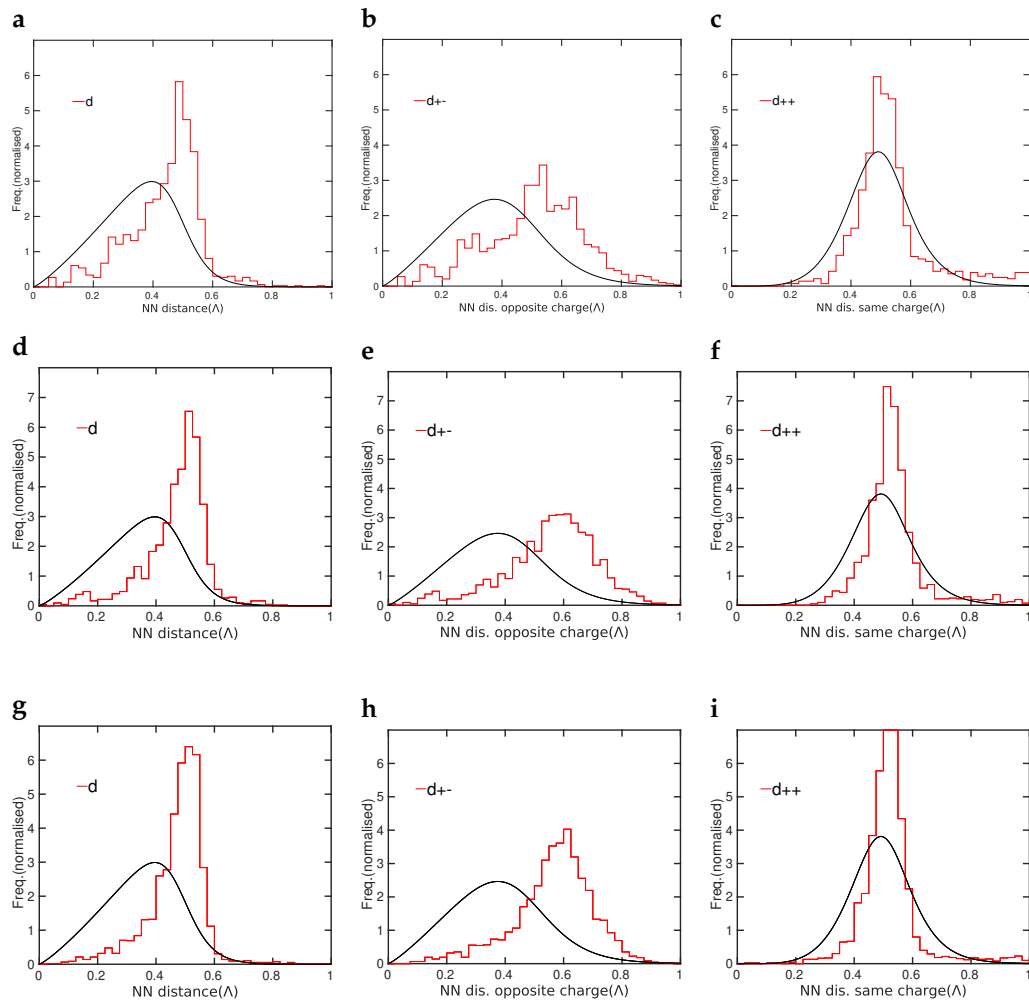


Figure (7.3) The NN distance distributions for $t = 60T^*$. The NN distance distribution for arbitrary pinwheel charges for the area size as 1×1 (a). The NN distance distribution for opposite pinwheel charges for the area size as 1×1 (b). The NN distance distribution for same pinwheel charges for the area size as 1×1 (c). The NN distance distribution for arbitrary pinwheel charges for the area size as 2×2 (d). The NN distance distribution for opposite pinwheel charges for the area size as 2×2 (e). The NN distance distribution for same pinwheel charges for the area size as 2×2 (f). The NN distance distribution for arbitrary pinwheel charges for the area size as 3×3 (g). The NN distance distribution for opposite pinwheel charges for the area size as 3×3 (h). The NN distance distribution for same pinwheel charges for the area size as 3×3 (i).

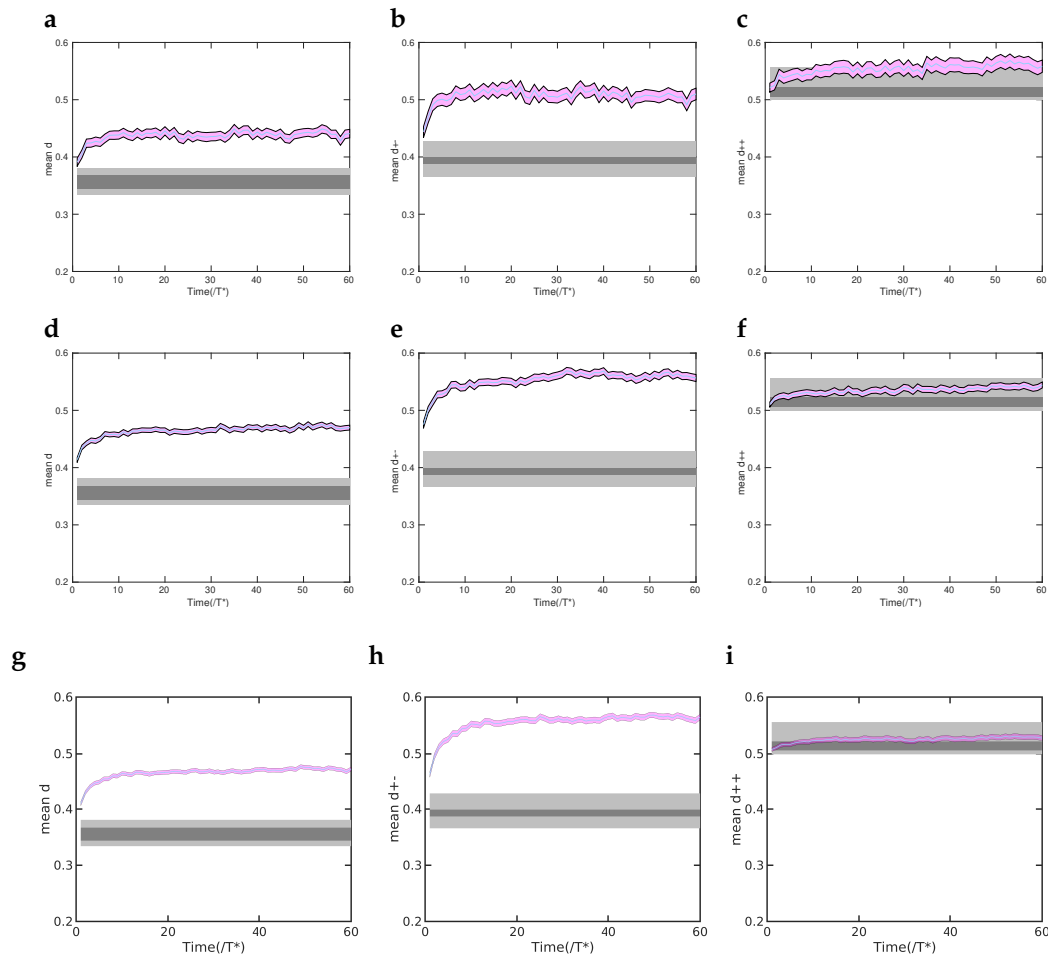


Figure (7.4) The mean NN distance for arbitrary pinwheel charges for the area size as 1×1 (a). The mean NN distance for opposite pinwheel charges for the area size as 1×1 (b). The mean NN distance for same pinwheel charges for the area size as 1×1 (c). The mean NN distance for arbitrary pinwheel charges for the area size as 2×2 (d). The mean NN distance for opposite pinwheel charges for the area size as 2×2 (e). The mean NN distance for same pinwheel charges for the area size as 2×2 (f). The mean NN distance for arbitrary pinwheel charges for the area size as 3×3 (g). The mean NN distance for opposite pinwheel charges for the area size as 3×3 (h). The mean NN distance for same pinwheel charges for the area size as 3×3 (i).

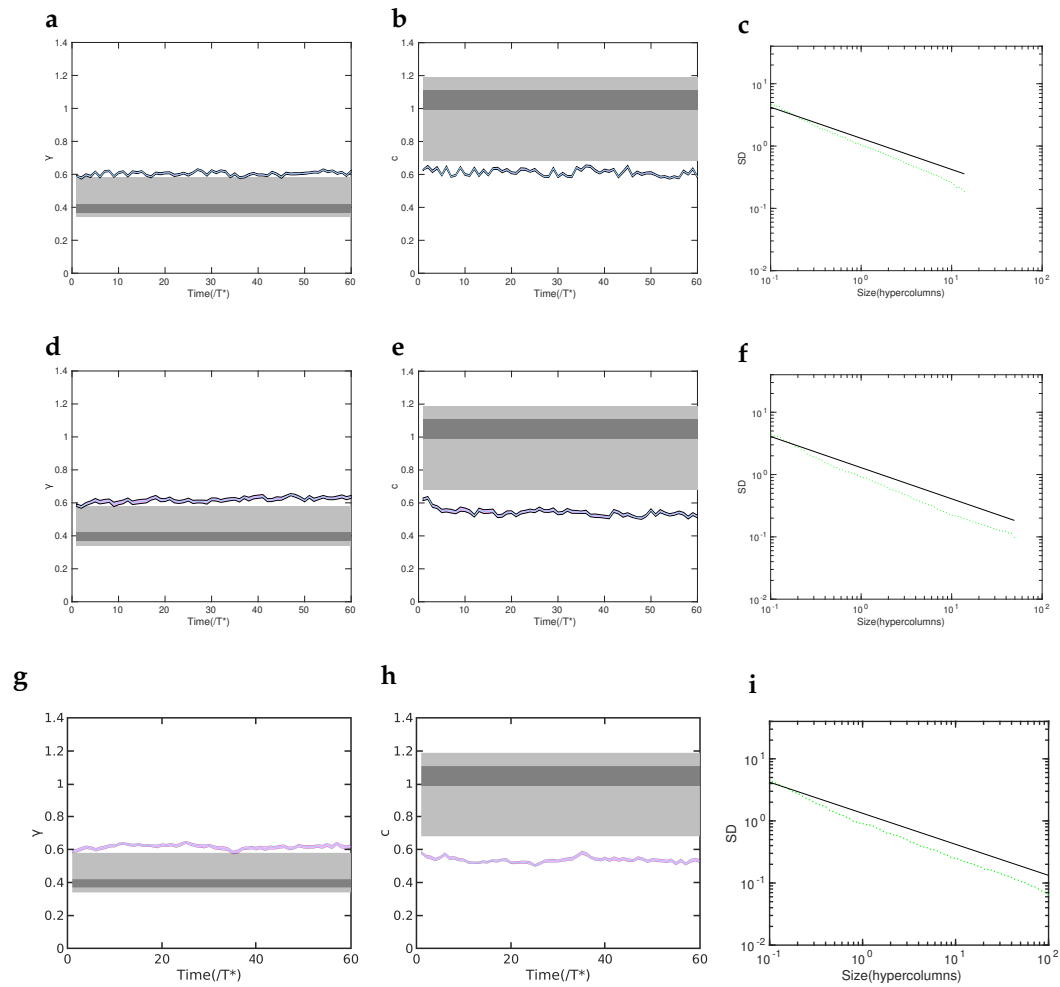


Figure (7.5) r for the area size as 1×1 (a). c for the area size as 1×1 (b). SD for the area size as 1×1 when $t = 60T^*$ (c). r for the area size as 2×2 (d). c for the area size as 2×2 (e). SD for the area size as 2×2 when $t = 60T^*$ (f). r for the area size as 3×3 (g). c for the area size as 3×3 (h). SD for the area size as 3×3 when $t = 60T^*$ (i).

Chapter 8

Changing learning rates

8.1 Introduction

Learning rate is an important parameter of activity driven cortical circuit rearrangement that can only be investigated in the framework of stimulus driven models. Fundamentally learning rate controls a central qualitative feature of the circuit self-organization process the effective noise level and the relative contribution of fluctuation-driven and state-driven changes to circuit remodelling. Large learning rates imply a large impact of individual stimuli and cortical activity patterns on the resulting circuit changes. In the limit of arbitrarily small learning rates only deterministic state dependent changes drive circuit remodelling. Small learning rates thus strengthen the relative impact of the prior circuit structure relative to individual activity events. Comparing results for different learning rates thus enables to test whether elementary remodelling steps such as pinwheel pair generation or annihilation are driven by fluctuations or by circuit state.

8.2 Map structure for different learning rates

We choose the maps for the learning rate as 0.02 to compare with the maps for the learning rate as 0.1. The similar places for the two types of map development are that they have long stripes which are the connection of crystal shapes and dominate the simulation areas. See Figure 8.1. The different things for them are for the maps with smaller learning rates, e.g. learning rate 0.02, the maps change slowly and smoothly. Their pinwheels move gradually, not like maps with learning rate as 0.1 whose pinwheels move fast and fiercely. But for smaller learning rates, the map development doesn't become static finally but still change all the time. The time scales for the map development with the learning rate as 0.02 are about 5 times the time scale for the map development with the learning rate as 0.1.

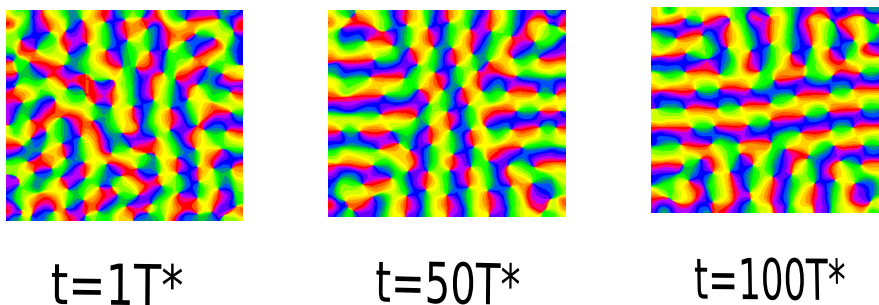


Figure (8.1) The observation for maps with learning rate 0.02 at different time stage.

8.3 Pinwheel movement for different learning rates

We perform pinwheel tracking analysis for the pinwheel movement with learning rates as 0.02 and 0.1, as shown in Figure 8.2. Both of them have tense pinwheel creation and annihilation events happening near the borders of cortical areas. More pinwheel creation and annihilation events happen near the boundaries than those events happen at central areas. For maps with learning rate as 0.1, there are also more pinwheel creation and annihilation events happening except for near boundaries but around the center position. Also the directions for pinwheel moving from the beginning to the end of the observation period for the map development are shown in the Figure. In addition, the figures of vector average show the distribution of directions for pinwheel movement. For maps with learning rates as 0.1 they have more activities of pinwheel creation and annihilation generated than maps with learning rates as 0.02 during the development process.

How many pinwheels of the pattern in the early stage are still present in the late stage? For a given set of pinwheels at a early time t we further calculate the fraction of pinwheels surviving until time $t + w$, w can be different time windows. We choose $w = 50T^*$, $150T^*$ and $250T^*$. For maps with learning rates as 0.02, if $w = 50T^*$, we can observe that at the first about 50 time scales the surviving fraction is lower than the later period and increases from about 50% to 80%. If $w = 150T^*$, the surviving fraction increase from about 20% to 50%. If $w = 250T^*$, the surviving fraction is shown as increase from about 15% to 30%. Actually the curve for $w = 250T^*$ is close to the one for $w = 150T^*$ during the time. By comparison, to maps with learning rates as 0.1 the surviving fractions for different time windows are more stable. As for $w = 50T^*$ the fraction keeps at the level of about 50%. For $w = 150T^*$ the fraction increases from the beginning and then stays at about 25% level. For $w = 250T^*$ the level is lower than the other two and is about 10%. The Figure indicates the longer time the w is, the smaller pinwheels' surviving fraction until $t + w$ is.

8.4 Pinwheel statistics for different learning rates

Firstly, we look at the average pinwheel densities of maps with learning rates as 0.1 and 0.02. Results show the average pinwheel density for the learning rate 0.1 is a little smaller than the average pinwheel density for the learning rate 0.02. The trend is similar and both of them at the beginning are about 3.1 and then decrease to about 2.6 at later time periods. Average pinwheel densities are relate to average pinwheel number. As shown by the Figure 8.3 the maps with the learning rate as 0.1 have less pinwheel number than the maps with the learning rate as 0.02. Similar with average pinwheel densities, the trend for average pinwheel number is also decreasing from the starting.

Then we fit the empirically observe power law, to the standard deviation of pinwheel density estimate in randomly selected circular regions of size A . The standard deviations for maps at $t = 100T^*$ with the two learning rates somewhat overlap or are significantly close to each other.

We also plot the NN distance distributions for pinwheels with the arbitrary, the same and the opposite charge for $t = 100T^*$. We find that the distributions for maps with learning rates as 0.1 and 0.02 are not far from each other.

The pinwheel change during the map development comes from two parts. One part is because pinwheels are created or annihilate in the process. Another part is pinwheels move from outside of the simulation area or move to inside of the cortical

area. We show two figures separately about this aspect. In Figure 8.3 in the beginning more pinwheels annihilate than pinwheels are created. and lately pinwheel creation number and annihilation number are similar. The pinwheels for learning rates as 0.1 have slightly more events for the creation and annihilation than the pinwheels for learning rates as 0.02. In another figure the pinwheels moving into the simulation area are more than the pinwheels moving to outside of the cortical area. Also the number of pinwheels for moving between outside and inside of the simulation area with the learning rate 0.1 are higher than the number of pinwheels with the learning rate 0.02. The total change of pinwheel number for pinwheel creation, annihilation, moving from outside to inside or from inside to outside of the simulation area is also shown in the figure.

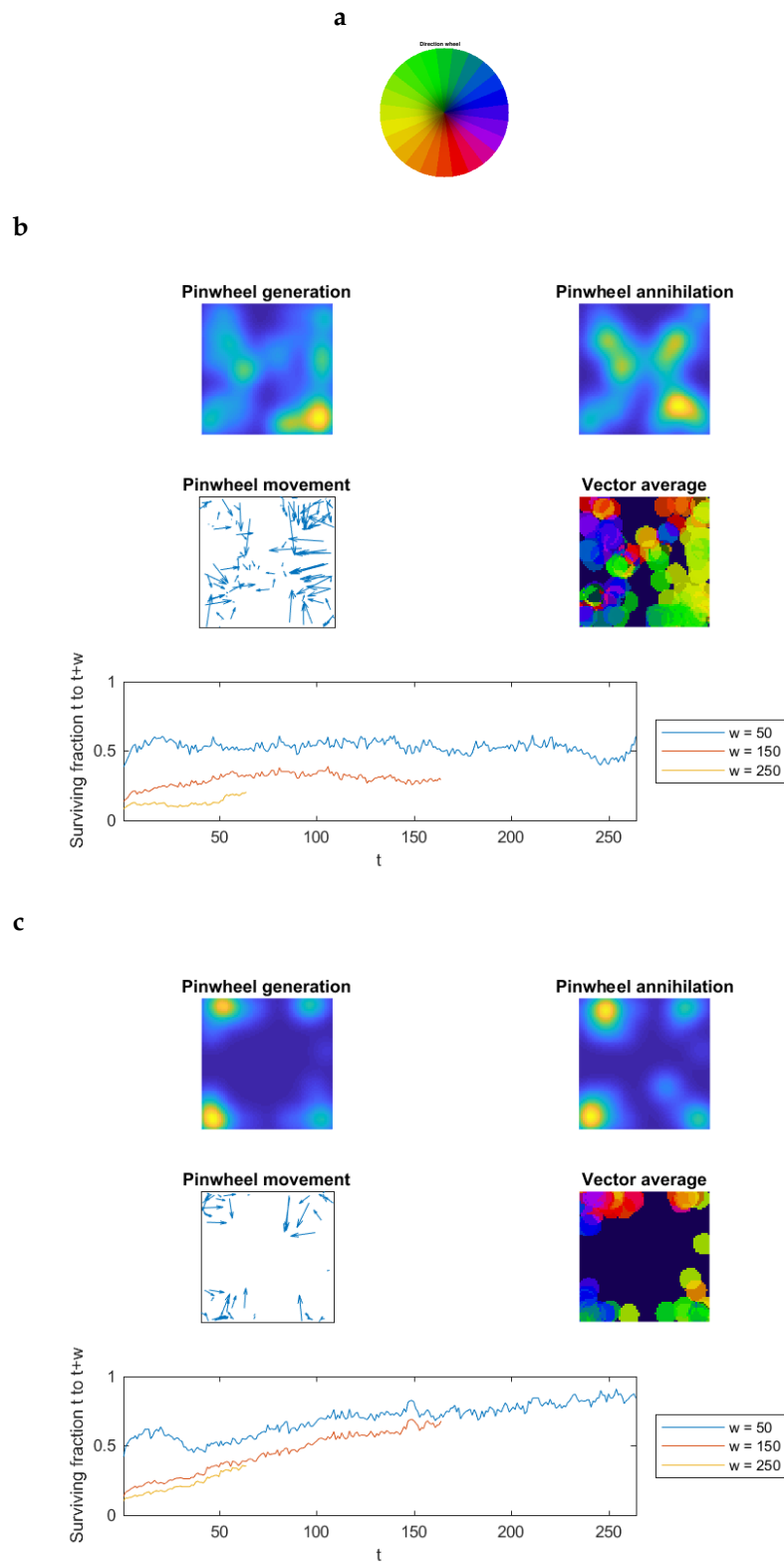
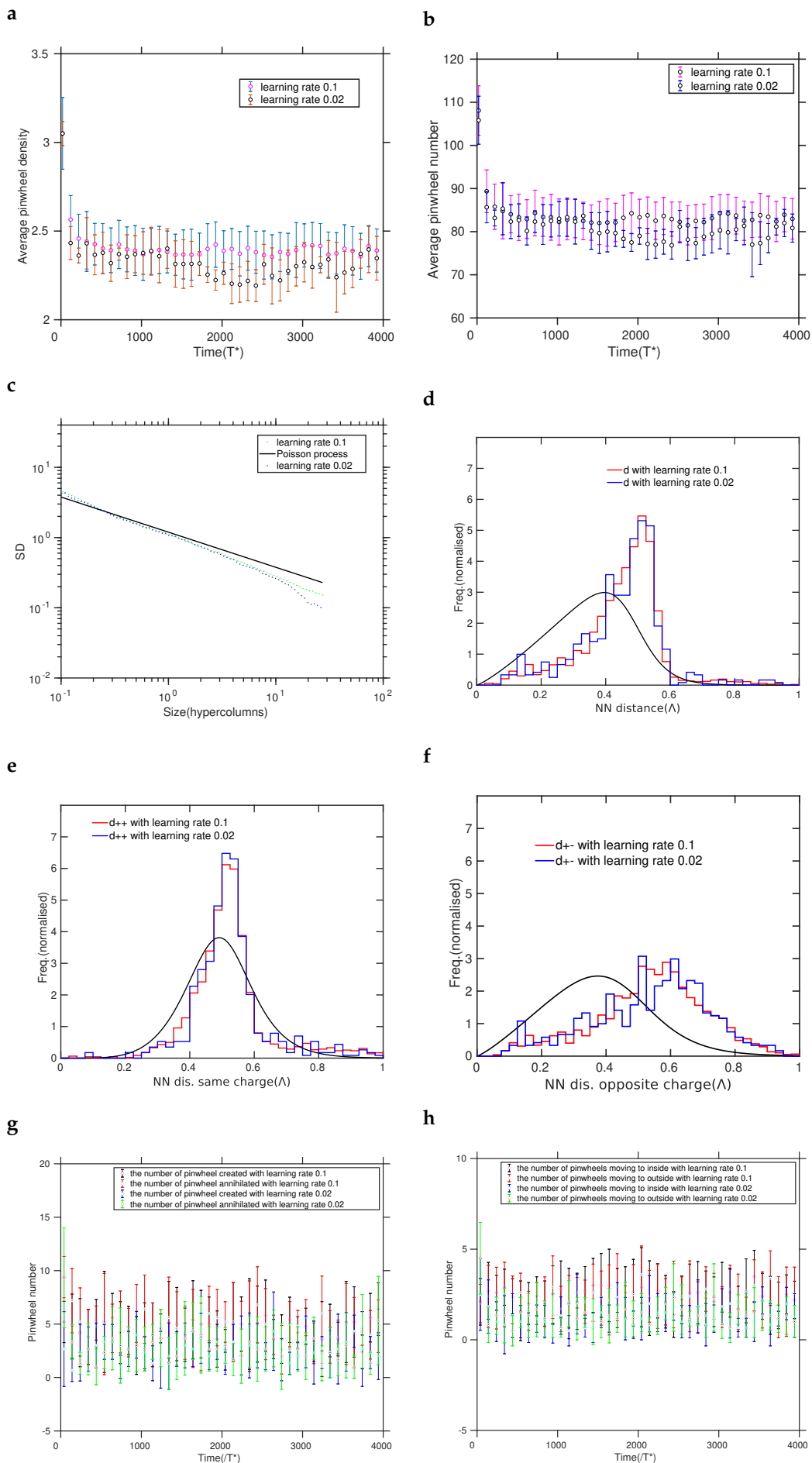


Figure (8.2) The directions represented by different color (a). The analysis of pinwheel movement for maps with learning rate 0.1 (above) and 0.02 (below) (b)(c). The heat maps for pinwheel generation and annihilation in the cortical areas are shown. Also the arrows indicate the directions of pinwheel movement during the time course. Vector average codes the directions of pinwheel movement. The surviving fractions of pinwheels during the time course are given.



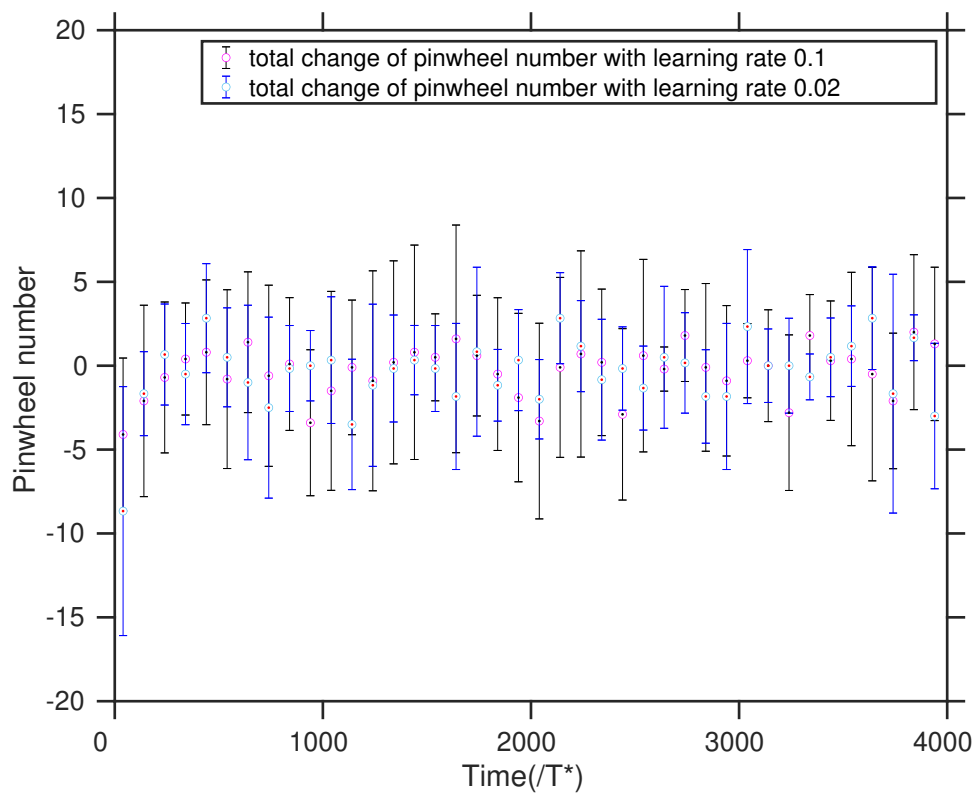


Figure (8.3) The comparison of pinwheel statistics between maps with learning rate 0.1 and 0.02. The NN distributions are obtained when $t=100T^*$ for(d)(e)(f).

Chapter 9

Impact of inhibitory interactions in the model

9.1 Introduction

While short range excitatory interactions are essential for the formation of local clusters of similar tuning properties, longer ranged inhibitory interactions are both important for the selection of a typical spacing of adjacent orientation domains and potentially for the results of pattern selection. In order to explore the impact of this parameter relative to the parameters used in the original Topographica model, we examined the impact of changes of this parameter on pattern formation and pinwheel dynamics.

9.2 Maps generated by the model with different inhibitory interaction ranges

We first show three snapshots of maps for $t = 1T^*$, $t = 30T^*$ and $t = 60T^*$. For an inhibitory interaction range of 0.4, the map consists of patches and stripes. Besides, there are some shadow areas distributed in the map. As for the inhibitory interaction range as 0.6, when $t = 1T^*$ the map is basically formed by patches. Also the size of the patches seem to be larger than the size of the patches of the map for the inhibitory interaction range as 0.4. In later stage for $t = 30T^*$ and $t = 60T^*$, long stripes appeared and the width of some stripes for $t = 60T^*$ is larger than the one for $t = 30T^*$. Also shadow places are seen for these maps. When the inhibitory interaction range is 0.8, for $t = 1T^*$ the map mainly contains patches and in later time, e.g. $t = 30T^*$ and $t = 60T^*$ long stripes are formed. In addition, shadows can also be seen in these maps. See Figure 9.1.

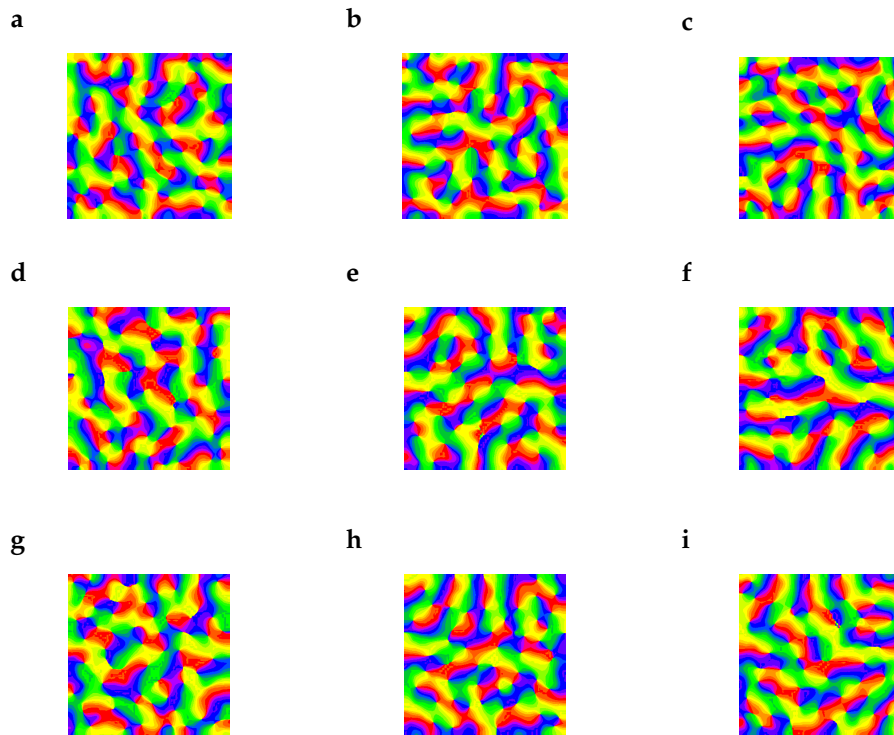


Figure (9.1) A map for $t = 1T^*$ for the inhibitory interaction as 0.4(a). A map for $t = 30T^*$ for the inhibitory interaction as 0.4(b). A map for $t = 60T^*$ for the inhibitory interaction as 0.4(c). A map for $t = 1T^*$ for the inhibitory interaction as 0.6(d). A map for $t = 30T^*$ for the inhibitory interaction as 0.6(e). A map for $t = 60T^*$ for the inhibitory interaction as 0.6(f). A map for $t = 1T^*$ for the inhibitory interaction as 0.8(g). A map for $t = 30T^*$ for the inhibitory interaction as 0.8(h). A map for $t = 60T^*$ for the inhibitory interaction as 0.8(i).

9.3 The process of the map development for different inhibitory interaction ranges in the model

We will analyze the pinwheel statistics for the map development with different inhibitory interaction ranges to characterize the development process.

Firstly we plot the average pinwheel density of maps during the process. See Figure 9.2. For the inhibitory interaction range as 0.4, the average pinwheel densities and the confidence interval are shown in the Figure. The values of the average pinwheel densities locate between 2.5 and 3. There is a fluctuation for the average pinwheel densities during the course and the confidence interval have small parts in the experiment observation area. For the inhibitory interaction range as 0.6, the values of average pinwheel densities are around 2.5. The confidence interval is basically under the experiment value region. As for the inhibitory interaction range as 0.8, the values of average pinwheel densities are between 2 and 2.5, and the confidence interval is below the experiment observation scope.

Secondly, we do the analysis for nearest neighbor distance distribution of pinwheels. See Figure 9.3. For $t = 60T^*$ we plot the nearest neighbor distance distribution of pinwheels and the fitting function curves. For the inhibitory interaction

range as 0.4, the distributions are not fitted by the fitting functions. We also analyze mean NN distances as functions of time. See Figure 9.4. For the mean NN distance without considering the charge of pinwheels, the confidence interval stays above the experimental observation area during the time course. When we consider the mean NN distance for the pinwheels with the opposite charge, the confidence interval lies outside of the experimental observation area. As for the mean NN distance with the same charge of pinwheels, the confidence interval basically fills the experiment observation region. When the inhibitory interaction range is 0.6, similarly as the inhibitory interaction range as 0.4, the fitting functions deviate from the NN distance distribution curves. We also plot the mean NN distances as functions of time in the figures. As for the mean NN distance without considering charges of pinwheels, the confidence interval starts from the experiment value area and then leaves the area during the time course. For the mean NN distance for the pinwheels with the opposite charge, the confidence interval also grows from location at inside of the experiment area and then stays above the area. For the mean NN distance for the pinwheels with the same charge, during the time course the confidence interval has some intersections with the experimental observation area. When the inhibitory interaction range is 0.8, the NN distributions can't be fitted by the fitting functions. Then we analyze the mean NN distances as functions of time. For the mean NN distance without considering charges of pinwheels, except at some short time sections the confidence interval intersects with the experimental observation area and at other time range it lies outside of the area. For the mean NN distance with the opposite charge of pinwheels, the confidence interval basically stays outside of the experimental observation area. For the mean NN distance with the same charge of pinwheels, the confidence interval overlaps some parts of the experiment observation region and only a few short line sections of the mean NN distance lie in the region .

Besides, we fit the empirically observe power law, to the standard deviation of pinwheel density estimate in randomly selected circular regions of size A (Figure 9.5). We will also show the variability exponent r and the variability constant c . When the inhibitory interaction range is 0.4, the confidence interval of the variability exponent r basically is outside of the experimental observation area except at a few time intervals it is located inside of area, and the confidence interval of the variability constant c is below the area except at a very short interval during the time course. Then we evaluate the standard deviation of pinwheel densities as a function of the area A of randomly selected subregions of the iso-orientation domain layout. In the figure the black line is the standard deviation for 2 dimensional Poisson process of pinwheel density π . The pinwheel density variability deviates from standard deviation of a 2 dimensional Poisson process of pinwheel density π . We show for example the case of $t = 60T^*$. For the inhibitory interaction range as 0.6, the confidence interval of variability exponent r at the time interval for the beginning lies outside of the experimental observation area and lately it enters the area and then intersects with the border of the area several times, while the confidence interval of the variability constant c also at the beginning time interval locates at outside of the area and then it goes into inside of the area and crosses the boundary for several times. Then we find the pinwheel density variability deviates more closely from standard deviation of a 2 dimensional Poisson process of pinwheel density π than the case of the inhibitory interaction range as 0.4. We give an example of the case of $t = 60T^*$. For the inhibitory interaction range as 0.8, the confidence interval of the variability exponent r and the confidence interval of the variability constant c intersect with the boundaries of the experiment observation areas for some times.

Then we find the the pinwheel density variability deviates from standard deviation of a 2 dimensional Poisson process of pinwheel density π . An example of the case of $t = 60T^*$ is shown.

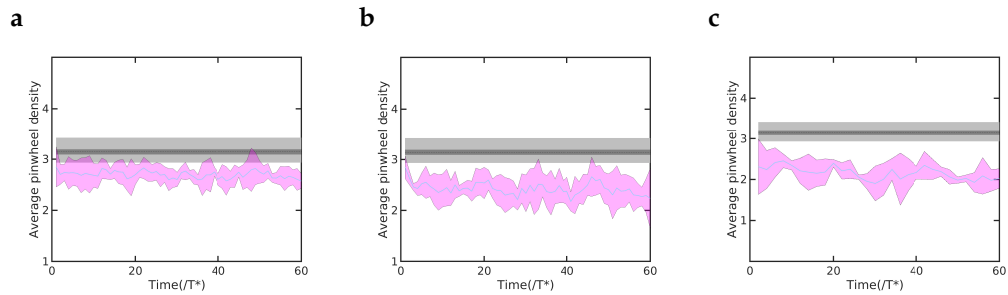


Figure (9.2) The average pinwheel density of maps for the inhibitory interaction range as 0.4 (a). The average pinwheel density of maps for the inhibitory interaction range as 0.6 (b). The average pinwheel density of maps for the inhibitory interaction range as 0.8 (c).

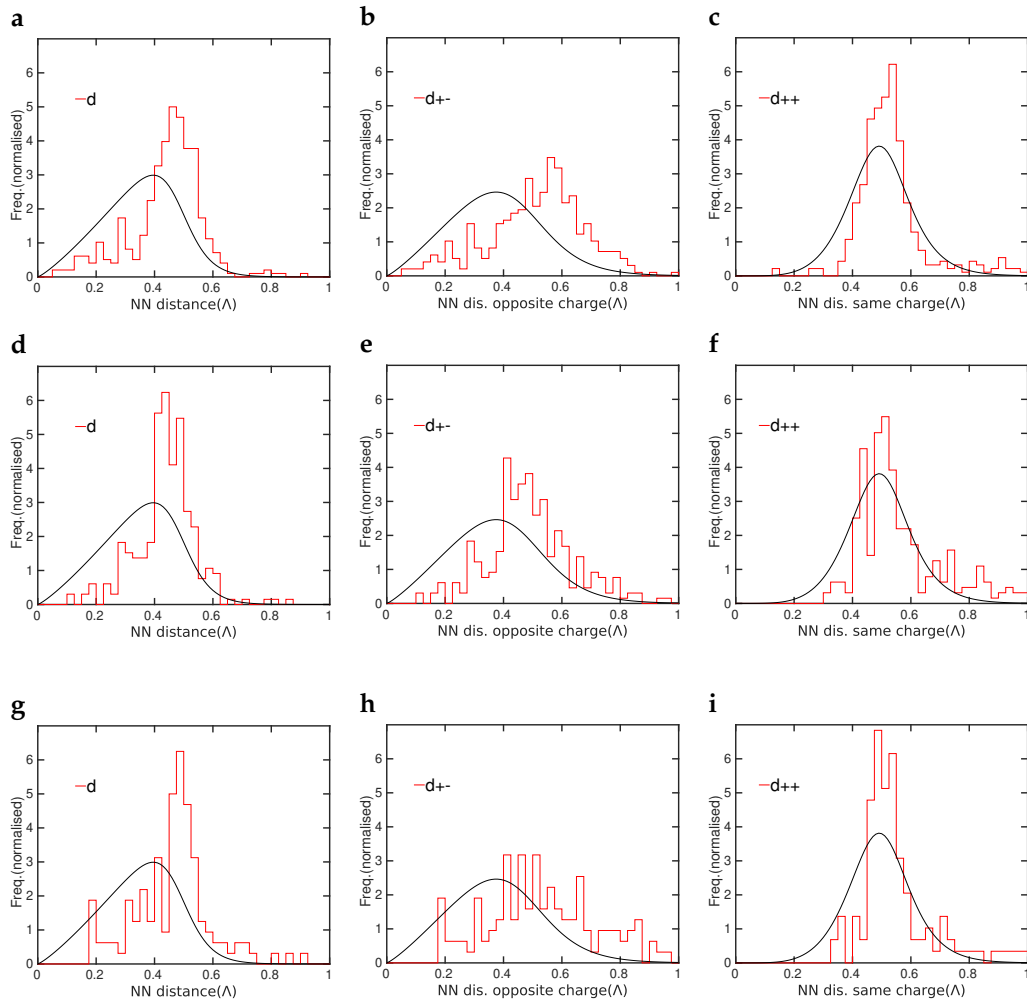


Figure (9.3) The NN distance distribution for arbitrary pinwheel charges of maps for the inhibitory interaction range as 0.4 when $t = 60T^*$ (a). The NN distance distribution for opposite pinwheel charges of maps for the inhibitory interaction range as 0.4 when $t = 60T^*$ (b). The NN distance distribution for same pinwheel charges of maps for the inhibitory interaction range as 0.4 when $t = 60T^*$ (c). The NN distance distribution for arbitrary pinwheel charges of maps for the inhibitory interaction range as 0.6 when $t = 60T^*$ (d). The NN distance distribution for opposite pinwheel charges of maps for the inhibitory interaction range as 0.6 when $t = 60T^*$ (e). The NN distance distribution for same pinwheel charges of maps for the inhibitory interaction range as 0.6 when $t = 60T^*$ (f). The NN distance distribution for arbitrary pinwheel charges of maps for the inhibitory interaction range as 0.8 when $t = 60T^*$ (g). The NN distance distribution for opposite pinwheel charges of maps for the inhibitory interaction range as 0.8 when $t = 60T^*$ (h). The NN distance distribution for same pinwheel charges of maps for the inhibitory interaction range as 0.8 when $t = 60T^*$ (i).

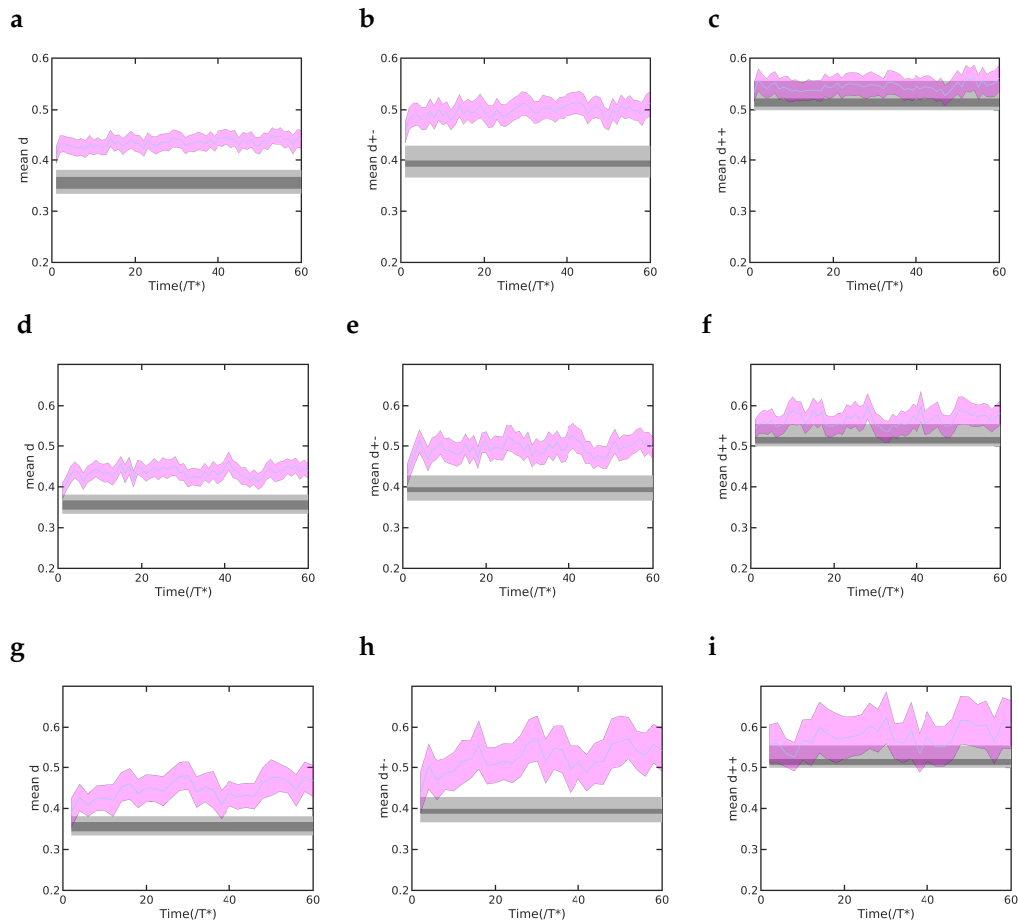


Figure (9.4) The mean NN distance for arbitrary pinwheel charges of maps for the inhibitory interaction range as 0.4 (a). The mean NN distance for opposite pinwheel charges of maps for the inhibitory interaction range as 0.4 (b). The mean NN distance for same pinwheel charges of maps for the inhibitory interaction range as 0.4 (c). The mean NN distance for arbitrary pinwheel charges of maps for the inhibitory interaction range as 0.6 (d). The mean NN distance for opposite pinwheel charges of maps for the inhibitory interaction range as 0.6 (e). The mean NN distance for same pinwheel charges of maps for the inhibitory interaction range as 0.6 (f). The mean NN distance for arbitrary pinwheel charges of maps for the inhibitory interaction range as 0.8 (g). The mean NN distance for opposite pinwheel charges of maps for the inhibitory interaction range as 0.8 (h). The mean NN distance for same pinwheel charges of maps for the inhibitory interaction range as 0.8 (i).

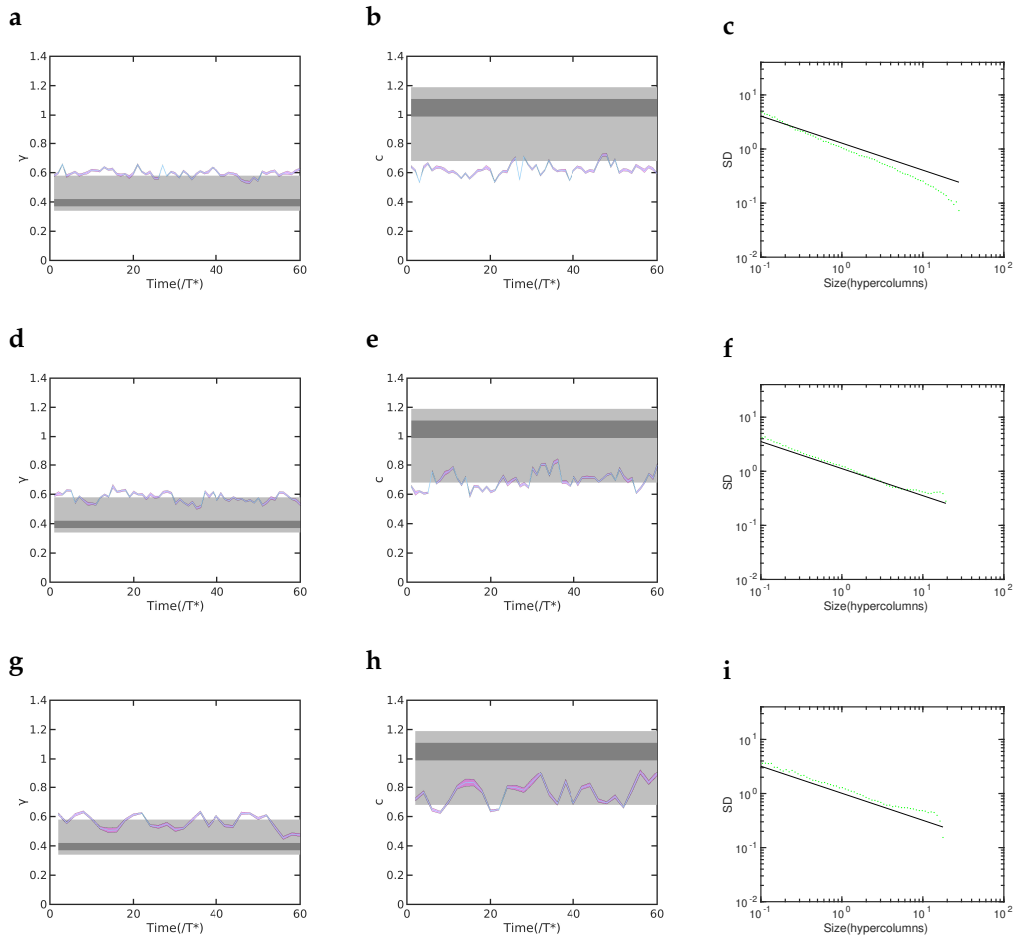


Figure (9.5) r for the inhibitory interaction range as 0.4 (a). c for the inhibitory interaction range as 0.4 (b). SD for the inhibitory interaction range as 0.4 (c). r for the inhibitory interaction range as 0.6 (d). c for the inhibitory interaction range as 0.6 (e). SD for the inhibitory interaction range as 0.6 (f). r for the inhibitory interaction range as 0.8 (g). c for the inhibitory interaction range as 0.8 (h). SD for the inhibitory interaction range as 0.8 (i).

Chapter 10

An analysis for correlated stimuli

10.1 Introduction

Previously we studied cases for randomly distributed Gaussian stimuli. Now we turn to describe properties of maps formed by using correlated stimuli which consist of a pair of 2 parallel Gaussian patterns. These correlated stimuli are considered to generate correlated cortical activity in the model visual cortex. This may be important for the long range neuronal interaction in the visual cortex as mentioned before.

10.2 Using correlated stimuli in the model

We choose three snapshots of $t = 1T^*$, $t = 50T^*$ and $t = 100T^*$ to show the appearance of maps during the development. We study two categories for simulation, one is using simulation area as $1.5 * 1.5$ and two Gaussian stimuli and another is using the same simulation area but four Gaussian stimuli which are two pairs of Gaussian patterns. In the first category, we give distance of two stimuli as 0.1, 0.3 and 0.5. In the second category, we fix the same distances of stimuluses as the first category. The pair of stimuli is two parallel Gaussian patterns and the distance of them is shown in Figure 10.1.

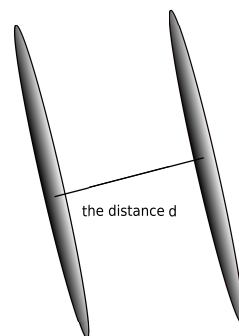


Figure (10.1) The pair of Gaussian stimuli used as a pair of correlated stimuli in the simulation. The meaning of "distance" is for the distance between the centers of two Gaussian patterns.

The layouts of maps for the two categories are shown in the Figure 10.2 and Figure 10.3. They are not crystal-like and randomly arranged. We need to perform statistical analysis to characterize the layouts of the maps.

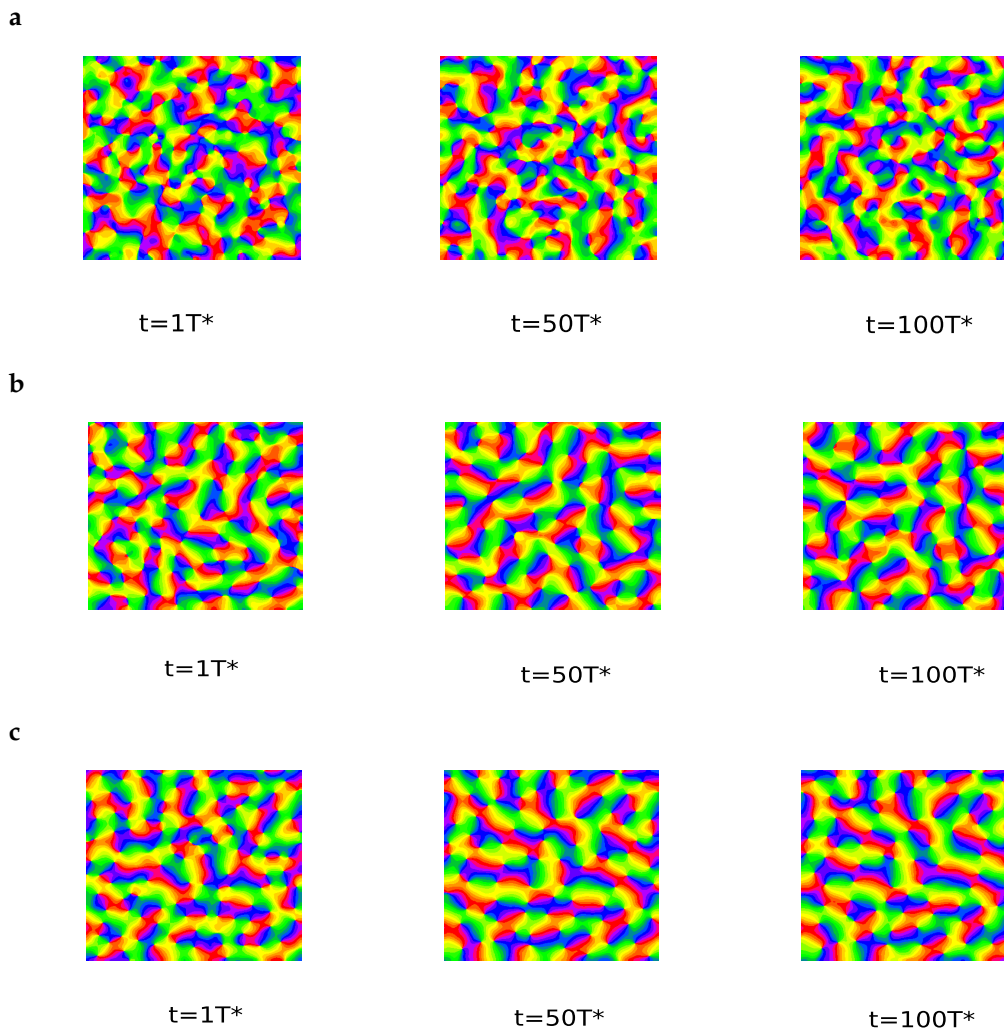


Figure (10.2) The maps for 1 pair of Gaussian patterns and the distance of 2 Gaussian stimuli as 0.1 (a). The maps for 1 pair of Gaussian patterns and the distance of 2 Gaussian stimuli as 0.3 (b). The maps for 1 pair of Gaussian patterns and the distance of 2 Gaussian stimuli as 0.5 (c).

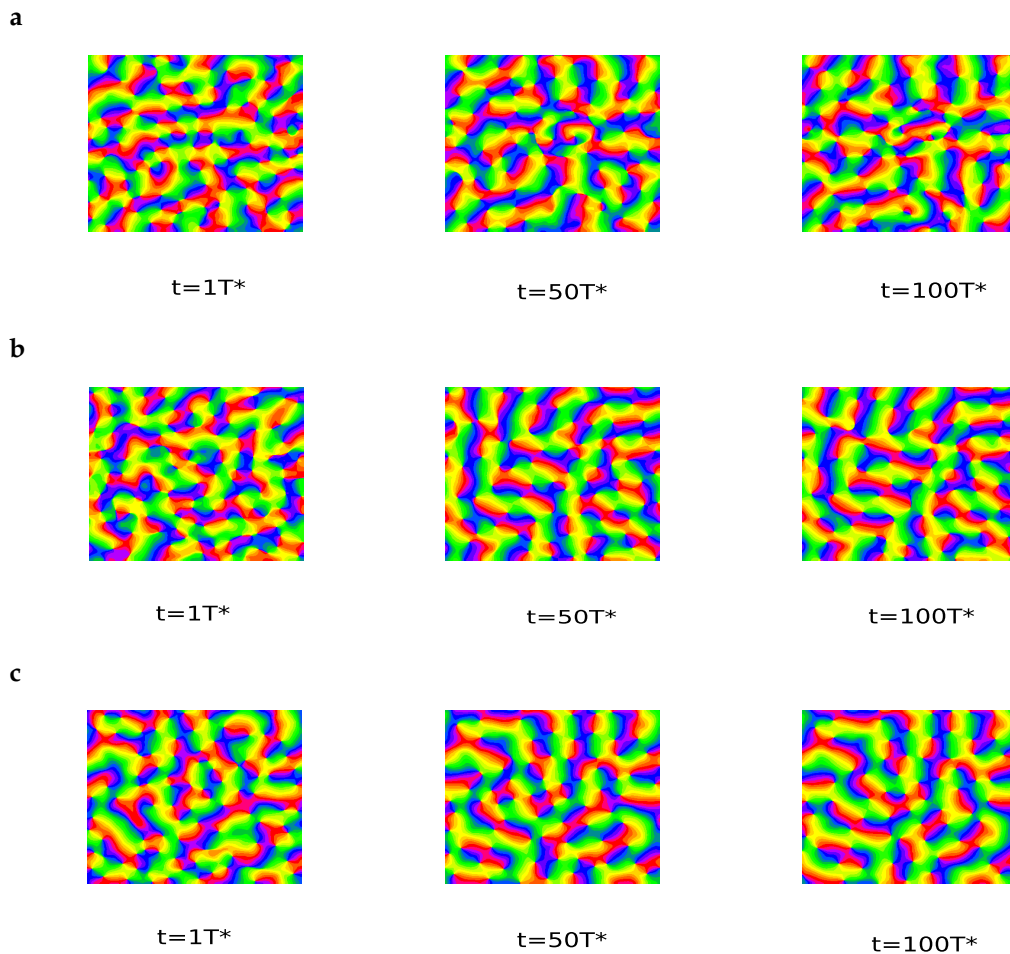


Figure (10.3) The maps for 2 pair of Gaussian patterns and the distance of 2 Gaussian stimuli as 0.1 (a). The maps for 2 pair of Gaussian patterns and the distance of 2 Gaussian stimuli as 0.3 (b). The maps for 2 pair of Gaussian patterns and the distance of 2 Gaussian stimuli as 0.5 (c).

10.3 The process of the map development for using correlated stimuli

10.3.1 Pinwheel statistics for area size 1.5*1.5 and 1 pair of stimuli

In the first category, when the distance of two Gaussian stimuli is 0.1, the average pinwheel density of maps fluctuates between 4 and 6 during the time course and beyond the experimental observation area. The confidence interval also lies above the experiment scope. When the distance of two correlated stimuli is 0.3, the average pinwheel density of maps is located below the experimental observation area. The confidence interval gradually leaves the experiment scope but still has intersections with the scope in later stage. For the distance of two parallel stimuli is 0.5, the confidence interval of average pinwheel densities drops to below the experimental observation area and the mean pinwheel density keeps at the level of about 2.6 at later time. See Figure 10.4.

Then we analyze nearest neighbor distance distribution of pinwheels for the first category. Firstly we analyze mean NN distances as functions of time (Figure 10.6).

When the distance of 2 Gaussian stimuli is 0.1, all of confidence intervals of the mean NN distance without considering the charge of pinwheels, the mean NN distance for the pinwheels with the opposite charge or the same charge stays below the experimental observation areas, respectively. For the distance of 2 Gaussian stimuli as 0.3, both of confidence intervals of the mean NN distance without considering the charge of pinwheels, the mean NN distance for the pinwheels with the opposite charge grow and leave the experimental observation area during the time course, while the mean NN distance for the pinwheels with the same charge basically lies below the experimental observation area but at some time points it stands near the boundary of the area. The confidence interval of the mean NN distance for the pinwheels with the same charge overlaps small parts of the experimental observation region. When the distance of 2 Gaussian stimuli is 0.5, similarly with the case of the distance of 2 Gaussian as 0.3, both of confidence intervals of the mean NN distance without considering the charge of pinwheels, the mean NN distance for the pinwheels with the opposite charge increase and leave the experimental observation area from the beginning of the time course. The mean NN distance for the pinwheels with the same charge lies in the experimental observation area and some parts of it are located in the common design region. The corresponding confidence interval intersects with the experiment observation.

Secondly we choose $t = 100T^*$ and plot the nearest neighbor distance distribution of pinwheels and the fitting function curves for the first category (Figure 10.5). For the distance of 2 Gaussian patterns is 0.1, the NN distance distribution of pinwheels without considering pinwheel charge is aing around 0.3 and deviates from the fitting function. The NN dibout centerstance distribution for pinwheels with the same charge centers around 0.4 and doesn't fit the function. The NN distance distribution for the pinwheels with the opposite charge centers around 0.3 and fails to fit the given curve. When the distance of 2 parallel Gaussian stimuli is 0.3, the NN distance distribution of pinwheels without relating to the pinwheel charge centers around 0.5 and doesn't fit to the function. The NN distance distribution for pinwheels with the opposite charge centers around 0.6 and obviously deviates from the fitting curve. The NN distance distribution for pinwheels with the same charge centers around 0.5 and is relatively close but still not fitting to the function. For the distance of two correlated Gaussian as 0.5, the NN distance distribution of pinwheels without considering pinwheel charge centers around 0.5 and doesn't fit to the curve. The NN distance distribution for pinwheels with the opposite charge of pinwheels centers around 0.6 and deviates from the fitting function. The NN distance distribution for pinwheels with the same charge centers around 0.55 and fails to fit the function.

In the first category, additionally we fit the empirically observe power law, to the standard deviation of pinwheel density estimate in randomly selected circular regions of size A (Figure 10.7). We will also analyze the variability exponent r and the variability constant c . When the distance of 2 Gaussian stimuli is 0.1, the confidence interval of the variability exponent r is located in the experimental observation area and at some time intervals lies in the common design area during the time course. Besides, the confidence interval of the variability constant c also stays in the experimental observation area and at some time intervals is located in the common design area during the time evolution. Then we evaluate the standard deviation of pinwheel densities as a function of the area A of randomly selected subregions of the iso-orientation domain layout. In the figure the black line is the standard deviation for 2 dimensional Poisson process of pinwheel density π . The pinwheel density variability deviates from standard deviation of a 2 dimensional Poisson process of

pinwheel density π . We show for example the case of $t = 100T^*$. For the distance of 2 Gaussian stimuli as 0.3, the confidence interval of the variability exponent r firstly enters the experimental observation area from the outside of area at the beginning and after a short period leaves the experimental observation area during the time course. The confidence interval of the variability constant c stays below the experimental observation area during the time course. Then we see the pinwheel density variability deviates from standard deviation of a 2 dimensional Poisson process of pinwheel density π . We give an example of the case of $t = 100T^*$. When the distance of 2 Gaussian stimuli is 0.5, the confidence interval of the variability exponent r fluctuates around the border of the experimental observation area and in most of time lies inside the area. The confidence interval of the variability constant c stays below the experimental observation area during the time evolution. Then we plot the the pinwheel density variability deviates from standard deviation of a 2 dimensional Poisson process of pinwheel density π . An example of the case of $t = 100T^*$ is shown.

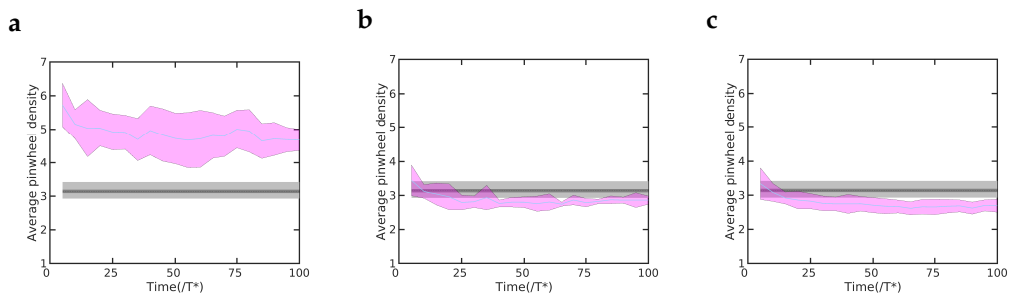


Figure (10.4) The number of stimuli is 1 pair. The average pinwheel density of maps for the distance of Gaussian stimuli as 0.1 (a). The average pinwheel density of maps for the distance of Gaussian stimuli as 0.3 (b). The average pinwheel density of maps for the distance of Gaussian stimuli as 0.5 (c).

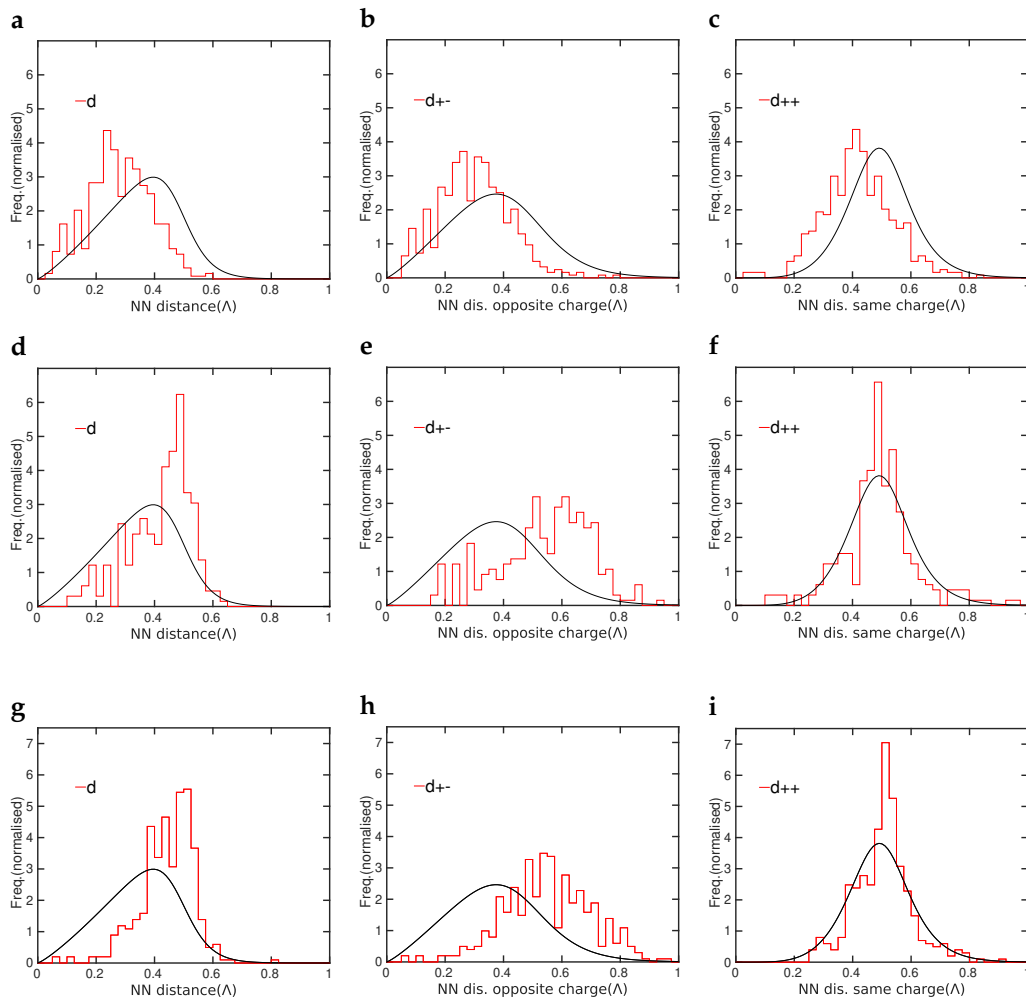


Figure (10.5) The number of stimuli is 1 pair and the time for maps is $t = 100T^*$. The NN distance distribution for arbitrary pinwheel charges of maps for the distance of Gaussian stimuli as 0.1 (a). The NN distance distribution for opposite pinwheel charges of maps for the distance of Gaussian stimuli as 0.1 (b). The NN distance distribution for same pinwheel charges of maps for the distance of Gaussian stimuli as 0.1 (c). The NN distance distribution for arbitrary pinwheel charges of maps for the distance of Gaussian stimuli as 0.3 (d). The NN distance distribution for opposite pinwheel charges of maps for the distance of Gaussian stimuli as 0.3 (e). The NN distance distribution for same pinwheel charges of maps for the distance of Gaussian stimuli as 0.3 (f). The NN distance distribution for arbitrary pinwheel charges of maps for the distance of Gaussian stimuli as 0.5 (g). The NN distance distribution for opposite pinwheel charges of maps for the distance of Gaussian stimuli as 0.5 (h). The NN distance distribution for same pinwheel charges of maps for the distance of Gaussian stimuli as 0.5 (i).

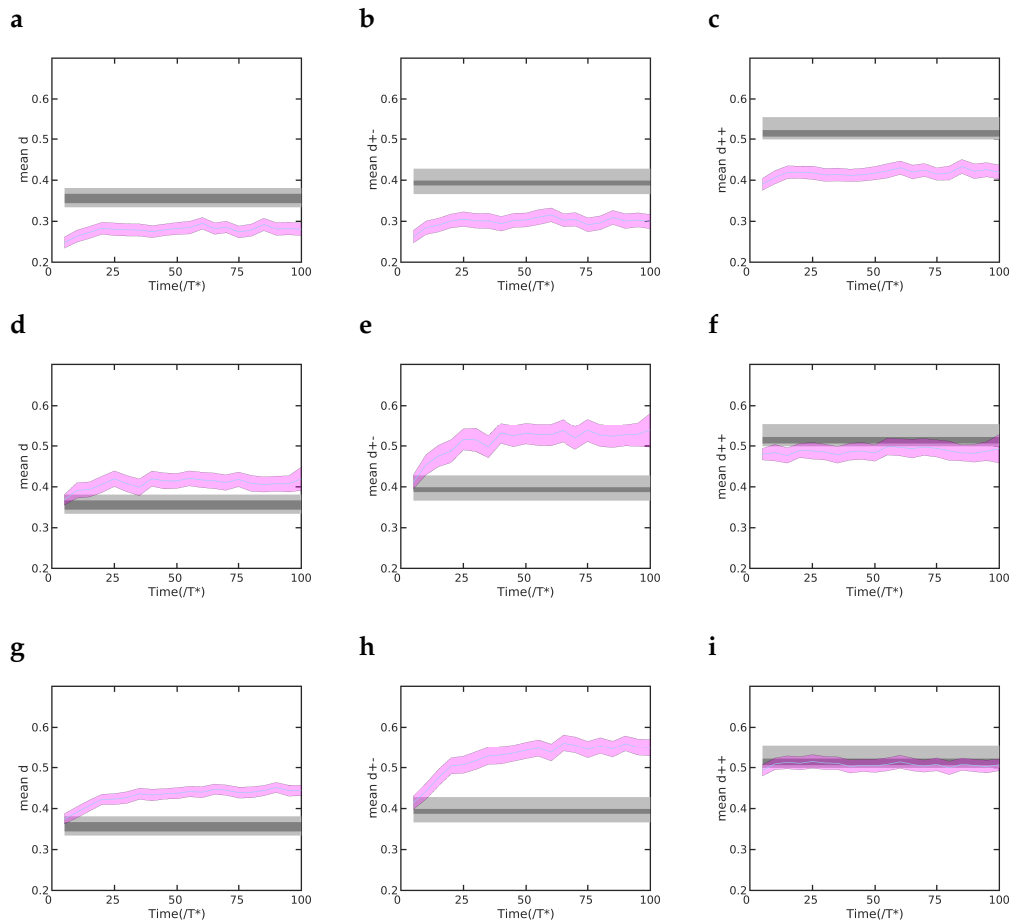


Figure (10.6) The number of stimuli is 1 pair. The mean NN distance for arbitrary pinwheel charges of maps for the distance as 0.1 (a). The mean NN distance for opposite pinwheel charges of maps for the distance as 0.1 (b). The mean NN distance for same pinwheel charges of maps for the distance as 0.1 (c). The mean NN distance for arbitrary pinwheel charges of maps for the distance of Gaussian stimuli as 0.3 (d). The mean NN distance for opposite pinwheel charges of maps for the distance of Gaussian stimuli as 0.3 (e). The mean NN distance for same pinwheel charges of maps for the distance of Gaussian stimuli as 0.3 (f). The mean NN distance for arbitrary pinwheel charges of maps for the distance of Gaussian stimuli as 0.5 (g). The mean NN distance for opposite pinwheel charges of maps for the distance of Gaussian stimuli as 0.5 (h). The mean NN distance for same pinwheel charges of maps for the distance of Gaussian stimuli as 0.5 (i).

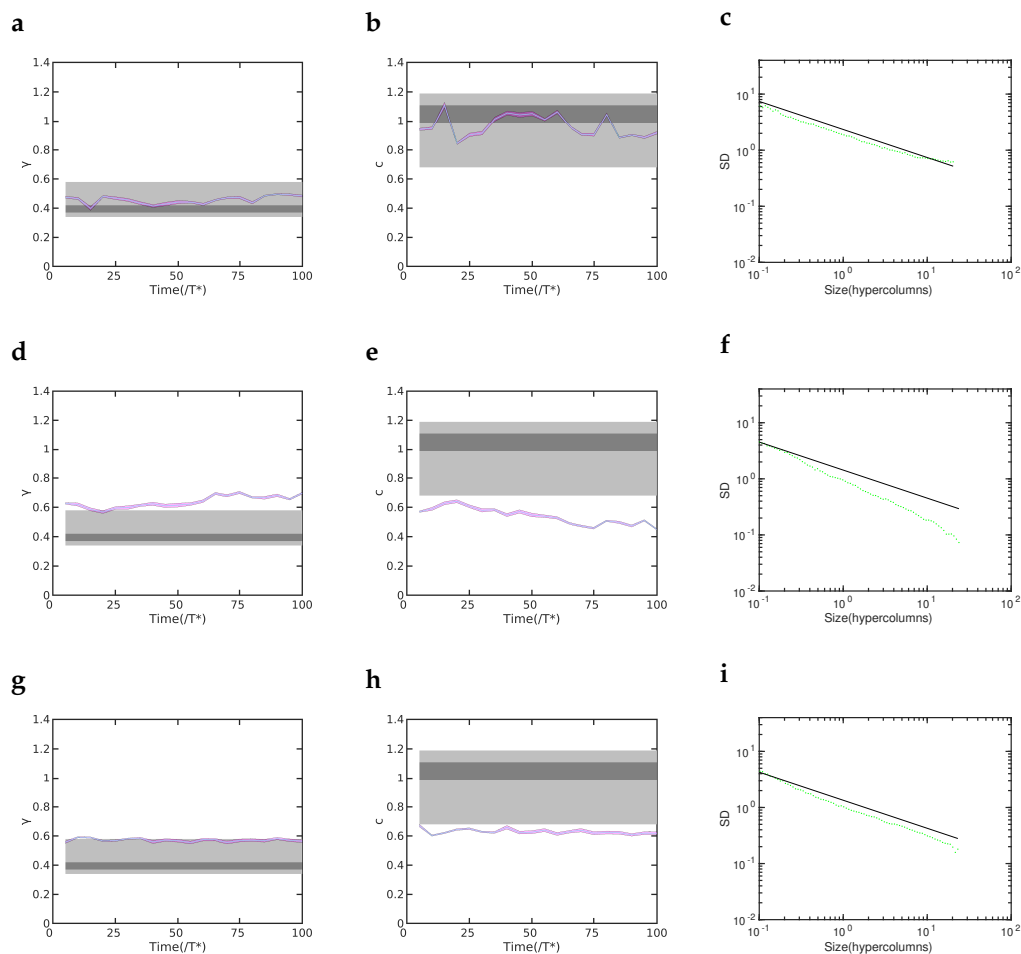


Figure (10.7) The number of stimuli is 1 pair. r for the distance of Gaussian stimuli as 0.1 (a). c for the distance of Gaussian stimuli as 0.1 (b). SD for the distance of Gaussian stimuli as 0.1 (c). r for the distance of Gaussian stimuli as 0.3 (d). c for the distance of Gaussian stimuli as 0.3 (e). SD for the distance of Gaussian stimuli as 0.3 (f). r the distance of Gaussian stimuli as 0.5 (g). c for the distance of Gaussian stimuli as 0.5 (h). SD for the distance of Gaussian stimuli as 0.5 (i).

10.3.2 Pinwheel statistics for area size 1.5×1.5 and 2 pairs of stimuli

Now we consider using 2 pairs of parallel Gaussian stimuli and area size as 1.5×1.5 to simulate the map development. When the distance of Gaussian patterns is 0.1, the average pinwheel density of maps firstly decreases and then fluctuate around the boundary of the experiment scope. The confidence interval is partly located in the experimental observation area. When the distance of two Gaussian stimuli is 0.3, the average pinwheel density drops gradually from about 4 to below 3 and the confidence interval leaves the experimental observation area during the time course. For the distance of two Gaussian as 0.5, the average pinwheel density falls to around 2 during the time evolution and the confidence interval drops to be outside of the experimental observation area. See Figure 10.8.

We choose $t = 100T^*$ and plot the nearest neighbor distance distribution of pinwheels and the fitting function curves for the second category (Figure 10.9). When

the distance of 2 Gaussian patterns is 0.1, the NN distance distribution of pinwheels without considering pinwheel charge deviates from the fitting function. The NN distance distribution of pinwheels with the same charge centers around 0.5 and the given function doesn't fit to the distribution. The NN distance distribution of pinwheels with the opposite charge also centers around 0.5 and doesn't fitted by the function. When the distance of 2 Gaussian is 0.3, the NN distance distribution of pinwheels without considering pinwheel charge centers around 0.45 and deviates from the fitting curve. The NN distance distribution of pinwheels with the same charge centers around 0.5 and the function doesn't fit to the distribution. The NN distance distribution of pinwheels with the opposite charge centers around 0.6 and the fitting function significantly deviate from it. As for the distance of 2 input patterns is 0.5, the NN distance distribution of pinwheels without considering pinwheel charge centers around 0.5 and is not close to the fitting function. The NN distance distribution of pinwheels with the same charge centers around 0.5 and doesn't fit to the function. The NN distance distribution of pinwheels with the opposite charge highly deviates from the fitting function.

Then we do the analysis of nearest neighbor distance distribution of pinwheels for this category. Firstly we analyze mean NN distances as functions of time (Figure 10.10). When the distance of 2 Gaussian is 0.1, both of confidence intervals of the mean NN distances without considering the charge of pinwheels and the mean NN distances for the opposite charge of pinwheels from the beginning of the period for observation leave the experimental observation area and to the end of the period they travel near the border of the experimental observation area. The confidence interval of the mean NN distances for the same charge of pinwheels stays near the boundary of the experimental observation area during the time course. When the distance of 2 Gaussian is 0.3, both of confidence intervals of the mean NN distance without considering the charge of pinwheels and the mean NN distance for the opposite charge of pinwheels firstly cross the experimental observation area and then stay outside of the area during the time evolution. The confidence interval of the mean NN distance for the same charge of pinwheels keep close to boundary of the experimental observation area. For the distance of 2 patterns is 0.5, both of the confidence intervals of the mean NN distance without considering the charge of pinwheels and the mean NN distance for the opposite charge of pinwheels grow from the inside of the experimental observation area and then stay in the outside of the area during the time course. The confidence interval of the mean NN distance for the same charge of pinwheels is basically located below the experimental observation area during the time evolution and intersects with the border of the area.

In the second category, we also fit the empirically observe power law, to the standard deviation of pinwheel density estimate in randomly selected circular regions of size A (Figure 10.11). Besides, we will show the variability exponent r and the variability constant c . When the distance of 2 Gaussian stimuli is 0.1, the confidence interval of the the variability exponent r is located in the experimental observation area but not in the common design area, and the confidence interval of the variability constant c firstly goes around the boundary of the experimental observation area for some time scales and then enters the inside of the area. Then we calculate the standard deviation of pinwheel densities as a function of the area A of randomly selected subregions of the iso-orientation domain layout. The black line is the standard deviation for 2 dimensional Poisson process of pinwheel density π . The pinwheel density variability is not far but still deviates from standard deviation of a 2 dimensional Poisson process of pinwheel density π . We show for example the case of $t = 100T^*$. For the distance of 2 Gaussian as 0.3, the confidence interval of the

variability exponent r firstly is located in the experiment observation area but then gradually leaves the area and the confidence interval of the variability constant c drops to below the area during the time course. Then we plot the pinwheel density variability deviates from standard deviation of a 2 dimensional Poisson process of pinwheel density π . We show an example of the case of $t = 100T^*$. For the distance of 2 Gaussian stimuli as 0.5, the confidence interval of the variability exponent r fluctuates around the border of the experimental observation area and the confidence interval of the variability constant c drops to below the area for the time course. Then we analyze the the pinwheel density variability deviates from standard deviation of a 2 dimensional Poisson process of pinwheel density π . An example of the case for $t = 100T^*$ is shown.

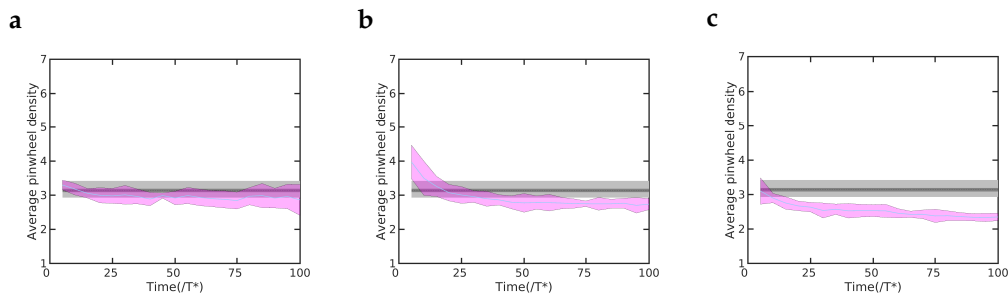


Figure (10.8) The number of stimuli is 2 pair. The average pinwheel density of maps for the distance of Gaussian stimuli as 0.1 (a). The average pinwheel density of maps for the distance of Gaussian stimuli as 0.3 (b). The average pinwheel density of maps for the distance of Gaussian stimuli as 0.5 (c).

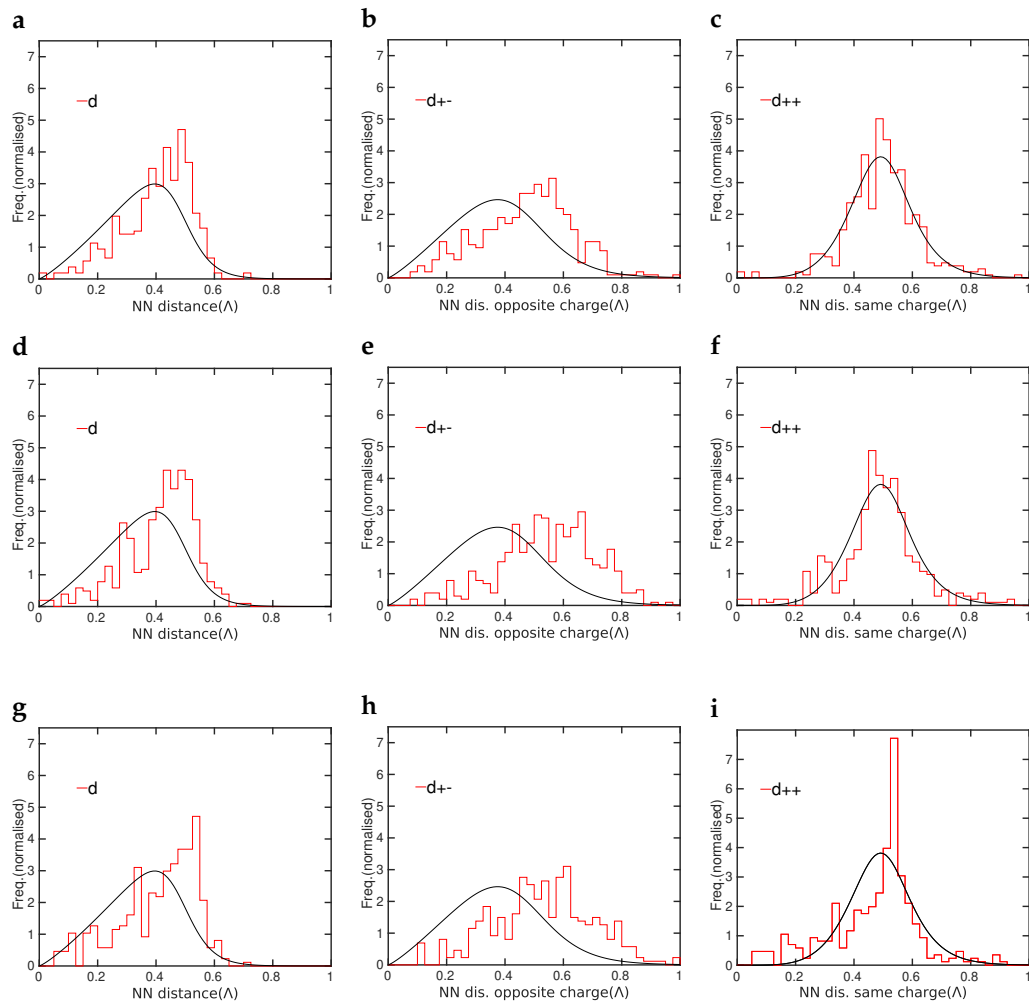


Figure (10.9) The number of stimuli is 2 pair and the time for maps is $t = 100T^*$. The NN distance distribution for arbitrary pinwheel charges of maps for the distance of Gaussian stimuli as 0.1 (a). The NN distance distribution for opposite pinwheel charges of maps for the distance of Gaussian stimuli as 0.1 (b). The NN distance distribution for same pinwheel charges of maps for the distance of Gaussian stimuli as 0.1 (c). The NN distance distribution for arbitrary pinwheel charges of maps for the distance of Gaussian stimuli as 0.3 (d). The NN distance distribution for opposite pinwheel charges of maps for the distance of Gaussian stimuli as 0.3 (e). The NN distance distribution for same pinwheel charges of maps for the distance of Gaussian stimuli as 0.3 (f). The NN distance distribution for arbitrary pinwheel charges of maps for the distance of Gaussian stimuli as 0.5 (g). The NN distance distribution for opposite pinwheel charges of maps for the distance of Gaussian stimuli as 0.5 (h). The NN distance distribution for same pinwheel charges of maps for the distance of Gaussian stimuli as 0.5 (i).

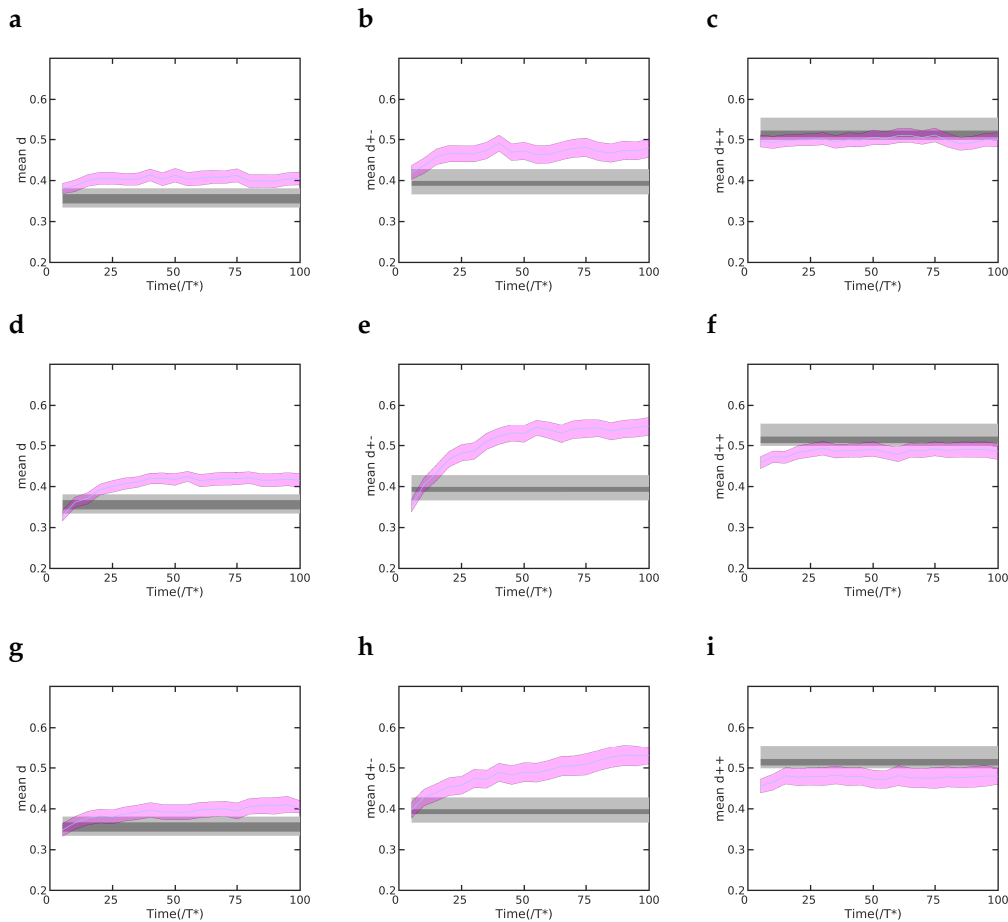


Figure (10.10) The number of stimuli is 2 pair. The mean NN distance for arbitrary pinwheel charges of maps for the distance as 0.1 (a). The mean NN distance for opposite pinwheel charges of maps for the distance as 0.1 (b). The mean NN distance for same pinwheel charges of maps for the distance as 0.1 (c). The mean NN distance for arbitrary pinwheel charges of maps for the distance of Gaussian stimuli as 0.3 (d). The mean NN distance for opposite pinwheel charges of maps for the distance of Gaussian stimuli as 0.3 (e). The mean NN distance for same pinwheel charges of maps for the distance of Gaussian stimuli as 0.3 (f). The mean NN distance for arbitrary pinwheel charges of maps for the distance of Gaussian stimuli as 0.5 (g). The mean NN distance for opposite pinwheel charges of maps for the distance of Gaussian stimuli as 0.5 (h). The mean NN distance for same pinwheel charges of maps for the distance of Gaussian stimuli as 0.5 (i).

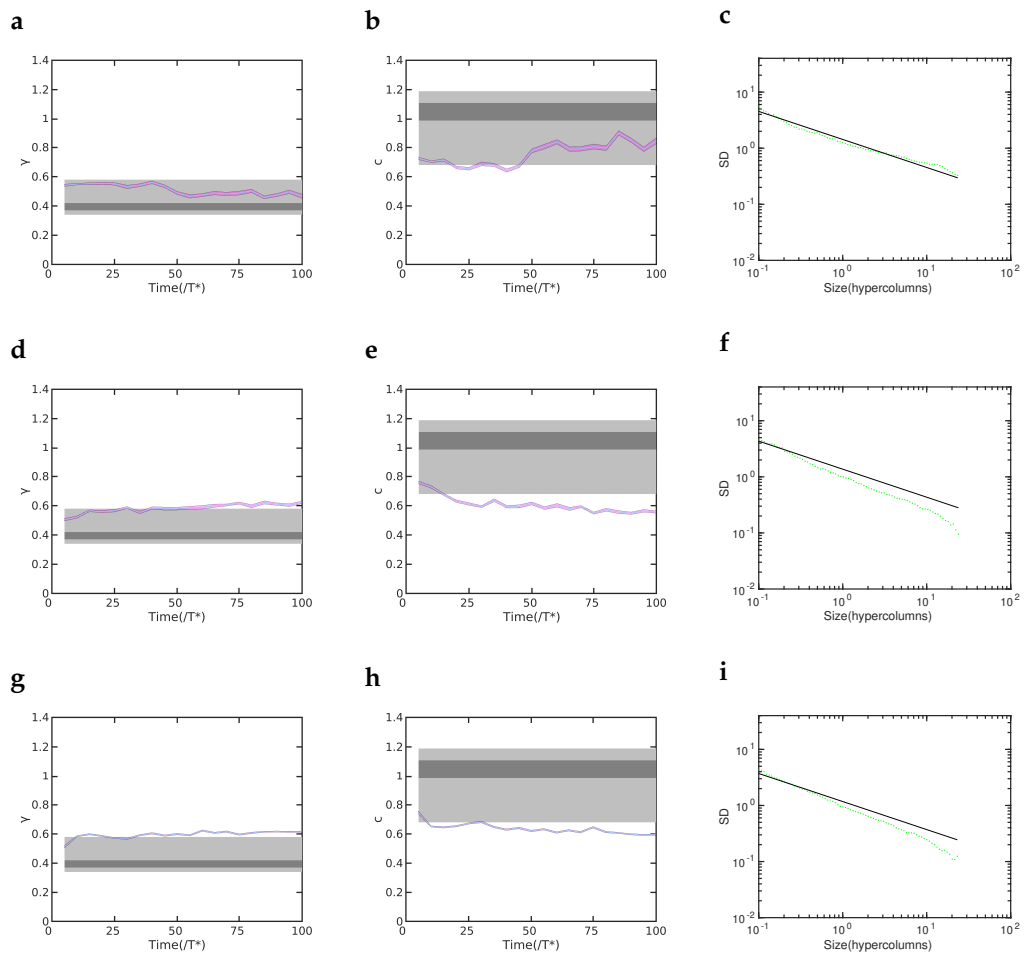


Figure (10.11) The number of stimuli is $2 \text{ pair}.r$ for the distance of Gaussian stimuli as 0.1 (a). c for the distance of Gaussian stimuli as 0.1 (b). SD for the distance of Gaussian stimuli as 0.1 (c). r for the distance of Gaussian stimuli as 0.3 (d). c for the distance of Gaussian stimuli as 0.3 (e). SD for the distance of Gaussian stimuli as 0.3 (f). r the distance of Gaussian stimuli as 0.5 (g). c for the distance of Gaussian stimuli as 0.5 (h). SD for the distance of Gaussian stimuli as 0.5 (i).

Chapter 11

Modeling the long range interaction in the visual cortex

11.1 Introduction

In previous investigations, long range interactions appear as the key element for the stabilization of orientation preference maps with "common design" features. In order to more closely mimic the long range interactions in the visual cortex, we introduced two types of effective inhibitory connections to the Topographica model: "short" connections and "long connections". The "short connections" drive the basic structure formation of patterns with one dominant wavelength. The "long connections" are responsible for the long range cortical competition in the model. Both of them are thus effectively inhibitory and exhibit Gaussian envelope functions. Here we explore an example for a choice of parameters the size of Gaussians 0.15 and 0.8 for "the short connection" and "the long connection". Where 0.8 is more than double of a typical wavelength of the modeling cortex which is about 0.25, a condition predicted by abstract order parameter models. We examine map development in simulations with periodical boundary conditions.

11.2 The observation for maps developed for the long range interaction in the model

First we show three snapshots at times $t = 1T^*$, $t = 50T^*$ and $t = 100T^*$ to represent one example of the development process. The map layout is not crystal-like at all times. See Figure 11.1.

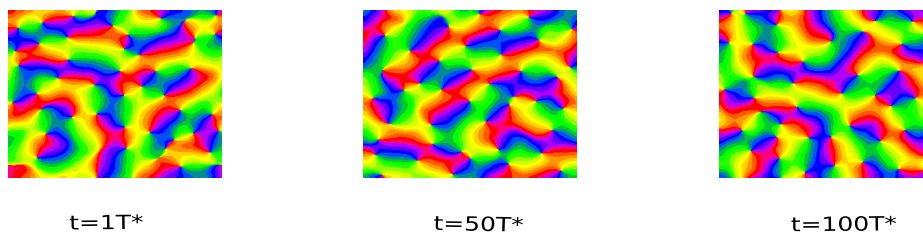


Figure (11.1) An example of map development with the effect of modeling long range interaction.

11.3 The statistical analysis of the process of the map development for the modeling of long range interaction

Now we perform statistical analysis to characterize the process of the map development with the modeling long range interaction.

Regarding to the mean pinwheel density (Figure 11.2.), it gradually leaves the experimental observation area during the time course, although the confidence interval still have some parts in the area. From about $t = 60T^*$, the average pinwheel density decreases to below 3. Then we analyze nearest neighbor (NN) distance distribution of pinwheels. See Figure 11.3. Firstly we calculate mean NN distances as functions of time. For the mean NN distance without considering the charge of pinwheels, its confidence interval stays outside of the experimental observation area. As for the mean NN distance of pinwheels with the same charge, the confidence interval overlaps the common design area. For the mean NN distance of pinwheels with the opposite charge, the confidence interval gradually leaves the experimental observation region. Secondly we choose $t = 100T^*$ and plot the NN distance distribution of pinwheels and the fitting function curves. All of the distributions deviate from the fitting functions. The NN distance distribution without considering the charge of pinwheels have the shape of some rectangle bars and doesn't fit to the function. The NN distance distribution for pinwheels with the same charge centers around 0.45 and can't fitted by the function curve. The NN distance distribution for pinwheels with the opposite charge also centers about 0.45 and deviates from the fitting curve.

Besides we fit the empirically observe power law, to the standard deviation of pinwheel density estimate in randomly selected circular regions of size A . We will also describe the variability exponent r and the variability constant c . As shown in the figures, the confidence interval of the variability exponent r is located at the experimental observation area but not at the common design area. After about $5T^*$ the confidence interval of the variability constant c falls to below the experimental observation area and basically stays outside of the area but at a few time points, it is close to the border of the area. Then we describe the standard deviation of pinwheel densities as a function of the area A of randomly selected subregions of the iso-orientation domain layout. As shown in the figure the black line is the standard deviation for 2 dimensional Poisson process of pinwheel density π . The pinwheel density variability is close but still deviates from standard deviation of a 2 dimensional Poisson process of pinwheel density π . We show for example the case for $t = 100T^*$.

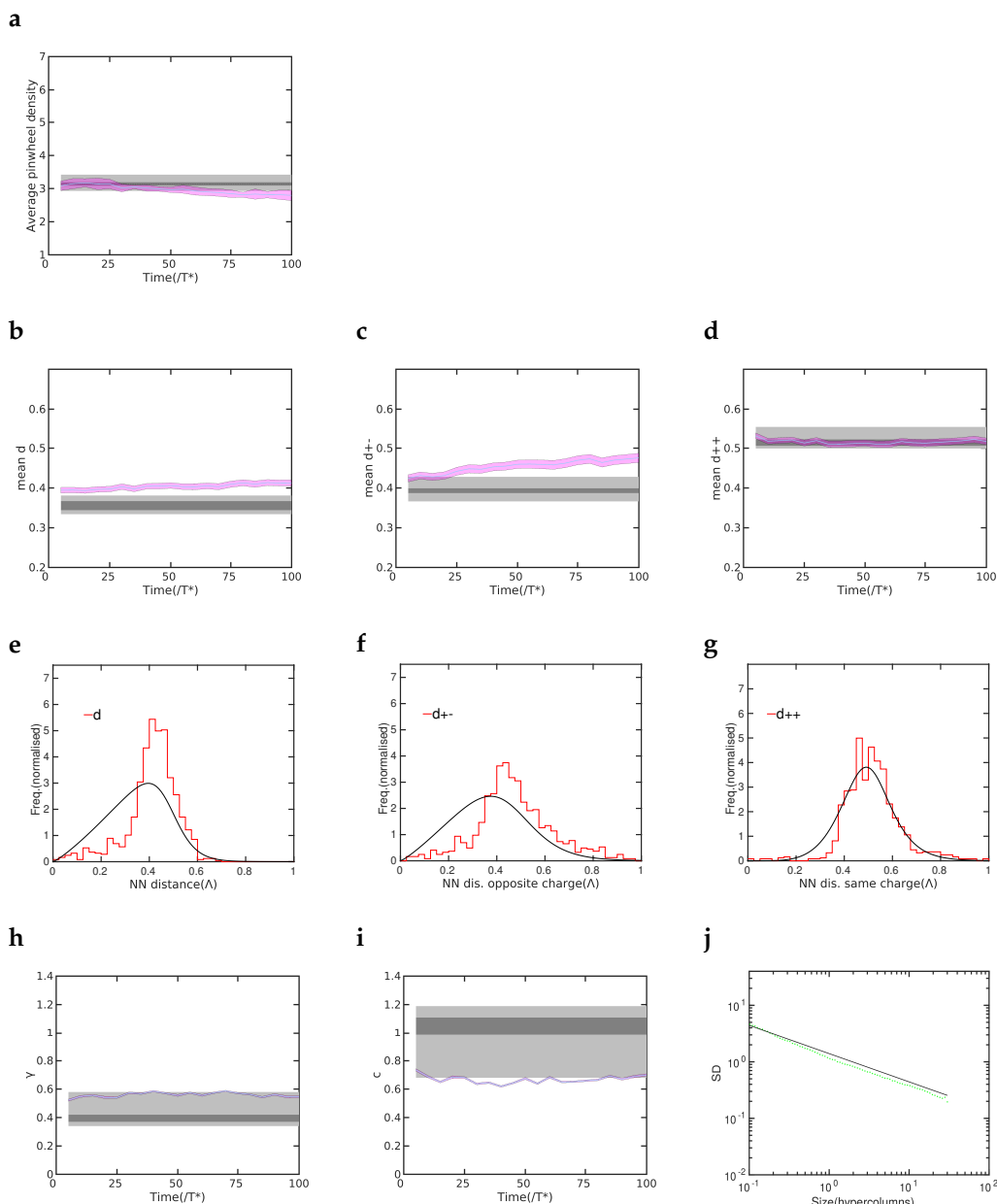


Figure (11.2) The pinwheel statistics for maps developed for the long range interaction model. The mean pinwheel density of maps during the time course (a).The mean NN distance for arbitrary pinwheel charges for the maps (b).The mean NN distance for same pinwheel charges for the maps (c).The mean NN distance for opposite pinwheel charges for the maps (d).The NN distance distribution for arbitrary pinwheel charges for the maps when $t = 100T^*$ (e). The NN distance distribution for same pinwheel charges for the maps when $t = 100T^*$ (f). The NN distance distribution for opposite pinwheel charges for the maps when $t = 100T^*$ (g). The variability exponent r for the maps (h).The variability constant c for the maps (i).SD for the maps (j).

Chapter 12

The impact of different numbers of Gaussian stimuli for map development

12.1 Introduction

In this chapter we analyze maps with 1,2,4,8,16,32 Gaussian stimuli, respectively and show they have varied pinwheel statistics. By the analysis of simulation results, we find that using different numbers of Gaussian stimuli in the Topographical model, map development is substantially altered. For example, when the number of Gaussian stimuli is 32, we obtain the maps shown in the figure 12.1. Compared to patterns developed by using 4 stimuli in the size of area as $1.5 * 1.5$, the maps with 32 stimuli appear to have some short curved stripes which are newly observed (Figure 12.1).

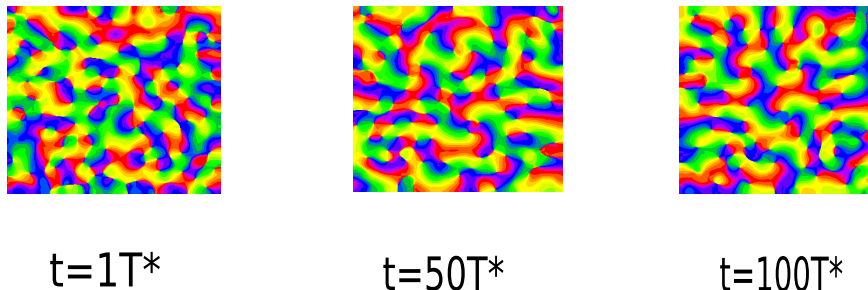


Figure (12.1) An example of map development with 32 Gaussian stimuli.

12.2 Map development using 2 Gaussian stimuli

Here we will show the analysis results for 2 Gaussian inputs. Now we analyzed the statistics of pinwheels for maps developed by only 2 Gaussian stimuli in the area size as $1.5 * 1.5$. The aspect ratio of the Gaussian pattern is 5.1. Firstly we show 3 snapshots of example maps and from the observation, there is no strong boundary effect for the maps which is seen in maps with 4 Gaussian stimuli simulated in the area $1.5 * 1.5$. See Figure 12.2.

Then we perform the analysis of pinwheel densities(Figure 12.3). The mean value of pinwheel densities drops from about 3.4 at the beginning and then grows to be in the common design area. From about $t = 50T^*$, the average pinwheel density is basically located at the common design region. The confidence interval of pinwheel densities have main parts in the experimental observation area during the time course.

We analyze nearest neighbor (NN) distance distribution of pinwheels. See Figure 12.4. We calculate mean NN distances as functions of time. For the confidence interval of mean NN distance without considering the charge of pinwheels, it is close to the upper border of the experimental observation area. As for the mean NN distance with the same charge of pinwheels, the confidence interval is also close to and fluctuates around the lower boundary of the experimental observation area. The confidence interval of the mean NN distance with the opposite charge of pinwheels is near the border of the experimental observation area and at some time points is located inside of the area. Then we choose $t = 150T^*$ and plot the NN distance distribution of pinwheels and the fitting function curves. Although all of the distributions deviate from the fitting functions, but they are close to the fitting curves, respectively.

In addition we fit the empirically observe power law, to the standard deviation of pinwheel density estimate in randomly selected circular regions of size A . We will analyze the variability exponent r and the variability constant c . The confidence interval of the variability exponent r is beside the upper boundary of the experimental observation area and for some time points is located at inside of the area. The confidence interval of the variability constant c is below and at outside of but is close to the experimental observation area. Then we plot for example $t = 150T^*$ the standard deviation of pinwheel densities as a function of the area A of randomly selected sub-regions of the iso-orientation domain layout. The figure shows the black line is the standard deviation for 2 dimensional Poisson process of pinwheel density π . The pinwheel density variability is close but still deviates from standard deviation of a 2 dimensional Poisson process of pinwheel density π .

So far the pinwheel statistics for using only 2 Gaussian in area $1.5 * 1.5$ are mostly close to the features of the common design among all the simulations we perform.

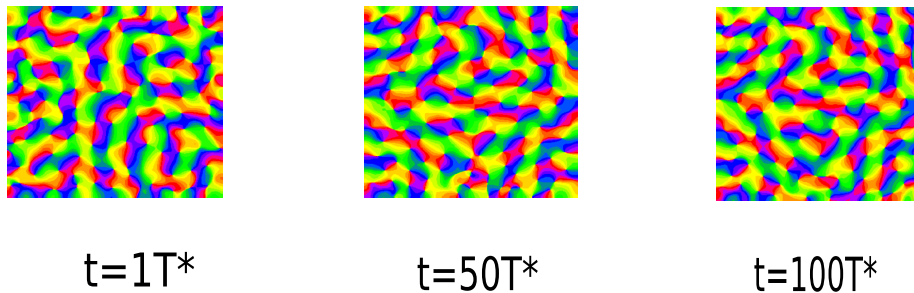


Figure (12.2) An example of map development with 2 Gaussian stimuli.

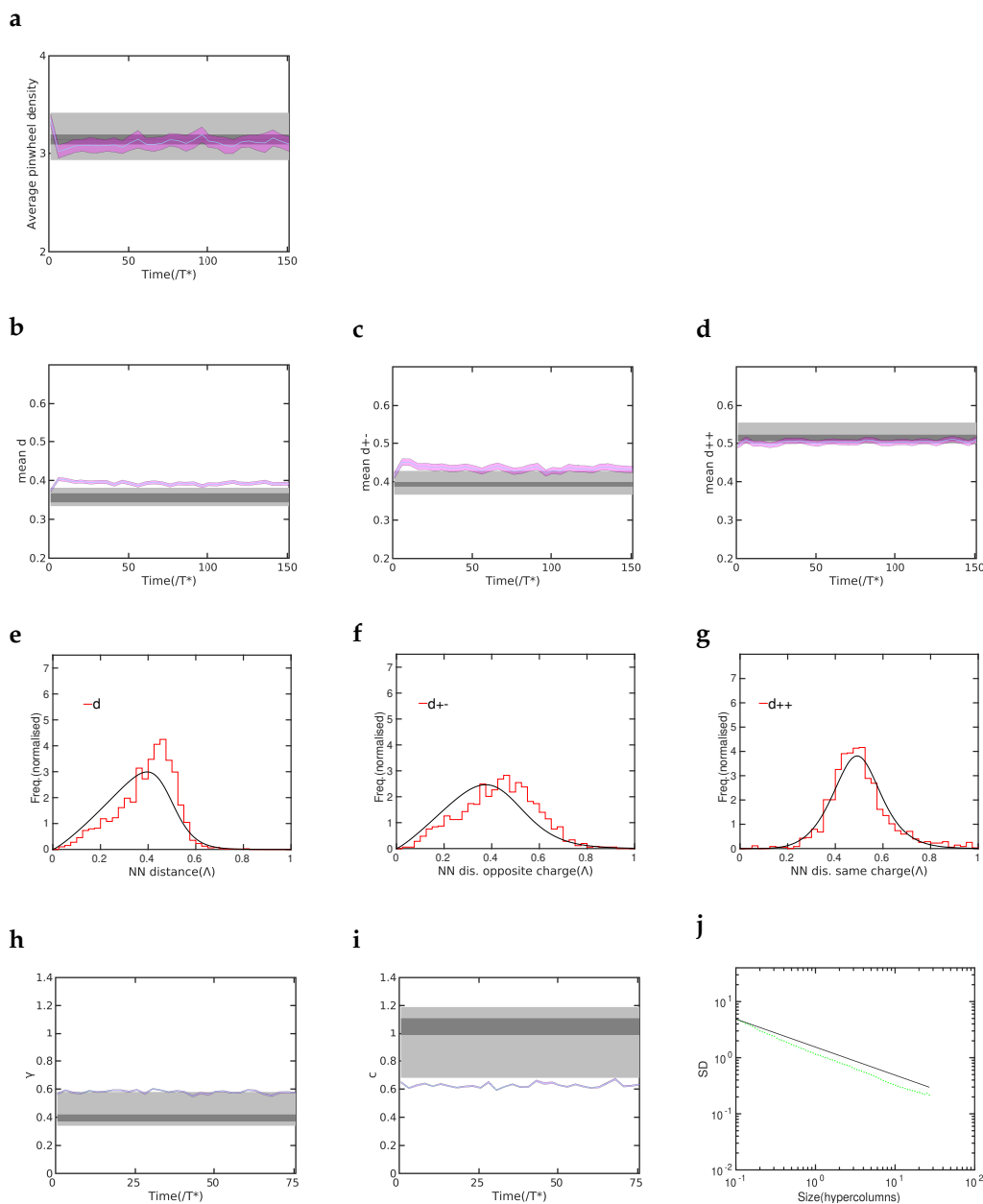


Figure (12.3) The statistics of pinwheel layouts for maps developed by using only 2 Gaussian. The mean pinwheel density of maps during the time course (a). The mean NN distance for arbitrary pinwheel charges (b). The mean NN distance for same pinwheel charges (c). The mean NN distance for opposite pinwheel charges (d). The NN distance distribution for arbitrary pinwheel charges for the maps when $t = 150T^*$ (e). The NN distance distribution for same pinwheel charges for the maps when $t = 150T^*$ (f). The NN distance distribution for opposite pinwheel charges for the maps when $t = 150T^*$ (g). The variability exponent r for the maps (h). The variability constant c for the maps (i). SD for the maps (j).

Chapter 13

Discussion and Conclusion

Our study explored pinwheel dynamical phenomena in the framework of the Topographica model and assessed parameter dependencies of model behaviour and model predictions for visual cortex development. In Chapter 3 I examined the van Hemmen model to describe the mechanism of the formation of receptive fields in the Topographica model and the current results show that the framework of van Hemmen model is probably unsuitable to achieve this goal. In subsequent chapters I used extensive numerical simulations to characterize the behaviour of the Topographica model on long biologically important time scales. Chapter 4 examines with the same conditions as used originally in the Topographica model, the dynamics of OPM development on long-term time scales and during the process of pinwheel creation and annihilation; In addition, pinwheel crystals are discovered to form in the simulations. Chapter 5 focuses on the parameter regime of the excitatory range of the cortex in the model by examining the change of pinwheel layouts during map development. Chapter 6 turns to study the model with periodic boundary conditions which are newly implemented and gives the dynamical description of cortical patterns under this condition. Chapter 7 analyzes the process of OPM development for different system sizes of the model and finds that in larger size cortical areas (for example if the area is $3 * 3$) that the pinwheel crystallization process is more apparent and clearly expressed. Chapter 8 compares pinwheel statistics generated by using different learning rates in the model. Chapter 9 performs an analysis for the parameter of the inhibitory interaction in the model and confirms that OPMs produced by using the previously chosen parameters values fail to match observed OPMs for the common design. Chapter 10 studies whether using correlated stimuli consisting of 1 or 2 pairs of 2 parallel Gaussian stimuli could produce OPMs which could have pinwheel layouts conforming the features of the common design. Chapter 11 builds a model with a new type of long range cortical interactions and examines the pinwheel statistics produced under this condition. The results show the model with the long-range interaction in the visual cortex and periodic boundary conditions is not able to generate features for the common design. Chapter 12 examines the impact of different numbers of input patterns for OPM development in the model and discovers the maps which have similar pinwheel statistics to the common design are observed for the first time in a high dimensional biologically detailed model.

13.1 Pinwheel crystallization in the developmental model

Now we turn to discuss the phenomena of pinwheel crystallization emerged in the OPM development of the model. Pinwheel crystallization was for the first time observed during the process of the map development in a detailed input-driven model. Under various conditions including using 2 or 4 Gaussian stimuli, and cortical areas of size $1 * 1$ or $1.5 * 1.5$, a boundary effect is observed for map formation, with the

maps dominated by stripes perpendicular to the boundaries. There are long stripes and crystals formed and the long stripes consist of crystals connected to each other. The patterns of stripes and crystals are affected by pinwheel generation and disappearance near the borders. Pinwheels which are generated near the boundary move into the central zone of the simulation area and collide with other pinwheels, so that pinwheel annihilation and creation happens. If the size of the cortical area is larger e.g 3×3 , OPMs become more regular than the maps for smaller sizes and clear crystals can be observed during the map development. The shapes of these crystals are similar to rhomboid pinwheel crystals observed in abstract models previously and the stripes near borders are additionally produced.

It is important to note that pinwheel crystallization is a dynamical process that takes long time in map development. Whether it occurs in real brains is thus an interesting question to discuss. Currently, some experimental evidences indicate it is unlikely to happen in animal brains. At least five species have been discovered to share the common design for their cortical architectures and do not appear to have pinwheel crystallization process during their early and late stages of map development ((C.L.A.Ho et al., 2021; W.Keil et al., 2012; M.Kaschube et al., 2010a; M.Schottdorf et al., 2015b)). So it is most likely that pinwheel crystallization is a behavior only exhibited by theoretical and simulation models and a process characteristic of developmental processes substantially different from the biological system.

Pinwheel crystals have been previously found in several abstract as well as in synaptic plasticity based models. Von der Malsburg was the first to predict OPMs by a synaptically based self-organization model in 1973 and this model displays hexagonal patterns in the OPMs. Von der Malsburg in the simulations used a hexagonal grid of cells that may affect the formation of hexagonal patterns. Hexagonal layouts of maps are also demonstrated by L.Reichl et al. (2012) which studies coordinated optimization models of orientation preference, ocular dominance, spatial frequency or direction preference. Strikingly, for solutions as optima of this model, pinwheels are also arranged on regular periodic lattices such as rhombic pinwheel crystals (rPWCs), which are similar to the shape of crystals found in our research. rPWCs can also be found in some other studies (P.J.Thomas and J.D.Cowan, 2021; M.Schnabel, M.Kaschube, and F.Wolf, 2008; W.Keil and F.Wolf, 2011). For example, W.Keil and F.Wolf (2011) utilizes an amplitude equation approach which enables to analytically compute optima of the elastic net model for visual cortical map layout and determines a class of solutions which are rPWCs. In this study they also find other solutions for hexagonal pinwheel crystallization. In Schnabel et al.(2008)'s work, they show that a generalized Swift-Hohenberg model of visual cortical development under the Euclidean symmetry has the solution of rPWCs which are similar to the crystals in the Bednar model.

13.2 Conclusion and outlook

We examined different conditions and parameter regimes for OPM development in the Topographica model and characterize map layouts on long time scales. Our results for the first time provide a comprehensive characterization of the temporal reorganization of orientation maps across all biologically relevant timescales, from the first emergence of orientation selective cells to the final convergence of the entire circuit architecture. All of these results confirm that - as expected for large aspect ratio dynamical systems - visual cortical circuit development is predicted to exhibit

a hierarchy of time scales. In addition, they provide strong evidence that the experimentally observed universal common design of orientation pinwheels in visual cortex provides a highly selective filter to identify models that quantitatively correctly reproduce cortical functional organization. My comprehensive scan of parameter variations and model modification demonstrate that models that quantitatively correctly reproduce cortical functional organization are very rare. Among these conditions pinwheel layouts under conditions explained in Chapter 12 show statistical characteristics mostly closely matching the features of the common design. Future work should further explore the regime around these conditions to identify conditions that can obtain pinwheel statistics of OPMs and reproduce the biologically invariant common design.

Bibliography

- A.Borst, V.L.Flanagin, and H.Sompolinsky (2005). "Adaptation without parameter change: Dynamic gain control in motion detection". In: *Proc. Natl. Acad. Sci. USA* 102, pp. 6172–6176.
- A.Grinvald et al. (1986). "Functional architecture of cortex revealed by optical imaging of intrinsic signals". In: *Nature* 324, pp. 361–364.
- A.Grinvald et al. (1988). "Optical imaging of neuronal activity". In: *Physiological Reviews* 68, pp. 1285–1366.
- A.I.Weber, K.Krishnamurthy, and A.L.Fairhall (2019). "Coding principles in adaptation". In: *Current Biology* 5, pp. 427–449.
- B.A.Wandell and S.M.Smirnakis (2009). "Plasticity and stability of visual field maps in adult primary visual cortex". In: *Nature Review Neuroscience* 10, pp. 873–884.
- B.G.Cragg (1975). "the development of synapses in the visual system of the cat". In: *J Comp Neurol* 160, pp. 147–166.
- B.Godde et al. (2002). "Plasticity of orientation preference maps in the visual cortex of adult cats". In: *PNAS* 99, pp. 6352–6357.
- B.M.Hooks and C.Chen (2006). "Distinct roles for spontaneous and visual activity in remodeling of the retinogeniculate synapse". In: *Neuron* 52, pp. 281–291.
- (2007). "Critical Periods in the Visual System: Changing Views for a Model of Experience-Dependent Plasticity". In: *Neuron* 56, pp. 312–326.
- C.D.Gilbert and T.N.Wiesel (1979). "Morphology and intracortical projections of functionally characterised neurones in the cat visual cortex". In: *J.Neurosci.* 280, pp. 120–125.
- (1983). "Clustered intrinsic connections in cat visual cortex". In: *J.Neurosci.* 3, pp. 1116–1133.
- C.D.Meliza and D.Yang (2006). "Receptive-field modification in rat visual cortex induced by paired visual stimulation and single-cell spiking". In: *Neuron* 49(2), pp. 183–189.
- C.Gilbert and T.N.Wiesel (1989). "Columnar specificity of intrinsic horizontal and corticocortical connections in cat". In: *J.Neurosci.* 9, pp. 2432–2442.
- C.L.A.Ho et al. (2020). "Orientation Preference Maps in Microcebus murinus Reveal Size-Invariant Design Principles in Primate Visual Cortex". In: *Current Biology* 31, pp. 733–741.
- (2021). "Orientation Preference Maps in Microcebus murinus Reveal Size-Invariant Design Principles in Primate Visual Cortex". In: *Curr.Biol.* 31, pp. 733–741.
- D.E.Hannula, D.J.Simons, and N.J.Cohen (2005). "Imaging implicit perception: promise and pitfalls". In: *Nature Rev.Neurosci.* 6, pp. 247–255.
- D.H.Hubel and T.N.Wiesel (1959). "Receptive fields of single neurones in the cat's striate cortex". In: *J Physiol.* 148, pp. 574–591.
- (1962). "Receptive fields, binocular interaction and functional architecture in the cat's visual cortex". In: *J Physiol* 160, pp. 106–154.
- (1963a). "Receptive fields of cells in striate cortex of very young visually inexperienced kittens". In: *J Neurophysiol.* 26, pp. 994–1002.

- (1963b). "Shape and arrangement of columns in cat's striate cortex". In: *J Physiol* 165, pp. 559–568.
- (1977). "Ferrier lecture - Functional architecture of macaque monkey visual cortex". In: *Proc.R.Soc.Lond.B* 198, pp. 1–59.
- D.O.Hebb (1949). "The Organization of Behaviour". In: (New York:Wiley).
- E.Erwin, K.Obermayer, and K.Schulten (1995). "Models of orientation and ocular dominance columns in the visual cortex: a critical comparison". In: *Neural Comput.* 7, pp. 425–468.
- E.Kaplan, S.Marcus, and Y.T.So (1979). "Effects of dark adaptation on spatial and temporal properties of receptive fields in cat lateral geniculate nucleus". In: *J Physiol.* 294, pp. 561–580.
- F.Sengpiel, P.Stawinski, and T.Bonhoeffer (1999a). "Influence of experience on orientation maps in cat visual cortex". In: *Nature Neuroscience* 2, pp. 727–732.
- (1999b). "Influence of experience on orientation maps in cat visual cortex". In: *Nat Neurosci* 2, pp. 727–732.
- F.Wolf (2005). "Symmetry,multistability,and long-range interactions in brain development". In: *Phys.Rev.Lett.* 95, p. 208701.
- F.Wolf and T.Geisel (2003). "Universality in visual cortical pattern formation". In: *J.Physiol.(Paris)* 97, pp. 253–264.
- G.G.Blasdel and G.Salama (1986). "Voltage-sensitive dyes reveal a modular organization in monkey striate cortex". In: *Nature* 321, pp. 579–585.
- G.J.Goodhill (1993). "Topography and ocular dominance: a model exploring positive correlations". In: *Biol.Cybern.* 69, pp. 109–118.
- (2007). "Contributions of theoretical modeling to the understanding of neural map development". In: *Neuron* 56, pp. 301–311.
- G.J.Goodhill and D.J.Willshaw (1990). "Application of the elastic net algorithm to the formation of ocular dominance stripes". In: *Network* 1, pp. 41–59.
- H.G.Barrow, A.Bray, and J.M.L.Budd (1996). "A self-organizing model of color blob formation". In: *Neural Comput.* 8, pp. 1427–1448.
- H.Kato, P.O.Bishop, and G.A.Orban (1978). "Hypercomplex and simple/complex cell classifications in cat striate cortex". In: *J Neurophysiol.* 41, pp. 1071–1095.
- H.Lütcke, D. J. Margolis, and F. Helmchen (2013). "Steady or changing?Long-term monitoring of neuronal population activity". In: *Trends in Neurosciences* 36, pp. 375–384.
- J.A.Bednar and R.Miikkulainen (2004). "Prenatal and postnatal development of laterally connected orientation maps". In: *Neurocomputing* 58-60, pp. 985–992.
- (2006). "Joint maps for orientation,eye,and direction preference in a self-organizing model of V1". In: *Neurocomputing* 69, pp. 1272–1276.
- J.A.Movshon, I.D.Thompson, and D.J.Tolhurst (1978). "Receptive field organization of complex cells in the cat's striate cortex". In: *J Physiol.* 283, pp. 79–99.
- J.B.Ackman and M.C.Crair (2014). "Role of emergent neural activity in visual map development". In: *Current Opinion in Neurobiology* 24, pp. 166–175.
- J.R.Kohn et al. (2021). "Flexible filtering by neural inputs supports motion computation across states and stimuli". In: *Current Biology* 31, R1523–R1525.
- J.S.Espinosa and M.P.Stryker (2012). "Development and Plasticity of the Primary Visual Cortex". In: *Neuron* 75, pp. 230–249.
- J.Sharma, A.Angelucci, and M.Sur (2000). "Induction of visual orientation modules in auditory cortex". In: *Nature* 404, pp. 841–847.
- J.Sirosh and R.Miikkulainen (1997). "Topographic receptive fieldsand patterned lateral interaction in a self-organizing model of the primary visual cortex". In: *Neural Comput.* 9, pp. 577–594.

- J.Stevens et al. (2013). "Mechanisms for Stable, Robust, and Adaptive Development of Orientation Maps in the Primary Visual Cortex". In: *J.Neurosci.* 33, pp. 15747–15766.
- J.T.Chang, D.Whitney, and D.Fitzpatrick (2020). "Experience-Dependent Reorganization Drives Development of a Binocularly Unified Cortical Representation of Orientation". In: *Neuron* 107, pp. 338–350.
- K.D.Miller (1994). "A model for the development of simple cell receptive fields and the ordered arrangement of orientation columns through the activity dependent competition between ON- and OFF-center inputs". In: *J.Neurosci.* 14, 409–441.
- Ko, Ho et al. (2011). "Functional specificity of local synaptic connections in neocortical networks". In: *Nature* 473, pp. 87–91.
- K.Obermayer, G.G.Blasdel, and K.Schulten (1992). "Statistical-mechanical analysis of self-organization and pattern formation during the development of visual maps". In: *Phys.Rev.A* 45, pp. 7568–7589.
- K.Obermayer, H.Ritter, and K.Schulten (1990). "A principle for the formation of the spatial structure of cortical feature maps". In: *Proc.Natl.Acad.Sci.USA* 87, 8345–8349.
- K.Ohki et al. (2005). "Functional imaging with cellular resolution reveals precise micro-architecture in visual cortex". In: *Nature* 433, pp. 597–603.
- K.Ohki et al. (2006a). "Highly ordered arrangement of single neurons in orientation pinwheels". In: *Nature* 442, pp. 925–928.
- (2006b). "Highly ordered arrangement of single neurons in orientation pinwheels". In: *Nature* 442, pp. 925–928.
- K.R.Jones, P.D.Spear, and L.Tong (1984). "Critical periods for effects of monocular deprivation: differences between striate and extrastriate cortex". In: *J.Neurosci.* 4, pp. 2543–2552.
- K.S.Rockland and J.S.Lund (1982). "Widespread periodic intrinsic connections in the treeshrew visual cortex". In: *Science* 215, pp. 1532–1534.
- L.C.Sincich and G.G.Blasdel (2001). "Oriented Axon Projections in Primary Visual Cortex of the Monkey". In: *J.Neurosci.* 21, pp. 4416–4428.
- L.E.White, D.M.Coppola, and D.Fitzpatrick (2001). "The contribution of sensory experience to the maturation of orientation selectivity in ferret visual cortex". In: *Nature* 411, pp. 1049–1052.
- L.Reichl et al. (2012). "Coordinated Optimization of Visual Cortical Maps (II) Numerical Studies". In: *PLoS Comput Biol* 8, e1002756.
- L.White and D.Fitzpatrick (2007). "Vision and cortical map development". In: *Neuron* 56, pp. 327–338.
- Malsburg, C.von der (1973). "Self-organization of orientation sensitive cells in the striate cortex". In: *Kybernetik* 14, pp. 85–100.
- Malsburg, C.von der and D.J.Willshaw (1976). "A mechanism for producing continuous neural mappings: ocularity dominance stripes and ordered retino-tectal projections". In: *Exp.Brain Res. (Suppl 1)*, pp. 463–469.
- (1977). "How to label nerve cells so that they can interconnect in an ordered fashion". In: *Proc.Natl.Acad.Sci.USA* 74, pp. 5176–5178.
- M.Callaway, E. and L.C.Katz (1990). "Emergence and Refinement of Clustered Horizontal Connections in Cat Striate Cortex". In: *J.Neurosci.* 10, pp. 1134–1153.
- M.C.Crair, D.C.Gillespie, and M.P.Stryker (1998a). "The role of visual experience in the development of columns in cat visual cortex". In: *Science* 279, pp. 566–570.
- (1998b). "The role of visual experience in the development of columns in cat visual cortex". In: *Science* 279, pp. 566–570.
- M.Kaschube et al. (2010a). "Universality in the Evolution of Orientation Columns in the Visual Cortex". In: *Science* 330, pp. 1113–1116.

- (2010b). “Universality in the Evolution of Orientation Columns in the Visual Cortex, Supporting Information”. In: *Science* 330, pp. 1113–1116.
- M. Riesenhuber et al. (1998). “Breaking rotational symmetry in a self-organizing map model for orientation map development”. In: *Neural Comput.* 10, pp. 717–730.
- M. S. Brainard and A. J. Doupe (2000). “Auditory feedback in learning and maintenance of vocal behaviour”. In: *Nature Rev. Neurosci.* 1, pp. 31–40.
- M. Schnabel, M. Kaschube, and F. Wolf (2008). “Pinwheel stability, pattern selection and the geometry of visual space”. In: *arXiv*.
- M. Schottdorf et al. (2015a). “Random Wiring, Ganglion Cell Mosaics, and the Functional Architecture of the Visual Cortex”. In: *PLOS Computational Biology* 12, e1004758.
- (2015b). “Random Wiring, Ganglion Cell Mosaics, and the Functional Architecture of the Visual Cortex”. In: *PLOS Computational Biology* 12(2), e1004758.
- M. Sur and C. A. Leamey (2001). “Development and plasticity of cortical areas and networks”. In: *Nature Review Neuroscience* 2, pp. 251–262.
- M. V. Albert, A. Schnabel, and D. J. Field (2008). “Innate Visual Learning through Spontaneous Activity Patterns”. In: *plos computational biology* 4, e1000137.
- M. Weliky and L. C. Katz (1994). “functional mapping of horizontal connections in developing ferret visual cortex: experiments and modeling”. In: *J. Neurosci.* 14, pp. 7291–7305.
- N. D. Mermin (1979). “The topological theory of defects in ordered media”. In: *Rev. Mod. Phys.* 51, p. 591.
- N. V. Swindale (1982). “A model for the formation of orientation columns”. In: *Proc. R. Soc. Lond. B* 215, pp. 211–230.
- (1996). “The development of topography in the visual cortex: a review of models”. In: *Network* 7, pp. 161–247.
- P. J. Thomas and J. D. Cowan (2021). “Symmetry Induced Coupling of Cortical Feature Maps”. In: *Phys. Rev. Lett.* 92, p. 188101.
- R. Backmann and K. Albus (1982). “the geniculocortical system in the early postnatal kitten: an electrophysiological investigation”. In: *Exp Brain Res* 47, pp. 49–56.
- R. Durbin and D. J. Willshaw (1987). “An analogue approach to the travelling salesman problem using an elastic net method”. In: *Nature* 326, pp. 689–691.
- R. Durbin and G. Mitchison (1990). “A dimension reduction framework for understanding cortical maps”. In: *Nature* 343, pp. 644–647.
- R. Linsker (1986a). “From basic network principles to neural architecture: emergence of orientation columns”. In: *Proc. Natl. Acad. Sci. USA* 83, pp. 8779–8783.
- (1986b). “From basic network principles to neural architecture: Emergence of orientation-selective cells”. In: *Proc. Natl. Acad. Sci. USA* 83, pp. 8390–8394.
- (1986c). “From basic network principles to neural architecture: Emergence of orientation-selective cells”. In: *Proc. Natl. Acad. Sci. USA* 83, pp. 7508–7512.
- R. Malach et al. (1993). “Relationship between intrinsic connections and functional architecture revealed by optical imaging and in vivo targeted biocytin injections in primate striate cortex”. In: *Proc. Natl. Acad. Sci. USA*. 90, pp. 2432–2442.
- R. Miikkulainen et al. (2005). “Computational maps in the visual cortex”. In: *New York: Springer*.
- S. Behpour, D. J. Field, and M. V. Albert (2021). “On the Role of LGN/V1 Spontaneous Activity as an Innate Learning Pattern for Visual Development”. In: *Front Physiol.* 12, p. 695431.
- S. F. Tavazoie and R. C. Reid (2000). “Diverse receptive fields in the lateral geniculate nucleus during thalamocortical development”. In: *Nat Neurosci.* 3, pp. 608–616.

- S.F.Tavazoie and R.C. Reid (2000). "Diverse receptive fields in the lateral geniculate nucleus during thalamocortical development". In: *Nat Neurosci* 3, pp. 608–616.
- S.Löwel and W.Singer (1992). "Selection of intrinsic horizontal connections in the visual cortex by correlated neuronal activity". In: *Science* 255, pp. 209–212.
- S.Wimbauer, W.Gerstner, and J.L.Hemmen (1998). "Analysis of a correlation-based model for the development of orientation-selective receptive fields in the visual cortex". In: *Network* 9, pp. 449–466.
- T.Bonhoeffer and A.Grinvald (1991). "Iso-orientation domains in cat visual cortex are arranged in pinwheel-like patterns". In: *Nature* 353, pp. 429–431.
- (1993). "The layout of iso-orientation domains in area 18 of cat visual cortex: optical imaging reveals a pinwheel-like organization". In: *J.Neurosci.* 13, pp. 4157–4180.
- T.Bonhoeffer, C.Clopath adn, M.Huebener, and T.Rose (2017). "Variance and invariance of neuronal long-term representations". In: *Phil.Trans.R.Soc.B* 372, p.20160161.
- T.Hainmueller and M. Bartos (2018). "Parallel emergence of stable and dynamic memory engrams in the hippocampus". In: *Nature* 558, pp. 292–296.
- T.Kohonen (1982). "Self-organized formation of topologically correct feature maps". In: *Biol.Cybern.* 43, pp. 59–69.
- (2000). "Self-Organizing Maps". In: (Berlin:Springer)Third Edition.
- (2006). "Self-organizing neural projections". In: *Neural Netw.* 19, pp. 723–733.
- U.R.Karmarkar and D.Yang (2006a). "Experience-Dependent Plasticity in Adult Visual Cortex". In: *Neuron* 52, pp. 577–585.
- (2006b). "Experience-Dependent Plasticity in Adult Visual Cortex". In: *Neuron* 52, pp. 577–585.
- V.Pawlak et al. (2013). "Changing the responses of cortical neurons from sub- to suprathreshold using single spikes in vivo". In: *eLife* 2, e00491.
- W.H.Bosking, J.C.Crowley, and D.Fitzpatrick (2002). "Spatial coding of position and orientation in primary visual cortex". In: *Nature Neuroscience* 5, pp. 874–882.
- W.H.Bosking et al. (1997). "Orientation selectivity and the arrangement of horizontal connections in tree shrew striate cortex". In: *J.Neurosci.* 17, pp. 2112–2127.
- W.Keil and F.Wolf (2011). "Coverage, continuity, and visual cortical architecture". In: *Neural Syst Circ* 1,17.
- W.Keil et al. (2012). "Response to Comment on "Universality in the Evolution of Orientation Columns in the Visual Cortex". In: *Science* 336, p. 413.
- Y.Frégnac, D.Shulz adn S.Thorpe, and E.Bienenstock (1992). "Cellular analogs of visual cortical epigenesis. I. Plasticity of orientation selectivity". In: *J Neurosci.* 12, pp. 1280–1300.
- Y.Frégnac et al. (1988). "A cellular analogue of visual cortical plasticity". In: *Nature* 333, pp. 367–370.
- Z.F.Kisvarday et al. (1997). "Orientation-specific relationship between populations of excitatory and inhibitory lateral connections in the visual cortex of the cat". In: *Cerebral Cortex* 7, pp. 605–618.

Acknowledgements

First of all, I would like to give my thanks to my advisor, Prof. Fred Wolf, who provides the opportunity for me to work in his group and institute and guide me patiently in the "computational neuroscience world". Then, with our cooperation I find ways into research and science.

Secondly, I thank Prof. Theo Geisel for creating excellent atmosphere of this non-linear dynamics department. With interactions between fields may give people new ideas.

Thirdly, I would like to thank my second thesis advisor, Prof. Joerg Enderlein. He reminds that I may need to pay more attention to research details.

Then I would like to thank Dr. Rainer Engelken. He is the one of first persons suggesting me I could spend some time directly visiting the institute.

The next person I would like to thank is Dr. Lars Reichl. He suggests me I could listen to more topics of lectures given in the MPI campus.

Then I would like to thank Dr. Manuel Schodorff and Dr. Juan Daniel Florez Weidinger. They are very nice and their research works are very good.

Then I would like to thank the secretary of CIDBN, Von Behren Christina, she is a very kind person.

Then, I would like to thank all the people in Göttingen campus institute for dynamics of biological networks and Max Planck Campus in Göttingen.

Finally, I would like to thank my country and my family for supporting me these years.

Curriculum Vitae

Personal Information:

Name: Wenqi Wu

Date of Birth: May 18, 1986

Nationality: P. R. China

Email: wuwenqi.2011@gmail.com

Latest degree: Master in mathematics

Education:

Jan 2016 to present	PhD studies in neurophysics in Max Planck Institute for Dynamics and Self-organization
Oct 2014 to Dec 2015	Internship at Max Planck institute for Dynamics and Self-organization
Oct 2011 to June 2014	Master studies in biomathematics of applied mathematics in Northwest Agriculture & Forestry University, China
Oct 2006 to June 2010	Bachelor studies in information and computing science in Faculty of Mathematics in Southwest Jiaotong University, China

Awards:

CSC scholarship from Scholarship Council of China

DAAD scholarship